Microfluidic Thermoelectric Heat Exchangers for Low-Temperature Waste Heat Recovery

A dissertation submitted to

ETH ZURICH

for the degree of

Doctor of Sciences

presented by

Nina Zuzanna Wojtas

MSc ETH Micro and Nanosystems

born October 03, 1982

citizen of Illnau-Effretikon ZH

accepted on the recommendation of

Prof. Dr. Christofer Hierold, examiner

Prof. Dr. Dimos Poulikakos, co-examiner

2014

"Always do whatever's next."

- George Carlin

To my family –

Abstract

More than half of the energy created by humanity is lost as waste heat into the environment. Over 75 % of this dissipated energy is classified as low grade waste heat and its temperature lies below 100 °C. By recovering part of this waste energy, the primary energy usage could be significantly reduced and thus the ecological footprint decreased. However, most technologies fail to produce electrical power at these low temperature levels. A possible solution is offered by thermoelectricity, where power can be generated starting from thermal gradients at arbitrary low temperatures.

There is a significant push to increase the output performance of thermoelectric generators (TEGs) in order to make them more competitive energy harvesters. The thermal coupling of TEGs has a major impact on the effective temperature gradient across the generator and therefore the power output achieved. This work reports on a novel approach combining efficient microfluidic thermal coupling and thin film generators in order to contribute to a significant thermoelectric output performance enhancement.

The proposed thermoelectric heat exchanger (TEHEX) for low temperature waste heat recovery consist of µTEGs in between multi-layer micro heat transfer systems (µHTSs) featuring very low heat transfer resistances and small pumping powers. The implementation of efficient thermal coupling allows for the application of thin film generators for a thermally matched system and thus maximal power output. Additionally, very compact systems and therefore high power densities can be achieved.

The TEHEXs are fabricated in two different size scales and characterized with respect to their net output performance. By means of a small size 8×8 mm device featuring high aspect ratio copper microchannels, the influence of the most relevant system parameters, i.e. the microchannel width, applied fluid flow rates and the µTEG thickness on the system net output performance is investigated. It is shown that dimensions of the µTEG and µHTS can be optimized for specific temperature ranges applied, and the maximum net power can be tracked by adjusting the heat transfer resistance during operation. With the compact system, a total of $63\,\text{mW/cm}^2$ at a fluid inlet temperature difference of $60\,\text{K}$ is measured. This corresponds to a net volumetric efficiency factor (VEF) of $37\,\text{W/m}^3\text{K}^2$, which is by a factor of 4.8 higher than reported elsewhere. The fabricated 9×9 cm large

TEHEX demonstrates the feasibility of a scalable low-cost technology and represents a successful proof of concept for a commercial application in waste heat recovery. The system characterization yields a net power of 0.44 W for one TEHEX unit at an applied fluid thermal gradient of 50 K, corresponding to a net VEF of 5.1 W/m^{3}K^2 per active TEG area, also being the highest among reported net values.

With the characterized systems, the established 1D TEHEX model could be verified and used as a powerful tool for further system analysis and optimizations. By optimizing the geometric parameters of the system as well as the operating conditions, an output power enhancement of up to 65 % could be achieved at an applied thermal gradient of 50 K.

Zusammenfassung

Mehr als die Hälfte der von Menschen erzeugten Energie geht in Form von Abwärme verloren. Über 75 % dieser ungenutzten Energie wird als niedriggradige Abwärme klassifiziert, da ihre Temperatur unterhalb von 100 °C liegt. Durch eine teilweise Rückgewinnung dieser verlorenen Energie könnte der Primärenergieverbrauch sowie der ökologische Fussabdruck signifikant reduziert werden. Im Niedertemperaturbereich versagen jedoch konventionelle Technologien der Energiegewinnung. Eine mögliche Lösung bietet die Thermoelektrizität, dank der bereits bei beliebig kleinen Temperaturgradienten Energie erzeugt werden kann.

Es besteht ein grosses Interesse die Leistung von thermoelektrischen Generatoren (TEG) zu steigern, um sie zu kompetitiveren Energiewandlern zu machen. Die thermische Ankopplung der TEG hat einen wesentlichen Einfluss auf den effektiven Temperaturgradienten über dem Generator und dementsprechend auf dessen Ausgangsleistung. Im Rahmen dieser Arbeit wird ein neuartiges Konzept entwickelt, welches eine effiziente thermische Ankopplung mittels Mikrofluidik mit Dünnschichtgeneratoren verbindet. Dieser Ansatz führt zu einer erheblichen thermoelektrischen Leistungssteigerung des Systems.
Der vorgeschlagene Aufbau eines thermoelektrischen Wärmetauschers (TEHEX) für Abwärmerückgewinnung bei niedrigen Temperaturgradienten, besteht aus alternierend gestapelten μTEG und mehrschichtigen Mikrowärmeübertragungssystemen (μHTS). Die entwickelten μHTS weisen sehr tiefe Wärmeübergangswiderstände sowie eine kleine Pumpleistungen auf. Diese Implementierung der effizienten thermischen Ankopplung erlaubt die Verwendung von Dünnschichtgeneratoren für thermisch abgeglichene Systeme, was zu einer Leistungsmaximierung führt. Zusätzlich können sehr kompakte Systeme mit hoher Leistungsdichte erreicht werden.

Die TEHEX werden in zwei verschiedenen Grössenordnungen hergestellt und bezüglich ihrer Nettoausgangsleistung charakterisiert. Mit dem kleinen 8 x 8 mm System, welches Mikrokupferkanäle mit hohem Aspektverhältnis aufweist, werden die Einflüsse der wichtigsten Systemparameter (i.e. Breite der Mikrokanäle, applizierte Durchflussrate sowie Dicke der Generatoren) auf den Nettoleistungsertrag untersucht. Es wird gezeigt, dass die Dimensionen der μTEG und μHTS für spezifische Temperaturbereiche optimiert werden können und dass die maximale Nettoleistung während dem Betrieb mittels Anpassung der Wärmeüber-

gangswiderstände verfolgt werden kann. Mit dem kompakten System konnte eine Nettoleistung von $63\,mW/cm^2$ bei einem angelegten Fluidtemperaturgradienten von $60\,K$ gemessen werden. Dies entspricht einem netto Volumeneffizienzfaktor (VEF) von $37\,W/m^3K^2$ und ist damit 4.8 Mal höher als anderweitig berichtet. Der fabrizierte $9\,x\,9\,cm$ grosse TEHEX demonstriert die Realisierbarkeit einer skalierbaren und kostengünstigen Technologie und liefert den Machbarkeitsnachweis für eine kommerzielle Anwendung im Bereich der Abwärmerückgewinnung. Die Charakterisierung des Systems ergibt bei einem angelegten Temperaurgradienten von $50\,K$ eine Nettoleistung von $0.44\,W$ für eine TEHEX-Einheit. Dies entspricht einem netto VEF von $5.1\,W/m^3K^2$ pro aktive TEG Fläche, was ebenfalls einer der höchsten publizierten Nettowerte darstellt.

Anhand der charakterisierten Systeme konnte das aufgestellte eindimensionale Model des TEHEX validiert und als wichtiges Werkzeug für eine weiterführende Systemanalyse und Optimierung verwendet werden. Durch Optimierung der geometrischen Systemparameter und der Betriebsbedingungen konnte eine theoretische Leistungssteigerung von bis zu 65 % bei einem angelegten Temperaturgradienten von $50\,K$ aufgezeigt werden.

x

Contents

List of Symbols

Symbol	Units	Description
α	V/K	Relative Seebeck coefficient of thermocouple
α_m	V/K	Absolute Seebeck coefficient of a material
A	m^2	Surface area
AV	–	Active to inactive TEG area ratio
c_p	J/kgK	Specific heat capacity
C_c	–	Constriction loss coefficients
C_e	–	Expansion loss coefficients
d_{ch}	m	Characteristic channel length
d_{hyd}	m	Hydraulic diameter
d_{TEG}	m	Thermocouple diameter
η	–	Efficiency
η_C	–	Carnot efficiency
η_{2nd}	–	Second order efficiency
f	–	Fanning friction factor
ϕ	V	Electrical potential
h_{conv}	W/m^{2}K	Convective heat transfer coefficient
I	A	Electrical current
κ_T	V/K	Thomson coefficient
K_{con}	cm^{2}K/W	Total contact thermal resistance
K_{HTS}	cm^{2}K/W	Thermal resistance of the heat transfer system
K_{TEG}	cm^{2}K/W	Thermal resistance of the generator
λ	W/mK	Thermal conductivity of TE material
l	m	Length
l_h	m	Hydrodynamic entrance length
l_{TEG}	m	Thermocouple length
μ	Pa s	Dynamic viscosity
m	–	Number of thermocouples
Nu	–	Nusselt number
Π	V	Peltier coefficient
Δp	Pa	Pressure drop
P_{out}	W	Output power
P_{out_net}	W	Net output power
PF	W/mK^2	Power factor

Contents

PF_m	W/K^2	Module power factor
$\dot{Q}$	W	Thermal flux
ρ_{el}	Ω m	Electrical resistivity
ρ_c	Ω m^2	Specific contact resistivity
ρ_f	kg/m^3	Density of the fluid
R_{el}	Ω	Electrical resistance of the generator
R_{eff}	Ω	Effective el. resistance of the generator
R_l	Ω	Electrical load resistance
Re	$-$	Reynolds number
s	m	Distance between Thermocouples
σ	S/m	Electrical conductivity
τ_{xy}	$-$	Normalized shear stress
t	m	Thickness
T	K	Temperature
$\overline{T}$	K	Average temperature
ΔT	K	Temperature difference
ΔT_{TEG}	K	Temperature difference across the generator
ΔT_0	K	External temperature difference
$\vec{\nabla} T$	K	Temperature gradient
u	m/s	Fluid velocity
V	m^3	System volume
V_{oc}	V	Open circuit voltage
V_S	V	Seebeck voltage
$\dot{V}$	m^3/s	Volumetric flow rate
Z	K^{-1}	Material figure of merit
ZT	$-$	Dimensionless figure of merit
Z_m	K^{-1}	Module figure of merit
ZT_m	$-$	Dimensionless module figure of merit

Abbreviations

Abbreviation	Description
1D	One-dimensional
BCB	Benzocyclobutene
CWC	Cylinder water cooler
DFR	Dry film resist
DI	Distilled water
DOS	Density of states
ECD	Electrochemical deposition
FEM	Finite element method
GBL	γ-butyrolactone
GUI	Graphical user interface
HCL	Hydrochloric acid
HES	Heat exchange system
HNO$_3$	Nitric acid
HTS	Heat transfer system
IPA	Isopropanol
LOR	Lift-Off resist
MC	Microchannel
MF	Manifold
PF	Power factor
PMMA	Poly(methyl methacrylate)
TC	Thermocouple
TE	Thermoelectric
TEG	Thermoelectric generator
TEHEX	Thermoelectric heat exchanger
US	Ultrasound
UV	Ultraviolet
VEF	Volumetric efficiency factor
WHR	Waste heat recovery
WLI	White light interferometry

1 Introduction

The simultaneous rise in energy consumption and environmental awareness creates a worldwide growing demand for more efficient and clean energy systems. One promising approach to improve a system's efficiency is to reduce the thermal losses by recovering a part of the produced waste heat. At least half of the energy created by humanity is dissipated as waste heat into the environment [1, 2]. Contemporary vehicle engines, for example, lose more than 60 % of their fuel energy in the form of heat [3]. Also most of today's steam generator based electrical power plants run on a very low average net efficiency below 36 %, and are therefore creating enormous amounts of waste heat [2, 4]. Thus, with the perspective of reducing primary energy usage and decreasing environmental impacts, the interest in waste heat recovery has gained more and more attention [2, 5, 6]. A potential correlation between global warming and produced waste heat has even been discussed [7, 8].

Apart from established technologies to convert waste heat into electricity by means of combined turbine cycles or recuperative heating [2], thermoelectricity has been identified as a promising approach to recover energy [9–11]. Thermoelectric generators (TEGs) convert an applied thermal gradient directly into electrical energy by taking advantage of the Seebeck effect. Although thermoelectric power generation cannot compete with the existing thermodynamic cycles with respect to conversion efficiency [12], it offers several other advantages such as device simplicity, compactness, scalability and an arbitrarily low operating temperature range. The last point is of particular importance, since most of the waste heat is available in the range below $100\,°C$ [2], where other technologies fail to produce electrical power. Therefore, the most attractive applications for thermoelectric power generation lie in low temperature waste heat recovery from technical or natural sources [9, 11, 13, 14], transportation [15, 16] as well as energy harvesting for small autonomous systems [17–19].

1.1 Rationale

So far, the commercial applications of TEGs have been limited to niche markets such as aerospace [20, 21] and power supply in remote or hazardous places [22, 23]. The main reasons for this are (1) the relatively low thermoelectric conversion efficiency, (2) high fabrication costs of thermoelectric modules, (3) suboptimal exploitation of the available temperature gradients and (4) neglecting

the importance of a thorough system level optimization. While much effort is spent to improve the thermoelectric figure of merit *ZT* by nanostructuring [24–26] as well as to develop low-cost fabrication technologies [27–29], less attention has been paid to maximizing the thermal gradient exploitation and system level optimization. This in particular relates to the thermal coupling of the thermoelectric device to the heat source and the heat sink, an optimal matching of the thermal contact and TEG resistances [30], as well as the consideration of the net system performance.

By decreasing the thermal contact resistance to the cold and hot reservoir, a significant enhancement of the generator's output power can be achieved. The impact of the thermal contact resistance on the output performance of a thermoelectric generator is illustrated in Figure 1.1 and compared to the effect of the figure of merit *ZT*. While the output power exhibits a close to linear dependency on *ZT*, it is inversely proportional to the thermal contact resistance squared.
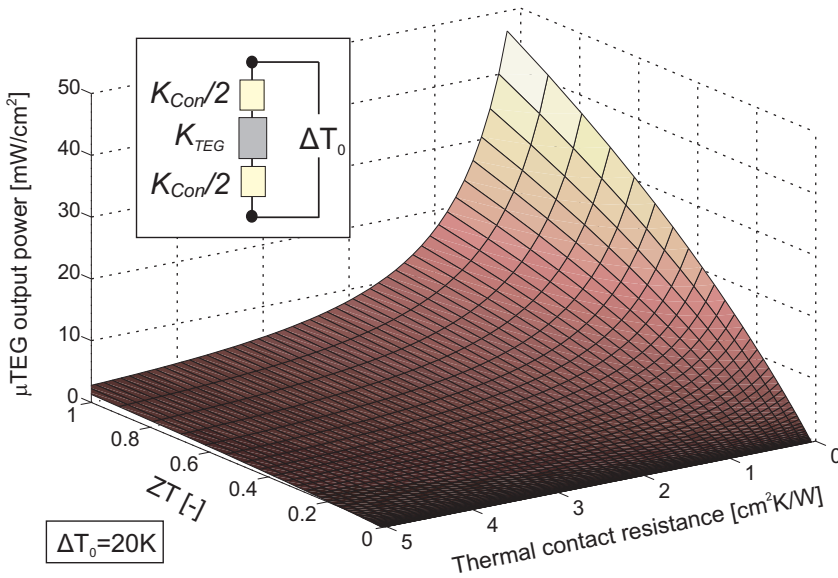
Figure 1.1: Simulated output power of a 215 μm thick Bi_2Te_3 μTEG ($K_{con} = 2.65\,cm^2K/W$) with respect to the *ZT*-value and the thermal contact resistance K_{con} at an applied temperature difference of 20 K.

In the so far presented approaches of thermoelectric heat exchangers (TEHEX) for waste heat recovery applications, only large conventional heat exchangers have been applied (see Chap. 2 for details). These systems feature large heat transfer resistances and are operated at high fluid flow rates [31]. Thus, large

pumping powers are needed, which are mostly neglected in the overall systems characterization.

By applying microfluidic heat transfer systems (μHTSs), the thermal contact resistance can be significantly reduced. μHTSs can achieve very high heat fluxes at small fluid flow rates as a result of an increased convective heat transfer coefficient and heat transfer surface area [32]. Additionally, more compact systems with reduced size and weight can be built, leading to improved applicability and modularity of the system. Many efficient μHTSs have been developed mainly for cooling applications of integrated circuits and optoelectronic devices. The system designs and methods include simple microchannels [32–34], multilayer manifold structures [35–38], porous media [34, 39], pin fin structures [40–42] and jet impingement [34, 43]. While most devices exhibit a similar heat dissipation capacity, manifold structures in particular show a superior hydrodynamic performance [34].

Apart from an enhanced thermal gradient, a reduction of thermal contact resistances to the heat source and sink bears an additional important advantage: by applying thermal resistance matching for maximal power output, the thickness of the generators can be decreased to the micrometer range, leading to a significant reduction in size, weight, and cost.

Therefore, a systematic analysis and optimization of a TEHEX system including the development of a μHTS enabling reduced thermal resistance with low pumping powers is necessary to overcome the present limitations. The following subsection introduces the proposed concept in more detail.

1.2 Concept of compact TEHEX enabled by microfluidic coupling

The presented approach combines thin film Bi_2Te_3 generators with efficient microfluidic heat transfer systems. In Figure 1.2, the schematic view of the proposed thermoelectric heat exchanger is depicted. Each μHTS consists of three functional layers: two copper layers featuring high aspect ratio microchannels for efficient heat dissipation or supply, and a polymer manifold layer for the fluid distribution. The manifold channels are tapered in order to generate a constant pressure drop across the microchannels, ensuring a homogeneous fluid distribution and thus uniform heat transfer over the entire device [44]. By choosing a thermally isolating polymer as the manifold material, the thermal crosstalk between the manifold and the copper channels is limited, and therefore the fluid temperature change along the inlet channels reduced. This configuration combines the advantages of very low heat transfer resistances enabled by the microchannels, and small pressure losses due to the short fluid paths inside the microchannels.
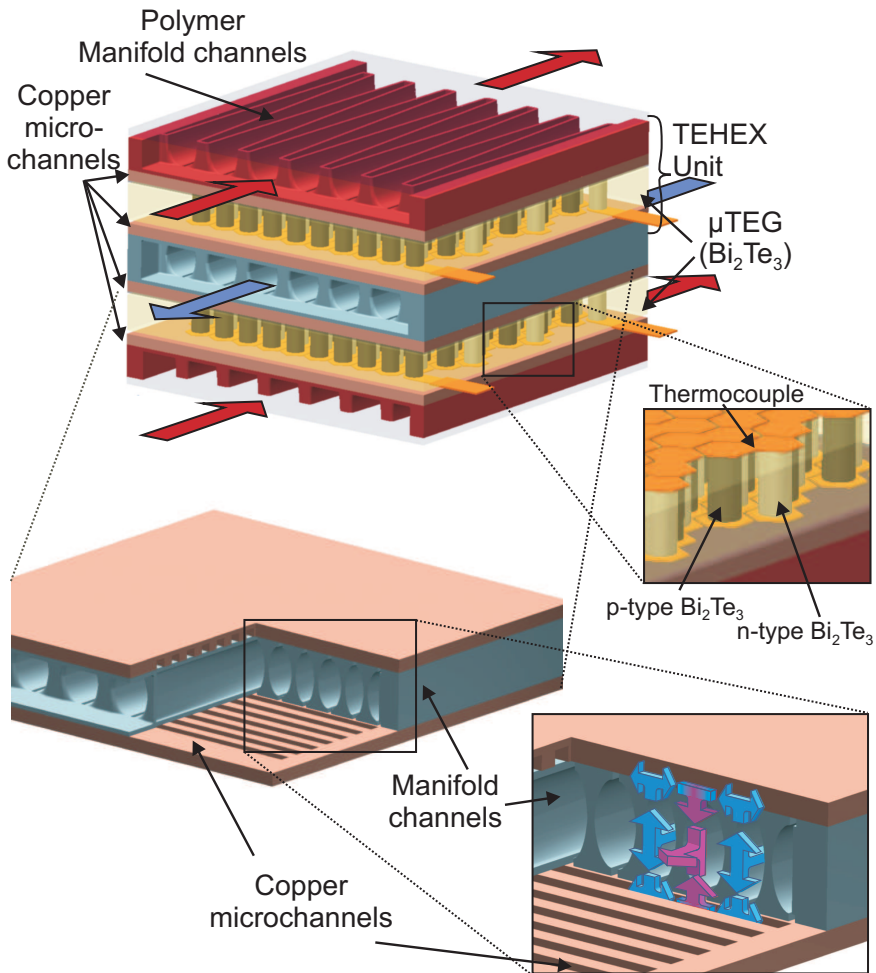
Figure 1.2: Schematic drawing of the proposed thermoelectric heat exchanger with enlarged view of the multilayer heat transfer system.

The reduced hydrodynamic resistance offers a significant advantage over conventional one layer heat transfer systems, since the necessary pumping power needs to be subtracted from the TEHEX output power for an overall system performance evaluation.

The thin film TEGs are fabricated by means of a low-cost process based on electrochemical deposition into a polymer mould [27, 28]. The fabrication method allows for a variable generator design with respect to TEG thickness and pile size, making system level optimization feasible.

1.3 Objective and outline of this work

Based on the proposed compact stacked thermoelectric heat exchanger system, the following objectives are pursued within the framework of this thesis:

1. Investigation of the impact of microscopic features on the system level performance of macroscopic thermoelectric heat exchangers. The objective is to show how the combination of optimized microfluidic concepts and matched thin film generators will enhance the net performance of TEHEXs.

2. Development of suitable fabrication processes for the implementation of highly efficient micro heat transfer systems on two different size scales: one small size approach to investigate the different parameter dependencies and achievable net system performance, and a large size approach to show the feasibility of a scalable low-cost technology as well as to demonstrate the potential for low temperature waste heat recovery. The focus is set on the technology developed for high aspect ratio microchannels and on the implementation of optimal material combinations.

3. A systematic analysis, characterization and modelling of the TEHEX in order to investigate the most important system parameters and to allow for a profound system understanding and model validation.

4. Application of the verified model for a detailed optimization study, as well as the demonstration of the systems potential and technological limitations with respect to specific applications in low temperature waste heat recovery.

The thesis is structured as fallows:

In Chapter 2, the state of the art of existing liquid-liquid and gas-liquid thermoelectric heat exchangers is discussed and compared by means of an introduced system comparison factor, the volumetric efficiency factor (VEF). Further, first systems of thermoelectric generators combined with microfluidic approaches are reviewed.

In Chapter 3, the theory and model of the two main components of the thermoelectric heat exchanger, the TEG and the µHTS, are introduced and discussed separately. Important design aspects and parameter interdependencies are highlighted and fist system improvements are proposed. The final combined TEHEX model is presented and the computation routine is outlined.

In Chapter 4, the developed fabrication process of the small and large size μHTS is documented and the advantages and limitations of the applied technologies are discussed. Furthermore, the assemblies of the two TEHEXs, the corresponding measurement setups and measurement conditions are explained.

In Chapter 5, the fabricated small and large size TEHEXs are characterized and the impact of different design parameters and boundary conditions on the net performance is investigated. The characterization results are compared to the 1D model developed in parallel, and related to the current state of the art.

In Chapter 6, the verified model is used for a systematic analysis of the most important TEHEX design parameters and for a system level optimization. Additionally, the performance and profitability of the optimized system design is estimated for the specific application in a marine propulsion engine.

In Chapter 7, the most important results are summarized and corresponding conclusions are drawn. Further, a brief outlook is given in perspective of potential applications.

2 State of the Art

In the first part of this chapter, a review of existing concepts of large size thermo-electric heat exchangers for industrial and automotive applications is presented and discussed. The second part of the review focuses on TEGs combined with microfluidic heat transfer systems.

2.1 Large size thermoelectric heat exchangers

Several large size fluidic systems have been modelled, developed and tested for the use in industrial and automotive waste heat recovery (WHR). Waste heat produced by machines, engines, electrical equipment or industrial processes that cannot be recycled effectively by conventional methods, is usually dissipated into the environment. Additional to this human created waste heat, naturally occurring heat from solar irradiation, geothermics and ocean thermics can also be a potential source for thermoelectric energy production. The heat from industrial processes and natural sources with a temperature below $100\,°C$ is considered as low temperature waste heat and is usually carried in form of liquids. The specific application scenarios for low temperature WHR in marine engines will be discussed in more detailed in Chapter 6. In applications related to combustion engines for transportation or power generation, where the heat is mostly available as exhaust gas, much higher temperatures are present.

In order to compare the performance of different thermoelectric heat exchange systems with different dimensions and applied temperature gradients, a volumetric efficiency factor VEF is introduced

$$VEF = \frac{P_{out}}{V\,\Delta T^2} \tag{2.1}$$

where P_{out} is the generated output power, V is the system volume and ΔT is the applied inlet temperature gradient of the hot and cold working fluids. For the volume calculations, only the effective TEHEX dimensions were considered, excluding the connecting fluid pipes and manifolds. The net volumetric efficiency factor can be computed by inserting the net output power P_{out_net} of the system into Eq. 2.1. The volumetric efficiency factor combines the performance of the generator (thermoelectric efficiency and power density) with the performance of

the heat exchanger (heat transfer resistance and compactness).

The reported waste heat recovery systems are summarized in Table 2.1 and in Figure 2.1 the corresponding VEFs are plotted against the applied fluid inlet temperature difference.
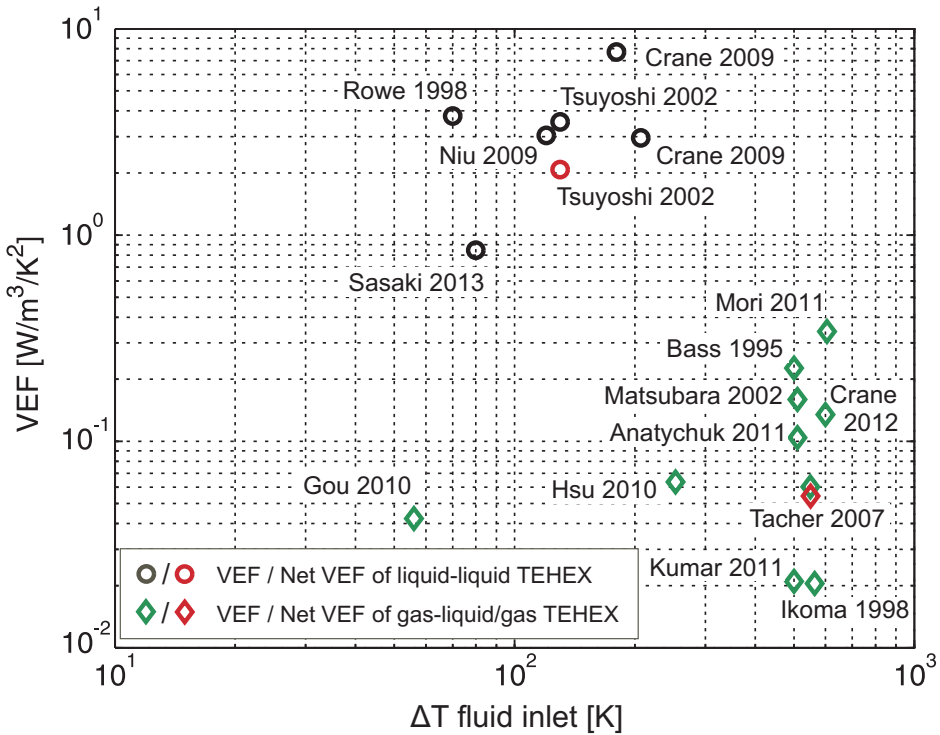
Figure 2.1: Volumetric efficiency factors VEFs for published liquid-liquid and gas/liquid-gas TEHEXs as a function of the applied fluid inlet temperature difference. More detailed information about the corresponding publications can be found in Tab. 2.1.

Liquid-liquid TEHEX

First development of thermoelectric heat exchangers for industrial large scale waste heat recovery started in 1994 within the framework of the NEDO project (Japanese New Energy and Industrial Technology Development Organisation) [45]. The project was based on a previously conducted feasibility study [46]. Due to a large dependency on fossil fuel and nuclear power, vast occurrence of natural

Table 2.1: Comparison of state of the art TEHEXs for industrial and automotive applications.

Liquid-liquid systems											
Author	Group	Year	Working Media	TE mat (ZT)	ΔT	P	Net P	Volume	VEF	Net VEF	Ref
					[K]	[W]	[W]	$[10^{-3}\,\mathrm{m}^3]$	$[\frac{W}{m^3K^2}]$	$[\frac{W}{m^3K^2}]$	
Rowe	UW Cardiff	1998	water/water	-	70	100	-	5.4	3.8	-	[45]
Tsuyoshi et. al	KCCT	2002	oil/water	Bi_2Te_3	130	170	100	2.84	3.54	2.08	[47]
Niu et al.	XJTU	2009	glycol-water/g-w	Bi_2Te_3 ($\sim$0.75)	120	146.5	-	3.34	3.04	-	[48]
Crane et al.	BSST LLC	2009	oil/water-ethyl.	Bi_2Te_3	207	500	-	4.1[1]	2.96[1]	-	[49]
Crane et al.	BSST LLC	2009	oil/water-ethyl.	Bi_2Te_3	180	105	-	0.42	7.7	-	[49]
Sasaki et al.	Toshiba	2013	water/water	-	80	900	900[2]	167	0.84[2]	-	[50]
Gas-liquid/gas systems											
Birkholz et. al	Porsche	1988	exhaust/coolant	$FeSi_2$	-	58	-	-	-	-	[51]
Bass et. al	Hi-Z Tech.	1995	exhaust/coolant	Bi_2Te_3	500[3]	1068	-	19[1]	0.23[1,3]	-	[15, 52, 53]
Ikoma et. al	Nissan	1998	exhaust/coolant	Si_2Ge	563	36	-	5.5	0.02	-	[54]
Matsubara	SUT	2002	exhaust/coolant	seg. (0.7-1)	510	266	-	6.4[1]	0.16[1]	-	[55]
Crane et. al	UMD	2004	coolant/air	Bi_2Te_3	64	0.54	-	-	-	-	[56]
Thacher et al.	CU,GM	2007	exhaust/coolant	Bi_2Te_3	550	250	230	13.7[1]	0.06[1]	0.055[1]	[57]
Gou et al.	CQU	2010	water/air	-	56	0.85	-	0.64[1]	0.042[1]	-	[58]
Hsu et al.	NTHU	2010	exhaust/air	Bi_2Te_3 (0.9/1)	253	43.3	-	10.8	0.064	-	[59]
Kumar et al.	VIT Uni.	2011	exhaust/coolant	Bi_2Te_3	500[3]	71	-	13.5[1]	0.021[1,3]	-	[60]
Anatychuk et al.	INTS UA	2011	exhaust/water	-	440	2100	-	-	-	-	[61]
Anatychuk et al.	INTS UA	2011	exhaust/water	Bi_2Te_3	510[3]	600	-	22[1]	0.1[1,3]	-	[62, 63]
Mori et al.	Honda	2011	exhaust/coolant	(0.8-1.1)	605	450	-	3.6	0.34	-	[64]
Crane et al.	Gentherm	2013	exhaust/coolant	Bi_2Te_3/h-Heusler	600	704	-	14.5	0.135	-	[65–67]

[1]Estimated volume based on reported dimensions and drawings.
[2]Use of potential energy.
[3]Estimated temperature, since cold side not stated in the publication.

hot springs and strong environmental awareness, Japan has been proactive in the development of new energy sources in perspective of future micro grid power supply systems [68]. In the course of the project, high power density modules with smaller thermocouples and reduced spacing have been produced and integrated into fluidic heat exchangers. The developed WATT (Waste heat Alternative Thermoelectric Technology) modules were capable of delivering up to 100 W power at an applied fluid temperature difference of 80 K, reaching a power density of $18.5 \, \text{kW/m}^3$ [45]. A cost analysis of the system yielded a pay back time of approximately two years.

In 2005, a TEHEX employing 329 Bi_2Te_3 modules was installed at the Kusatsu hot springs, where a constant hot water supply at 369 K is available [14]. By 2009, the plant generated more than 1360 kWh and was used for powering TV displays and lighting units. Tsuyoshi and Matsuura [47] reported modelling and experimental results of a thermoelectric engine composed of TEGs stacked between parallel plate heat exchangers using oil and water as active media. At an applied temperature gradient of 130 K, an output power of 170 W total and 100 W net could be reached. Niu et al. [48] built a similar parallel plate heat exchanger with commercially available Bi_2Te_3 modules, reaching 140 W at an inlet temperature difference of 120 K. Crane et al. [49] constructed a TEG-heat exchange assembly with a stack of 6 TEG modules producing 500 W at an inlet temperature difference of 205 K. A second generation high-power-density system reached a VEF of 7.7, mainly due to the increase of the thermopile density. Toshiba [50] built and installed a thermoelectric plant that runs by the thermal energy of natural hot spring water, reaching 900 W peak power ($\Delta T = 80$ K). The gained energy was used to power LED lights in a hotel lobby. Commissioned in 2011, it has generated a total energy of 1927 kWh after a operating time of 1.5 years. The water system was run by a potential energy difference, thus no pumping power was required.

Although the achieved output power values from the reported experimental studies are remarkable, the systems are very large and heavy, resulting in a maximal VEF of 7.7 (see Fig. 2.1). In most cases, thick commercially available TEGs and standard large size heat exchangers are applied, where high amounts of the working fluid are pumped through the system and the consumed pumping power is neglected. Furthermore, the reported systems work without an optimized thermal contact resistance as well as overall system design.

Gas-liquid/gas TEHEX

Due to low conversion efficiencies of internal combustion engines (30 - 43 % [69]) as well as the high energy consumption in the transportation sector, automotive

engines are predestined for thermal waste heat recovery. With the exhaust temperatures ranging from 500-1200 K and the cooling cycle temperature below 350 K, high thermal gradients and moving fluids are available.

As early as 1914, the possibility of scavenging energy from the car exhaust has been investigated [70] and a first prototype was built in 1964 [71]. In 1988, a thermoelectric generator using 90 $FeSi_2$ thermoelements was installed in a Porsche 944 engine and delivered up to 58 W at full power [51]. Starting form 1991, Hi-Z Technology Inc. started developing a thermoelectric recovery system for heavy duty trucks, reaching over 1 kW power on a test engine [15, 52, 53]. In the last decade, the interest in thermoelectric waste heat recovery in passenger cars has exploded and an international workshop was dedicated exclusively to this topic [72]. All the main car companies inducing General Motors [57, 73], BMW [65–67, 74] or Toyota [55] are involved in thermoelectric projects. The best performing TEHEX for passenger vehicles has been developed within the framework of a seven-year program started in 2004, in a collaboration between Amerigon (now Gentherm), BMW and Ford. The result was a system integrated into a BMW X6 and a Lincoln MKT reaching over 700 W on the test bench and over 600 W in on-vehicle tests (BMW). A net fuel efficiency increase of 1.2 % was reported [65–67]. Not only vehicle exhaust gas, but also car radiators [56] or stationary diesel power plants [61] have been identified as potential fields for thermoelectric heat exchange applications. In the latter example, up to 2.1 kW could be recovered, corresponding to 4.4 % of the total electric power produced by the diesel plant.

Despite the large development efforts towards automotive waste heat recovery, several challenges need to be solved in order to enable a commercial breakthrough of the technology. Next to reliability and long-term durability issues triggered by frequent thermal cycling, as well as the induced weight penalty, the cost efficiency has been identified as the most critical criterion. To meet market requirements and be competitive with other emerging technologies, it is estimated that TE modules must be produced and assembled at a fraction of today's cost [75]. To enhance the output power per cost, new fabrication technologies, higher ZT materials and optimization at the system level will be necessary.

Analogous to the liquid-liquid TEHEXs, the existing solutions work with thick and heavy commercial modules and do not take thermal optimization aspects into consideration. The calculated and estimated VEFs of the reported gas-liquid systems are significantly lower compared to the liquid solutions. This is mainly due to a lower thermal conductivity and heat capacity of the gases, i.e. lower heat transfer coefficients, as well as important dimensional constrains related to back pressure issues of the engine exhaust pipe.

2.2 Thermoelectric generators in combination with microfluidics

Although the importance of reduced thermal coupling resistances and system level optimization has been identified and confirmed by simulations [30, 76–78], only few groups have started experimental investigations towards the integration of TEGs with microfluidic heat transfer systems.

Reziana et al. simulated [79, 80] and published first experimental results [81] of TEGs cooled by a parallel microchannel heat sink. The focus of the experimental study was to explore the optimum coolant flow rate for a maximal net power performance of the system. With a setup consisting of a heater, a 56×56 mm TEG (G2-56-0375, Tellurex) and twenty plate-fin aluminium microchannels having a hydraulic diameter of 0.93 mm and an aspect ratio of approximately 1, a maximal net power of 2 W was generated at a temperature difference of 80 K directly across the TEG. The author concluded that the optimal coolant flow rate increases with increasing applied temperature gradient. Due to the simple parallel microchannel structure, large pressure losses and a decrease of the thermal gradient along the channel flow would limit the device performance in a scaled up system.

An interesting theoretical and experimental study of a phase change MEMS-based capillary heat exchanger designed as a heat sink for thermoelectric waste energy harvesting has been published by Mathew et al. [82]. The fabricated prototypes consisted of silicon and SU-8 based heat exchangers with rectangular 100 µm wide and up to 375 µm high microchannels (total footprint of 38×13 mm). A minimal thermal contact resistance of $33 \, \text{m}^2\text{K/W}$ was reached operating at the boiling point of the working fluid.

Concluding from the discussed experimental works, the possible approaches for improving the integration of microfluidic features mainly involve a system design enabling efficient and homogeneous fluid distribution with low pumping power as well as smaller microchannels. Additionally, a sufficient heat capacity and corresponding flow rates of the working fluid must be achieved in order to allow efficient heat transfer.

3 Theory and Modelling

The first part of this chapter will introduce the fundamentals of thermoelectricity and TE modelling, as well as highlight important aspects and conclusions related to the module design and application. In the second part, theory and modelling of microfluidic heat transfer systems will be discussed. The final part will combine both fields and introduce the thermoelectric heat exchanger model.

3.1 Thermoelectric generators

3.1.1 Fundamentals of thermoelectricity

Three thermoelectric effects, the Seebeck [83], the Peltier and the Thomson effect, contribute to the direct conversion of heat into electricity and vice-versa. They are based on the interaction between heat and charge carriers and are thermodynamically reversible.

Seebeck effect

When a temperature gradient is applied to a conductor or semiconductor, an electromotive force is generated, leading to the build up of electrical potential $\vec{\nabla}\phi$

$$\vec{\nabla}\phi = -\alpha_m(T)\vec{\nabla}T \tag{3.1}$$

where $\alpha_m(T)$ is the absolute temperature dependent Seebeck coefficient and $\vec{\nabla}T$ is the temperature gradient. For small temperature differences applied, α_m can be assumed constant and the integration over the material will yield an expression for the generated Seebeck voltage

$$V_S = -\alpha_m\left(T_h - T_c\right) = -\alpha_m\,\Delta T \tag{3.2}$$

where T_h and T_c are the applied temperatures at the hot and cold side of the material, respectively. In practice, the Seebeck voltage can only be exploited by combining two materials with different (preferably opposite signed) Seebeck coefficients

$$V_{S1\_2} = \left(\alpha_{m1} - \alpha_{m2}\right)\left(T_h - T_c\right) = \alpha\,\Delta T \tag{3.3}$$

where α is the relative Seebeck coefficient of a thermocouple (TC). Applying the same material would results in the cancellation of the electric potential.

The Seebeck effect is based on the combination of several physical phenomena which will be briefly discussed [84]. The main contribution to the Seebeck effect in semiconductors is thermodiffusion [85]. The kinetic energy of the charge carriers is temperature dependent. Therefore, the charge carriers on the hot side (electrons for n-type and holes for p-type semiconductors) have a higher kinetic energy and thus higher local thermal velocity than the carriers on the cold side. As a result, more carriers diffuse in average from the hot to the cold side than vice-versa, causing a charge accumulation at the cold end. The carrier concentration of semiconductors also strongly varies with temperature. A thermal gradient results in a carrier concentration gradient and therefore gradient based diffusion towards lower concentrations (cold side). Changes of the band gap with temperature can also lead to a carrier flow between the two ends of the semiconductor. In metals and semiconductors with approximately equal concentration of holes and electrons, the dependence of the diffusion coefficient or the charge carrier mobility on temperature can lead to negative as well as positive Seebeck coefficients. The Fermi level also reduces with increasing temperature, resulting in an carrier movement from the cold to the hot side. Additionally, phonons follow the temperature gradient from the hot to the cold end. Due to phonon-charge carriers interactions, the carriers can be pushed along with the lattice vibrations by the so called phonon drag effect. The combination of all those effect leads to a final charge accumulation at either end of the conductor. The resulting electric field counteracts a further charge build up and an equilibrium is reached.

Several approaches to physically model the Seebeck coefficient with different levels of complexities have been reported in literature [84, 86–88].

Peltier effect

When an electric current is flowing through a junction of two conducting materials, heat is generated or absorbed. This heat current $\dot{Q}_P$ originates from the Peltier effect

$$\dot{Q}_P = (\Pi_{m1} - \Pi_{m2})\, I = \Pi\, I = \alpha\, T\, I \qquad (3.4)$$

where Π_m is the absolute Peltier coefficient of one material, Π is the relative coefficient of the two conductors (i.e. the TC) and I is the electric current. The first Thomson relation links the Peltier with the Seebeck effect. In thermoelectric generators, the Peltier heat is supplied by the hot side heat source and delivers the energy for the electric current to run [89] .

Thomson effect

When an electric current is flowing through a homogeneous conductor with an applied thermal gradient, heat is generated or absorbed (additional to the Joule heat). This Thomson heat originates from the temperature dependent Seebeck coefficient. If a current is driven through a conductor with an applied thermal gradient, a continuous Peltier effect will occur. The Thomson heat can be expressed as

$$\dot{Q}_T = \kappa_T \, I \, \Delta T = \frac{d\alpha}{dT} \, T \, I \, \Delta T \tag{3.5}$$

where κ_T is the Thomson coefficient. The second Thomson relation links the Seebeck with the Thomson effect. Since the Thomson effect is small in comparison to the other two thermoelectric effects, it is often neglected in the device modelling. Especially for small temperature gradients and thin-film TEGs, this is a reasonable model simplification.

3.1.2 Thermoelectric materials and modules

The suitability of a material for thermoelectric conversion can be expressed with the figure of merit [90]

$$Z = \frac{\alpha^2 \, \sigma_{el}}{\lambda} = \frac{\alpha^2}{\lambda \, \rho_{el}} \tag{3.6}$$

where λ is the thermal conductivity, σ_{el} is the electrical conductivity and ρ_{el} is the electrical resistivity of the material. For efficient energy conversion, a low thermal conductivity for high temperature gradients and low electrical resistivity for low ohmic losses are desired. All three parameters of Z depend on the charge carrier concentrations of the material (see Fig. 3.1). Therefore, an optimal carrier concentration for high Z-values can be found between 10^{18} and 10^{20}cm^{-3}, corresponding to highly doped semiconductors and semi-metals.

The more commonly used dimensionless figure of merit $Z\overline{T}$ is obtained by multiplication with the average system temperature $\overline{T}$. Figure 3.2 gives an overview of the state of the art and state of the practice thermoelectric materials and their $Z\overline{T}$ values. Next to the well established compound semiconductors (e.g. PbTe, Bi$_2$Te$_3$) with a maximum $Z\overline{T}$ around unity, new engineered materials have emerged in the recent decade. This boost of $Z\overline{T}$ has been achieved through (1) enhancement of the electron density of states (DOS) near the Fermi level by quantum confinement or band gap engineering [91–96] and (2) an enhancement of phonon scattering by increasing the presence of interfaces [24, 25, 97–102] (e.g. grain boundaries, defects, dislocations, or acoustic mismatch). The latter can significantly reduce the phonon mean free path and thus the thermal conductivity λ of the TE material. Quantum confinement potentially leads to a simultaneous
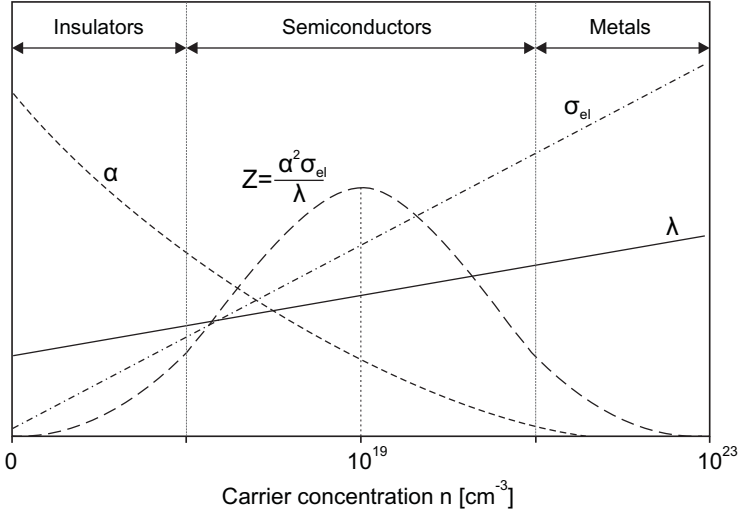
Figure 3.1: Correlation between the thermoelectric figure of merit Z, the Seebeck coefficient α, the thermal conductivity λ and the electrical conductivity σ on the charge carrier concentrations n of a material. Reproduced according to [84].

increase of the Seebeck coefficient α, a reduction of the electrical resistivity ρ_{el} and, as a side effect, also to a decrease of λ by boundary scattering effects. While working with nano confined structures like nanowires has shown to be difficult to scale up and impracticable for large scale power generation [26], the focus has shifted to engineering bulk materials that mimic the local DOS of nano structures (e.g. resonant impurity doping [103]).

Analogous to the material figure of merit, a TEG module figure of merit Z_m (or $Z\overline{T}_m$) can be expressed as

$$Z_m = \frac{(m\alpha)^2 K_{TEG}}{R_{el}} \tag{3.7}$$

where m is the number of in series connected TC of the module, K_{TEG} is the thermal and R_{el} the electrical resistance of the generator. Additional to the material properties in Z, Z_m includes parasitic thermal losses through the isolating material and electric losses through the contact and interconnect resistances. Refer to Eq. B.1 - Eq. B.6 in Appendix B for detailed definitions of K_{TEG} and R_{el}.

The open circuit voltage V_{oc} of a thermoelectric module is defined as

$$V_{oc} = m\alpha\Delta T_{TEG} \tag{3.8}$$
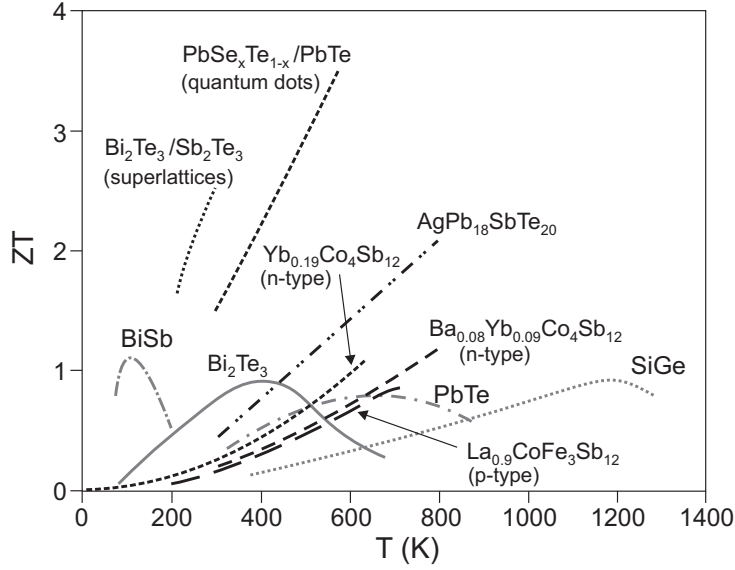
Figure 3.2: *ZT* versus *T* for state of the practice (gray lines) and state of the art materials (black lines). Reproduced according to [16] (2009).

where ΔT_{TEG} is the temperature gradient directly over the generator. Figure 3.3 shows the schematic thermoelectric network of a TEG. The output power of the module P_{out} can be expressed as

$$P_{out} = VI = V_{oc}^2 \frac{R_l}{(R_l + R_{el})^2} = (m\,\alpha\,\Delta T_{TEG})^2 \frac{R_l}{(R_l + R_{el})^2} \tag{3.9}$$

where R_l is the applied load resistance. The thermal efficiency of a module can be calculated by dividing P_{out} by the input power P_{in}, i.e. the incoming heat flux $\dot{Q}_{in}$

$$\eta = \frac{P_{out}}{P_{in}} = \frac{P_{out}}{\dot{Q}_{in}} = \frac{\dot{Q}_{in} - \dot{Q}_{out}}{\dot{Q}_{in}} \tag{3.10}$$

The 2nd order efficiency can be formulated in terms of the Carnot efficiency η_C

$$\eta_{2nd} = \frac{\eta}{\eta_C} = \eta \frac{T_h}{(T_h - T_c)} \tag{3.11}$$

If the thermoelectric cycle would be entirely reversible, η_C could be reached. In practice, the efficiency is strongly limited by irreversible heat losses from Joule heating and thermal conduction.
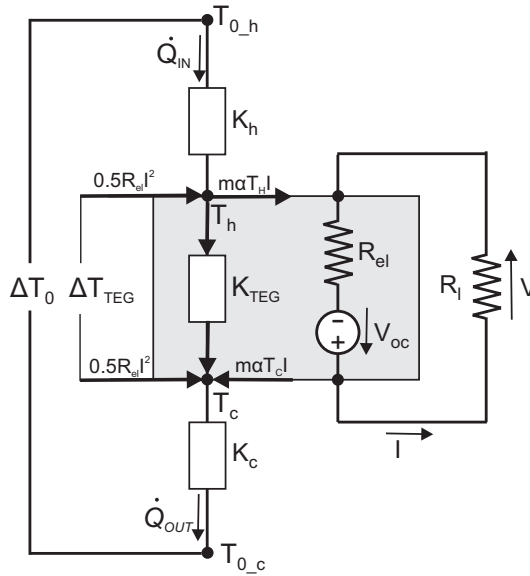
Figure 3.3: Schematics of a thermoelectric network including the thermal and electric components.

3.1.3 Thermoelectric generator modelling

To compute the temperature gradient ΔT_{TEG} across the generator, the basic heat balance equations at the hot and cold junctions of the generator must be solved. Neglecting the Thomson effect and assuming that thermoelectric material properties remain constant over the operating temperature range, the incoming and outgoing heat current $\dot{Q}_{in}$ and $\dot{Q}_{out}$ can be expressed as [90, 104–107]

$$\dot{Q}_{in} = m\,\alpha\,T_h I - \frac{1}{2}R_{el}\,I^2 + \frac{(T_h - T_c)}{K_{TEG}} \tag{3.12}$$

$$\dot{Q}_{out} = m\,\alpha\,T_c I + \frac{1}{2}R_{el}\,I^2 + \frac{(T_h - T_c)}{K_{TEG}} \tag{3.13}$$

including the energy supply and removal by the Peltier effect, Joule heating (equally divided between the hot and cold junctions) and heat conduction losses through the generator. The electric current generated under applied load is given as

$$I = \frac{m\,\alpha\,(T_h - T_c)}{R_l + R_{el}} \tag{3.14}$$

The incoming and outgoing heat flux through the thermal contacts can be expressed by Fourier's law of heat conduction as

$$\dot{Q}_{in} = \frac{1}{K_h} (T_{0-h} - T_h) \tag{3.15}$$

$$\dot{Q}_{out} = \frac{1}{K_c} (T_c - T_{0-c}) \tag{3.16}$$

where K_h and K_c are the cold and hot thermal contact resistances, respectively. Solving Equations 3.12 - 3.16 after $\Delta T_{TEG} = T_h$ - T_c leads to a complex cubic equation which is analytically solvable [27, 89, 106, 108], however impractical to handle. Therefore, the set of transformed equations (see Eq. B.7 and B.8 in App. B) was implemented to be solved numerically using the fsolve function provided by Matlab. This allows, apart from easy handling, for more flexibility in extending the model by adding arbitrary thermal resistances and also for modelling multilayer TEG stacking.

For the comprehension of the following impedance matching section and further illustrations, two approximate analytical solutions for ΔT_{TEG} will be briefly presented. By neglecting second and third order terms from the cubic ΔT_{TEG} solution and assuming small temperature gradients across the generator (T_h and $T_c \approx \overline{T}$), ΔT_{TEG} can be expressed as [89]

$$\Delta T_{TEG} = \frac{\Delta T_0}{1 + \dfrac{K_{con}}{K_{TEG}} + (m\alpha)^2 \, \overline{T} \, K_{con} \, \dfrac{1}{R_l + R_{el}}} \tag{3.17}$$

with $K_{con} = K_h + K_c$ corresponding to the entire thermal contact resistance and $\Delta T_0 = T_{0-h} - T_{0-c}$ to the externally applied temperature gradient.
An approximate and more straightforward relation between ΔT_{TEG} and ΔT_0 can be formulated by assuming a constant heat flux through the system (analogous to the voltage divider formula), neglecting the Joule heating and Peltier effect.

$$\Delta T_{TEG} = \frac{K_{TEG}}{K_{TEG} + K_{con}} \Delta T_0 \tag{3.18}$$

This last simplification implies that the produced power is small in comparison to the heat flux entering the generator (actually that no current is running) and holds only for small temperature gradients, TEGs with low conversion efficiencies and small K_{con}. In this simplified case, the output power will become

$$P_{out} = (m \, \alpha \, \Delta T_0)^2 \left(\frac{K_{TEG}}{K_{TEG} + K_{con}} \right)^2 \frac{R_l}{(R_l + R_{el})^2} \tag{3.19}$$

and the efficiency will be given by

$$\eta = (m\,\alpha)^2 \Delta T_0 \frac{(K_{TEG})^2}{K_{TEG} + K_{con}} \frac{R_l}{(R_l + R_{el})^2}$$ (3.20)

3.1.4 Impedance matching

The output power (Eq. 3.9) and the efficiency (Eq. 3.10) of a generator can be maximized by matching the electrical and thermal impedances. However, differentiating each equation separately will lead to different optimal impedance parameters, resulting in a maximal value for one or the other. For thin-film TEGs in low temperature waste heat applications, where the supply energy is free, maximizing the output power is of higher interest [9]. A comparison of power versus efficiency will be discussed in Section 3.1.5.

Electrical impedance matching

Maximizing the TEG output power $\partial P_{out}/\partial R_l = 0$ results in the matching of the external load to the impedance of the generator

$$R_l = R_{el}$$ (3.21)

However, Eq. 3.21 is only valid under open circuit conditions. When a load is applied and current is flowing, an effective electrical TEG resistance R_{eff} must be considered [104, 109, 110]

$$R_{eff} = R_{el} + (m\,\alpha)^2 K_{TEG}\overline{T}_m \frac{K_{con}}{K_{TEG} + K_{con}} = R_{el}\left(1 + Z\overline{T}_m \frac{K_{con}}{K_{TEG} + K_{con}}\right)$$ (3.22)

which can be derived from inserting Eq. 3.17 in Eq. 3.9 and taking the derivative with respect to R_l. This is a result of the current dependence of $\dot{Q}_{in}$ and $\dot{Q}_{out}$, and therefore ΔT_{TEG} caused by the Peltier effect. Note that R_{eff} is also dependent on the TEG and contact thermal resistances K_{TEG} and K_{con}, respectively. By introducing the ratio $X = K_{con}/K_{TEG}$, R_{eff} can be rewritten as

$$R_{l\_opt} = R_{eff} = R_{el}\left(1 + Z\overline{T}_m \frac{X}{X+1}\right)$$ (3.23)

If $X \to 0$ then $R_{eff} \to R_{el}$, if $X \to \infty$ then $R_{eff} \to R_{el}(1 + Z\overline{T}_m)$.
Figure 3.4 a) shows the TEG output power with respect to the load resistance for $Z\overline{T}_m = 1$ and $X = 1$. The maximum power point in the graph corresponds to the
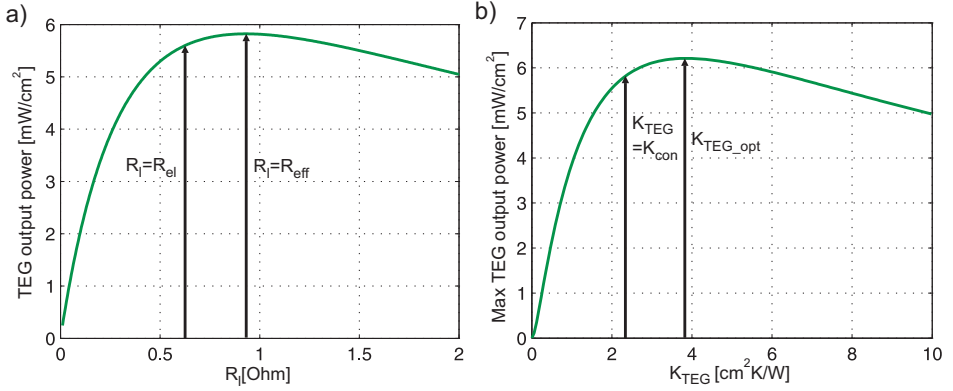
Figure 3.4: a) TEG output power as a function of the load resistance R_l for $Z\overline{T}_m = 1$ and $X = 1$. b) TEG output power as a function of the generator's thermal resistance K_{TEG}. For the change of K_{TEG}, the TC length l_{TEG} was varied. The simulations were performed for a $K_{con} = 2.35\,\text{cm}^2\text{K/W}$ and $\Delta T_0 = 10\,\text{K}$, the remaining parameters are found in Tab. B.1 in App. B. The optimal load and thermal TEG resistance differ from the impedance matching of the open circuit solution.

maximal TEG output power under matched effective electrical load

$$P_{max} = (m\,\alpha\,\Delta T_0)^2 \left(\frac{K_{TEG}}{K_{TEG} + K_{con}}\right)^2 \frac{1}{4R_{eff}} = \frac{(m\,\alpha\,\Delta T_0)^2}{4R_{eff}} \left(\frac{1}{1+X}\right)^2 \quad (3.24)$$

To show the impact of R_{eff} in comparison to the often used load matching for open circuit conditions [111–114] from Eq. 3.21, the relative increase of the output power ΔP_{max} for $R_l = R_{eff}$ is calculated for different $Z\overline{T}_m$ and X values and summarized in Table 3.1. The parameter combination closest to the experimental

Table 3.1: Impact of R_{eff} on P_{out} for different $Z\overline{T}_m$ and X ($R_{el} = 0.62\,\Omega$). Bold values mark the parameter combination closest to the experimental measurements in Chap. 5.

$Z\overline{T}_m$ [-]	**X** [-]	R_{eff} [Ω]	ΔP_{out} [%]
1	1	0.93	4.2
0.5	1	0.78	1.2
0.2	**1**	**0.68**	**0.2**
1	20	1.21	11.6
0.5	20	0.91	3.9
0.2	20	0.74	0.8

measurements performed in this thesis is marked in bold. It can be concluded that at this operating point, the introduced error is negligible. However, for higher $Z\overline{T}_m$ and X values, e.g. in energy harvesting applications for autonomous systems, R_{eff} should be considered as a relevant parameter for system optimization.

Thermal impedance matching

Equivalent to the electrical load matching, also thermal resistance matching can be applied. If a certain thermal contact resistance K_{con} is given, the TEG thermal resistance K_{TEG} can be adapted to further maximize the output power of a TEG.

In the simplified model under open circuit conditions, the maximal power can be expressed by replacing $R_l = R_{el}$ with $m^2 \, \alpha^2 \, K_{TEG} \, / \, Z_m$ according to Eq. 3.7

$$P_{out} = \frac{\Delta T_0^2 \, Z}{4} \frac{K_{TEG}}{(K_{TEG} + K_{con})^2} \tag{3.25}$$

Maximizing the TEG output power $\partial P_{out}/\partial K_{TEG} = 0$ yields [30, 115]

$$K_{TEG} = K_{con} \tag{3.26}$$

If a current is running and the effective ΔT_{TEG} is reduced by the Peltier effect, the optimal K_{TEG} can be calculated from [78, 89, 110]

$$K_{TEG\_opt} = K_{con} \sqrt{1 + Z\overline{T}_m} \tag{3.27}$$

and the optimal R_{eff} becomes in the case of a thermally matched system

$$R_{eff\_opt} = R_{el} \sqrt{1 + Z\overline{T}_m} \tag{3.28}$$

resulting in a maximal output power

$$P_{max\_opt} = \frac{\Delta T_0^2 \, Z_m}{4 \, K_{TEG}} \frac{1}{(1 + \sqrt{1 + Z\overline{T}_m})^2} \tag{3.29}$$

Figure 3.4 b) shows the output power with respect to the thermal TEG resistance for a module with $Z\overline{T}_m = 1$. For small $Z\overline{T}_m$, the difference between the power at $K_{TEG} = K_{con}$ and K_{TEG_opt} will again become negligibly small.

Note that the thermal impedance matching works only by adapting K_{TEG} to

K_{con} and not vice-versa. Reducing K_{con} independent of K_{TEG} will always lead to a higher output power.

3.1.5 TEG model conclusions and considerations

The above presented model allows us to highlight important design aspects relevant for this work. In the following section, the impact of the thermal contact resistance, the geometric parameters of the module and the different thermoelectric material parameters on the TEG output performance will be discussed.

Impact of thermal contact resistance

For waste heat recovery applications where fluidic heat transfer systems (HTSs) can be applied, low thermal contact resistances are feasible (see system comparison in Sec. 1.2). Figure 3.5 shows the impact and interdependence of K_{con} and K_{TEG} on the TEG output power. By reducing K_{con}, the output power enhancement benefits in two ways. First, a higher effective gradient across the generator
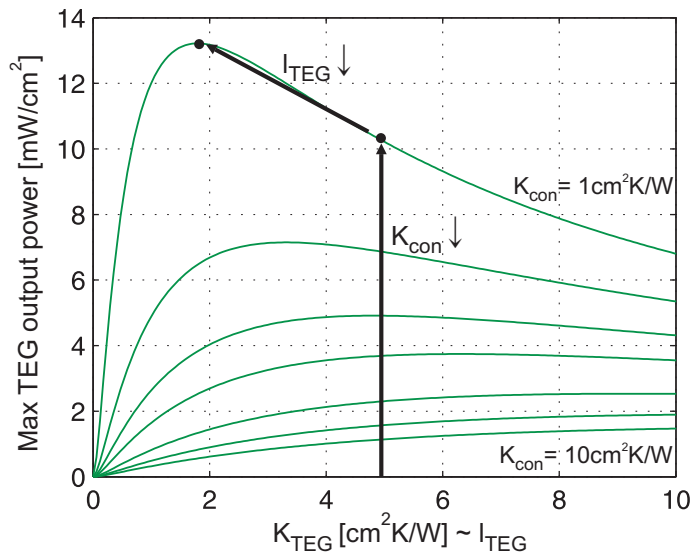
Figure 3.5: TEG output power as a function of the generator's thermal resistance K_{TEG} for different contact resistances K_{con} (1-10 cm^{2}K/W, in steps of 1 until 4 cm^{2}K/W and steps of 2 above) at $\Delta T_0 = 10$ K. For the change of K_{TEG}, the TC length l_{TEG} was varied. Relevant simulation parameters are found in Tab. B.1 in App. B. With decreasing K_{con} and reducing l_{TEG} for thermal impedance matching, P_{max} is significantly enhanced.

thus a higher power output (see Eq. 3.18 and Eq. 3.29) can be reached, correspond-
ing to the vertical arrow in the center of Figure 3.5. Second, it allows for a re-
duction of K_{TEG} by decreasing the TC length, i.e. generator thickness, to reach a
thermally matched system (diagonal arrow to upper left). By decreasing the thick-
ness of the TEG to the micrometer range, the heat flux through the generator is
significantly increased. This enables the application of thin-film generators, sav-
ing material, weight and cost.

Optimal TEG geometrical parameters

The thermal and electrical resistance of a generator depends not only on material
properties, but also on geometrical parameters (see Eq. B.1 - Eq. B.6 in App. B).
The two main geometrical parameters, the TC length l_{TEG} and TC diameter
d_{TEG}, can be adjusted to maximize the power output by electrical and thermal
impedance matching. Additionally, the spacing between the piles s, i.e. the pile
density must be considered. This can be expressed with the ratio between the
inactive (e.g. air or polymer mold) and active (TC) material of the generator AV.
For a fixed area of the TEG, the corresponding number of thermocouples can be
calculated from the diameter and the AV-ratio (see Eq. B.2 in App. B).

   When the interconnect resistance R_{ic} of the module is neglected, the output
power per area for a fixed AV-ratio is independent of the diameter as shown
in [27, 114] (see dashed green line in Fig. 3.6 a)). In this ideal case, only a
reduction of the AV-ratio will lead to a power increase. In a more realistic case,
where interconnect resistances are considered, minimizing the diameter (i.e.
maximizing the number of TCs) will enhance the output power as indicated by
the dotted green line in Figure 3.6 a). This can be explained with a smaller R_{ic} per
TC for smaller diameters, resulting from a shorter spacing between the piles for
a constant AV-ratio. With increasing thickness of the interconnect, i.e. reduction
of R_{ic}, this effect will become less pronounced.
 In practice, however, it is difficult to maintain a constant AV when the diameter
is reduced. The limiting factor caused by fabrication constrains is the minimal
distance between the pile s. By fixing s to a certain minimal value, an optimal
diameter can be found, as shown by the green solid line in Figure 3.6 a). For
a specific contact resistance, geometric constrains of s and material properties
of the module, an optimal combination of the TC length l_{TEG} and diameter
d_{TEG} will result in an optimal output power as indicated in Figure 3.6 b). With
decreasing TC length, the electrical resistance of the module R_{el} will decrease
and thus its negative impact on the output power will be reduced. Therefore,
smaller TC diameters and thus a larger amount of TCs will be favorable.
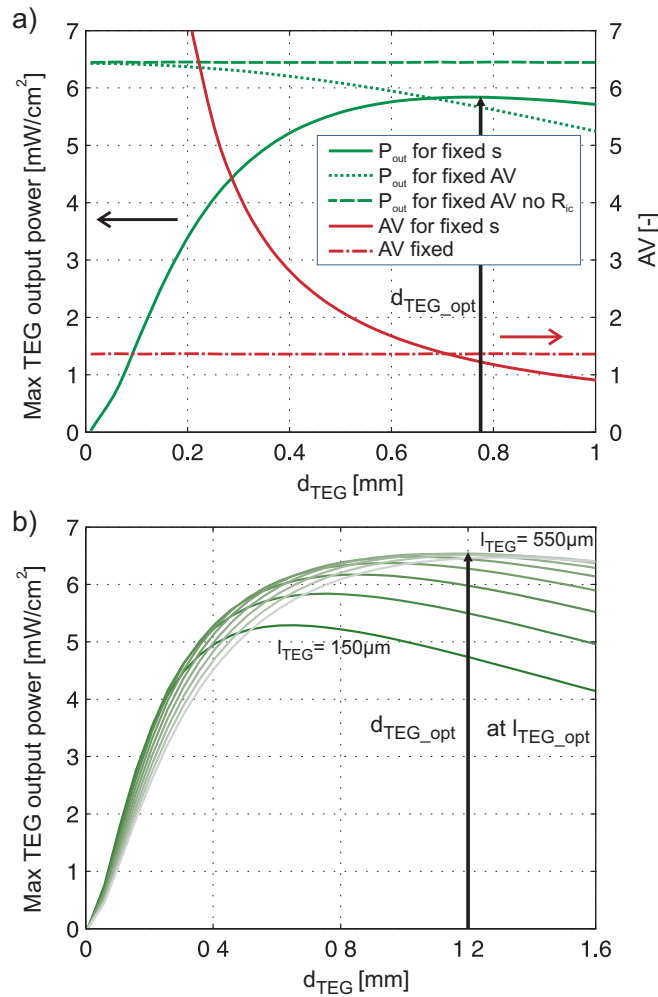
Figure 3.6: a) TEG output power (green lines) and *AV*-ratio (red lines) as a function of the TC diameter d_{TEG} for a fixed *AV*-ratio (dotted and dashed lines) and fixed minimal pile distance s (solid line). b) TEG output power as a function of the TC diameter d_{TEG} and length l_{TEG} at a fixed $s = 330\,\mu m$. The simulations were performed for a $K_{con} = 2.35\,cm^2K/W$ and $\Delta T_0 = 10\,K$, the remaining parameters are found in Tab. B.1 in App. B. When the minimal pile distance is the limiting fabrication parameter, an optimal TC diameter in combination with an optimal TC length exists.

Note that for energy harvesting applications, where $X >> 1$, working with a fixed area of the generator is not advisable, therefore different sets of optimal parameters will be valid.

Impact of thermal conductivity

The figure of merit $Z\overline{T}$ is a well established value to compare thermoelectric materials. However, in applications with low contact resistances and high heat fluxes, this standard value should be reconsidered. When working with very small K_{con}, the importance of low thermal conductivities is reduced.

Figure 3.7 shows the relative TEG output power plotted as a function of the thermal conductivity λ of the thermoelectric material for different thermal contact resistances. The relative power is normalized to a generator output power value potentially achieved with a very low thermal conductivity of $\lambda = 0.2\,\mathrm{W/mK}$ (e.g. in a superlattice structure [24]). The relative impact of an increase in λ decreases with reduced K_{con}. In the ideal case of $K_{con} = 0$, ΔT_{TEG} becomes ΔT_0 (see Eq. 3.17) and the output power becomes a function of only the thermopower $m\alpha$, the electrical resistance R_{el} (also R_l if not matched) and the externally applied ΔT_0 (see Eq. 3.9). Therefore, when working with very low contact resistances, the material optimization efforts should shift from the increase of the figure of merit $Z\overline{T}$ to the enhancement of the power factor $PF = \alpha^2/\rho_{el}$. This would in particular refer to nanostructured composites [116, 117] and superlattice structures
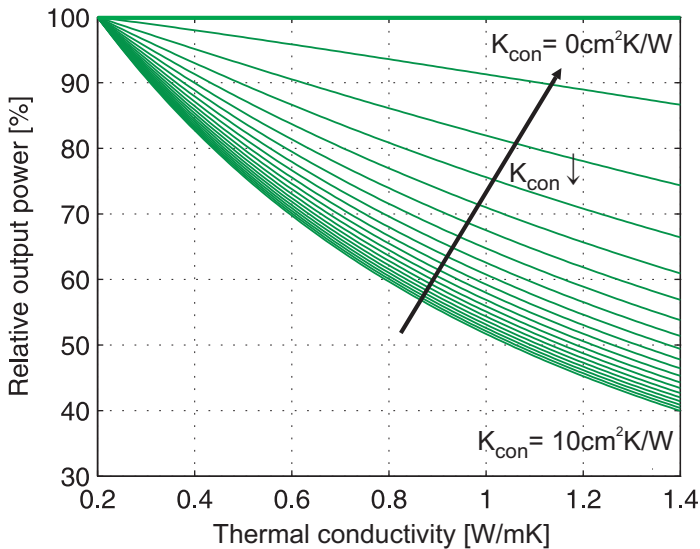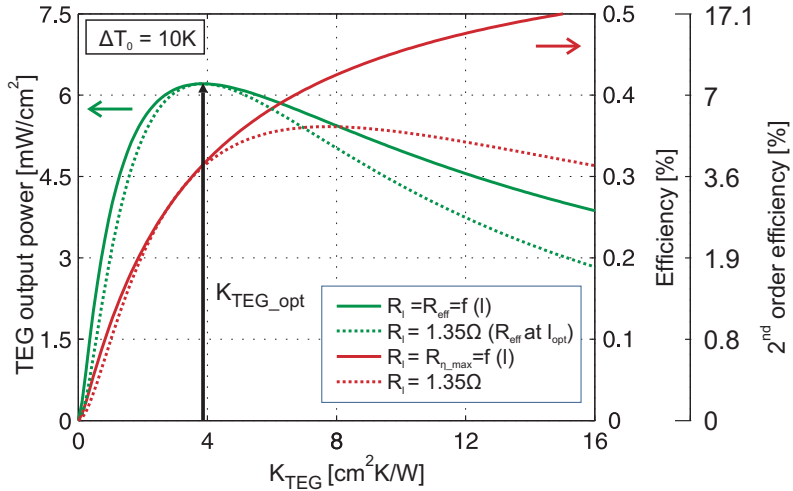

Figure 3.7: Relative TEG output power as a function of the thermal conductivity λ and the thermal contact resistance K_{con} (0-10 cm^{2}K/W, in steps of 0.5 cm^{2}K/W), referring to the value of $\lambda = 0.2\,\mathrm{W/mK}$. Relevant simulation parameters are found in Tab. B.1 in App. B. With $K_{con} \to 0$, the impact of λ on the output power $\to 0$.

[24, 25, 118], where an improvement of $Z\overline{T}$ is mainly achieved by the reduction of λ. This conclusion is in agreement with [119], where the much higher relevance of the power factors over the $Z\overline{T}$ value, especially for high heat flux applications, was also emphasized.

Maximal power vs. efficiency

As mentioned above, the optimal TEG parameters will vary for maximal power or maximal efficiency. Figure 3.8 shows the TEG output power (green lines) and TE conversion efficiency (red lines, see Eq. 3.10) with respect to the generator's thermal resistance K_{TEG} for two cases: (1) the ideal external load that is matched to the TEG electrical resistance for maximal power (R_{eff}) and maximal efficiency (R_{η_max} [89]) (solid line) and (2) a fixed load resistance as imposed by the system's application (dotted line). In the first case, the load resistance is a linear function of the TC length and therefore increases with increasing K_{TEG}. A maximal output power will be found at an optimal K_{TEG} (i.e. l_{TEG}) matching the thermal contact resistance (as discussed in Sec. 3.1.4 and 3.1.5). The efficiency, however, is continuously growing with increased thermal resistance of the generator. This

Figure 3.8: TEG output power (green lines), efficiency η and 2nd order efficiency η_{2nd} (red lines) as a function of the generator's thermal resistance K_{TEG} for the electric load R_l optimally match to the TEG's resistance (solid lines) and for a fixed $R_l = 1.35\,\Omega$ (dashed lines). The simulations were performed for a $K_{con} = 2.35\,cm^2K/W$ and $\Delta T_0 = 10\,K$, the remaining parameters are found in Tab. B.1 in App. B. The optimal R_l and K_{TEG} for maximal power and maximal efficiency due not coincide.

can be explained most directly with the basic open circuit model. By entering $R_l = R_g$ (Eq. 3.21) in Eq. 3.20 and replacing R_l with $m^2 \alpha^2 K_{TEG} / Z_m$ (Eq. 3.7), the efficiency can be simplified to

$$\eta = \frac{Z_m \Delta T_0}{4} \frac{K_{TEG}}{K_{TEG} + K_{con}} \tag{3.30}$$

Therefore, with increasing K_{TEG}, η will asymptotically converge to the maximal theoretical value of $Z_m \Delta T_0 / 4$. For a given load resistance, an optimal K_{TEG} or TEG thickness will exist, where the efficiency is maximal. This, however, does not correspond to the optimal thickness for maximal power.

To put the thermal efficiency in perspective with the theoretically reachable value limited by the Carnot efficiency, the scale of the 2nd order efficiency η_{2nd} (see Eq. 3.11) is added in Figure 3.8. Since the Carnot efficiency is dependent on ΔT_{TEG}, the scales of η and η_{2nd} are not linear.

3.2 Micro heat transfer system

The second component of the thermoelectric heat exchanger is the micro heat transfer system (µHTS), which is responsible for the thermal coupling of the TEG to the hot and cold fluid. The following section will review the basic fluid dynamic theory as well as describe the modelling of the system.

3.2.1 Fluid dynamics in confined ducts

As a basis for the micro heat transfer system model, the fundamental theory behind convective heat transfer and hydrodynamic losses in confined ducts will be introduced.

In order to characterize the relevant flow regimes, i.e. distinguish between laminar and turbulent flow, the dimensionless Reynolds number (Re) is used. The Reynolds number describes the balance between viscous and inertial forces, and therefore relates to flow instability

$$\text{Re} = \frac{u \, d_{ch}}{\nu} \tag{3.31}$$

where u is the mean velocity of the fluid, d_{ch} is the characteristic length of the channel and ν is the kinematic viscosity of the fluid. In circular ducts, the transition from laminar to turbulent flow starts at Re $\approx$ 2300, but fully turbulent conditions are reached at much higher Reynolds numbers (Re $\approx$ 10000) [120].

For rectangular ducts, the transition depends on the channel aspect ratio and can vary between 1850 and 2800 [121]. In microsystems, where the characteristic length scales are typically very small ($d_{ch} \sim 10^{-6}$), the Reynolds number usually lies well below this transition point.

Another important consideration is to distinguish between a developing flow in the duct entrance region, and a fully developed flow. This distinction is relevant for the selection of an appropriate heat transfer model, as well as a friction model for pressure drop calculations. In short channels as in the discussed µHTS, the total channel length can be smaller than the hydrodynamic and thermal entrance region.

Hydrodynamics

The fluid entering a duct has a uniform velocity profile over the cross section. Imposed by viscous forces at the walls of the duct (no-slip condition), a hydrodynamic (momentum) boundary layer starts to grow along the flow directions (see Fig. 3.9). The hydrodynamic entrance length l_h is the region where the flow develops from the inlet velocity to 99 % of the free-stream bulk velocity. From this point on, the flow is fully developed and the velocity profile stays constant along the flow direction [122].
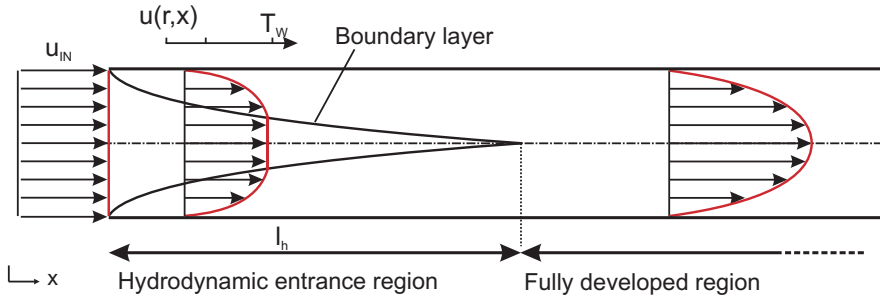
Figure 3.9: Hydrodynamic boundary development in a duct with laminar flow. Reproduced according to [120].

Solving Poisson's equation (reduced Navier-Stokes) for laminar flow and incompressible fluids, the general expression for the pressure loss in a straight duct with a constant arbitrary cross section can be expressed by [120]

$$\frac{\partial p}{\partial x} = -\frac{4f}{d_{ch}} \frac{1}{2} \rho_f u_{ch}^2 = -2f \frac{\rho_f u_{ch}^2}{d_{ch}} \qquad (3.32)$$

29

where u_{ch} is the mean fluid velocity, ρ_f is the density of the fluid and f is the Fanning friction factor. In non-circular ducts, the characteristic length d_{ch} corresponds to the hydraulic diameter. It has been shown, however, that in a laminar flow regime it is more precise to use the square root of the cross sectional area rather than the hydraulic diameter [123].

In order to distinguish the friction factor in developing flow (f) from the one in the fully developed flow, an apparent friction factor f_{app} was introduced [122]. Additionally to shear stress at the wall, the pressure drop in a developing flow is also caused by fluid acceleration. An expression of the apparent friction factor for laminar developing flow in non-circular ducts is provided by [124, 125] (see Eq. B.11 in App. B).

Convective heat transfer

Convection is a heat transfer mechanism by a fluid in motion. It describes the combined effects of heat conduction due to molecular interactions (i.e. diffusion) and energy transport by the bulk fluid flow motion [120].

Similar to the hydrodynamic boundary layer, a thermal boundary layer builds up. Figure 3.10 shows the development of the thermal boundary layer in a duct with constant wall temperature T_w and laminar fluid flow. The initially uniform fluid temperature T_f gradually evolves to a temperature profile with a T_f adjacent to the wall equal to T_w and a bulk fluid temperature in the middle of the duct. In the thermal entrance region, the boundary layer thickness is small and thus the temperature gradient between the wall and the fluid is large, resulting in an enhanced heat transfer compared to a thermally fully developed region. The hydrodynamic and the thermal boundary layers can affect each other, however the lengths of the entrance regions are often different.

Analogous to Fourier's law of heat conduction (see Eq. 3.15), convective heat transfer can be expressed by Newton's law of cooling [126]

$$\dot{Q}_{conv} = h_{conv} \left(T_f - T_w \right) \tag{3.33}$$

where h_{conv} is the convection heat transfer coefficient defined as

$$h_{conv} = \frac{\lambda_f \text{Nu}}{d_{ch}} \tag{3.34}$$

with λ_f being the thermal conductivity of the fluid and Nu the Nusselt number. The Nusselt number describes the ratio between convective and conductive heat transfer. For simultaneously developing flow in a duct under constant wall heat
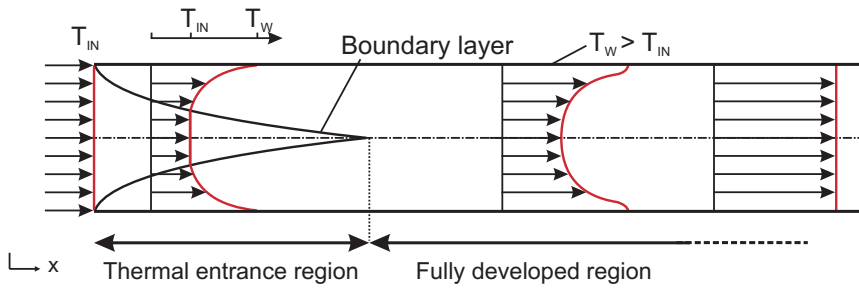
Figure 3.10: Thermal boundary development in a heated duct with constant wall temperature and laminar flow. Reproduced according to [120].

flux boundary condition, a Nusselt number correlation was provided by [127] (see Eq. B.12 in App. B for exact Nu definition).

Microfluidic considerations

From Eq. 3.32 and Eq. 3.34 it can be deducted that reducing the channel dimensions to the micrometre scale will significantly increase the heat transfer coefficient as well as the pressure losses. Additionally, an increase of the effective heat exchange area by high aspect ratio microchannels will further enhance the thermal performance. By decreasing the microchannel dimensions, the question arises until which point the classic theory based on thermodynamic equilibrium and continuum, formulated from the observation of macroscopic flow and heat transfer processes, is still valid. The onset of its failure has been widely discussed; however it is not well defined for liquids in microchannels. Many authors report large deviation from the conventional theory [128–130] attributing it to several microscale phenomena such as surface roughness [131–133], viscous heating effects [134], electrokinetic forces [135] or an early transition from laminar to turbulent flow [131, 136]. On the other hand, various papers confirm the validity of the classic theory [32, 137–144] for channel length scales as low as 4.5 μm [145]. Concluding from the inconsistent published results, potential microscale effects must be kept in mind.

3.2.2 Basic micro heat transfer system model

The generic part of the one-dimensional μHTS model is based on [44, 146]. Therefore, only the basic concept will be described in this section, further details can be found in [44, 146]. The introduced model extensions and optimizations will be covered in more detail in the following section.

Analogous to the theory section above, the model is divided in two parts: a thermal and a hydrodynamic model. Figure 3.11 depicts the schematic cross section of the µHTS and of a periodic microchannel unit cell showing the thermal and hydrodynamic model contributions and relevant design parameters.
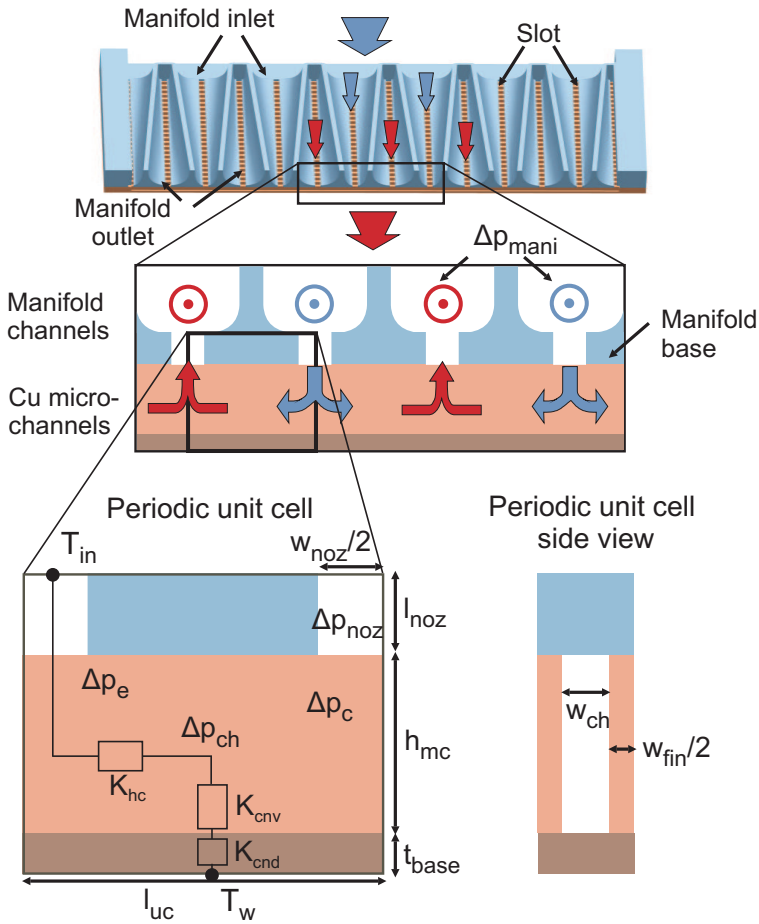
Figure 3.11: Schematics of the µHTS with an enlargement of the microchannel unit cell showing the thermal and hydrodynamic model contributions and relevant design parameters.

Thermal model

The thermal model of the µHTS is based on the concept of a thermal resistance network simplified to one-dimensional heat transfer. It is assumed that the heat transfer takes place only inside the copper microchannels and that no heat exchange occurs between the channels and the polymer manifold (i.e. adiabatic boundary conditions).

The total heat transfer resistance K_{HTS} of the µHTS consists of the conductive resistance through the microchannels K_{cnd}, the convective resistance at the fluid-channel interface K_{cnv}, and the fluid resistance due to its limited heat capacity K_{hc} (compare unit cell in Fig. 3.11)

$$K_{HTS} = K_{cnd} + K_{cnv} + K_{hc} \tag{3.35}$$

The conductive resistance term is given by

$$K_{cnd} = \frac{t_{base}}{\lambda_{Cu}} \tag{3.36}$$

where t_{base} is the thickness of the microchannel chip base and λ_{Cu} is the thermal conductivity of copper. Due to the a large value of λ_{Cu}, the contribution of K_{cnd} to K_{HTS} is small.

The convective thermal resistance is composed of three main parts: convection at (1) the base, (2) at the fins and (3) at the fin top in the channel entrance region. The last term was added to the original version in [44, 146], based on findings from 3D-FEM simulation results of the microchannel unit cell (see Sec. 3.2.4 for more details).

$$K_{cnv} = \frac{A_{uc}}{\bar{h}_{base} A_{base} + 2\eta_f \bar{h}_{fin} A_{fin} + \bar{h}_{fin\_top} A_{fin\_top}} \tag{3.37}$$

where $\bar{h}_{base}$, $\bar{h}_{fin}$ and $\bar{h}_{fin\_top}$ are the average convective heat transfer coefficients of the base, fin and the fin top, respectively, A_{xy} are the corresponding surface areas and η_f is the fin efficiency (see Eq. B.14 in App. B for the exact definition). The Nusselt number correlation for laminar developing flow are implemented according to [127] and for laminar jet impingement according to [147].

The bulk fluid resistance K_{hc} caused by the heating up of the fluid as it absorbs energy flowing through the channel, is expressed as

$$K_{hc} = \frac{A_{uc}}{\bar{c}_p \bar{\rho}_f \dot{V}_{mc}} \tag{3.38}$$

33

where $\bar{c}_p$ is the mean specific heat capacity of the fluid, $\bar{\rho}_f$ is the fluid density and $\dot{V}_{mc}$ is the volumetric flow rate through the microchannel.

Hydrodynamic model

The pressure losses in the μHTS are composed of the losses inside the microchannel unit cell Δp_{mc} and the tapered manifold distribution channels Δp_{man}. In the unit cell, several pressure drops contribute to the overall Δp_{mc}: the frictional pressure losses in the straight microchannel Δp_{ch} as well as in the inlet and outlet nozzles Δp_{noz}, and the pressure losses induced by sudden expansion and constriction at the microchannel entrance Δp_e and exit Δp_c (see microchannel unit cell in Fig. 3.11).

$$\Delta p_{mc} = \Delta p_{ch} + 2\,\Delta p_{noz} + \Delta p_c + \Delta p_e \tag{3.39}$$

The expressions for the different pressure drop contributions in straight parts of the microchannel are based on Eq. 3.32 from Section 3.2.1 and are defined as [148]

$$\Delta p_{ch} = \frac{2\,f_{app-ch}\,\bar{\rho}_f\,u_{ch}^2\,l_{ch}}{d_{ch}} \tag{3.40}$$

$$\Delta p_{noz} = \frac{2\,f_{app-noz}\,\bar{\rho}_f\,u_{noz}^2\,l_{noz}}{d_{noz}} \tag{3.41}$$

$$\tag{3.42}$$

The losses related to sudden expansion and constriction can be formulated as [149]

$$\Delta p_c = \frac{1}{2}\rho_f\left(u_{narrow}^2 - u_{noz}^2\right) + \frac{1}{2}C_c\,\bar{\rho}_f\,u_{narrow}^2 \tag{3.43}$$

$$\Delta p_e = \frac{1}{2}\rho_f\left(u_{narrow}^2 - u_{noz}^2\right) + \frac{1}{2}C_e\,\bar{\rho}_f\,u_{noz}^2 \tag{3.44}$$

where u_{narrow} is the mean velocity right at the channel entrance after leaving the nozzle and C_c and C_e are the loss coefficients associated with the abrupt contraction and expansion according to [149, 150].

The pressure drop in the tapered manifold is a function of the channel position, due to the varying channel width and continuous fluid outflow along the manifold channel

$$\Delta p_{man} = -2\int_0^{L_{man}} \frac{f_{app-mani}(x)\,\rho_f\,u_{man}^2(x)}{d_{man}(x)}dx \tag{3.45}$$

To solve the integral numerically, the manifold channel is divided into N_{ch} subdivisions with the length of $w_{ch} + w_{fin}$.

The pumping power of the μHTS was computed by multiplying the total hydrodynamic resistance Δp_{HTS} by the volumetric fluid flow $\dot{V}$

$$P_p = \Delta p_{HTS}\,\dot{V} = (\Delta p_{mc} + \Delta p_{man})\,\dot{V} \tag{3.46}$$

3.2.3 Model extensions

In order to model the μHTS more precisely, temperature changes inside microchannel and the manifold channel were added to the existing model.

Temperature profile inside the microchannels

Changes of the fluid temperature inside the microchannel have an impact on the fluid properties (in particular the fluid viscosity) and therefore the hydrodynamic and thermal performance of the system. Additionally, by introducing a temperature profile, the microchannel outlet temperature can be computed and used for the estimation of the inlet fluid temperature change along the manifold channel (see next section).

For this purpose, the microchannel unit cell was divided into an entrance region underneath the inlet nozzle (dark gray area in inset of Fig. 3.12 a)), a horizontal flow region along the microchannel (light gray area in insert of Fig. 3.12 a)) and an exit region (white area in inset of Fig. 3.12 a)). The regions are discretized into horizontal and vertical elements, respectively. The temperature of each element is calculated according to

$$T_{i+1} = T_i + q_i \frac{1}{\dot{m}_i c_{p,i}} = T_i + \frac{A_i\,dx\,h_i\,(T_w - T_i)}{\dot{V}_{ch}\,\rho_i\,c_{p,i}} \tag{3.47}$$

where T_i is the local fluid temperature, q_i is the local heat flux from the channel base and fins, A_i is the local heat transfer area, dx is the length of the subdivision and h_i is the local convective heat transfer coefficient. A constant temperature at the copper channel walls T_w is assumed, corresponding to the temperature at the channel base. For the calculations of K_{cnv}, the average convective heat transfer coefficient of all elements is used.

Figure 3.12 a) shows the temperature profile along the flow path inside a microchannel unit cell computed by 3D-FEM simulations and by the one-dimensional model. The first region corresponds to the nozzle inlet, where the heat flux from the manifold base is negligible. The heat transfer in the entrance region is affected by jet impingement at the fin top and channel base,
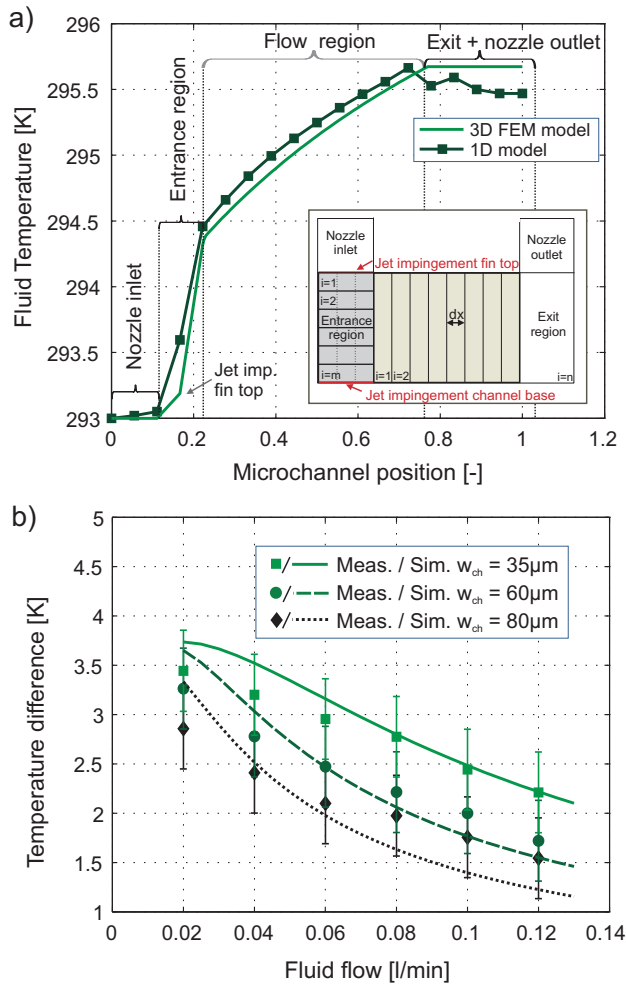
Figure 3.12: a) Comparison of the temperature increase inside the microchannel unit cell between the 1D model (symbols with line) and the 3D-FEM simulation (line only) for a small size μHTS with a $w_{ch} = 80\,\mu$m at a fluid flow of 0.04 l/min. Inset: Division and discretization of the unit cell in the 1D model. b) Measurement and simulations of the temperature increase inside the μHTS microchannels for different channel widths and flow rates. The remaining μHTS parameters used for measurement and simulations are found in Tab. B.2 in App. B (MF I).

as well as by convection from the fin wall. Inside the developing microchannel flow region, the temperature steadily increases. In the region underneath the nozzle outlet, no heat exchange is assumed in the 1D model. A good agreement between the 1D and 3D-FEM models can be found. Figure 3.12 b) compares the

1D model with the measured temperature increase between the inlet and outlet of 3 µHTSs with different channel sizes (see Sec. 4.2.1 for experimental settings). Considering the complexity of the complete system used and the influence of the measurement setup, the measurement results are in good agreement with the 1D model simulations. The µHTS measurements show a weaker fluid flow dependency indicated by a more linear trend compared to the 1D model.

Further comparison data of the temperature deviations for the 8 x 8 mm µHTS can be found in Table B.3 in Appendix B.

Inlet fluid temperature change

The initial model assumes a constant microchannel inlet temperature corresponding to the measured temperature at the manifold inlet. However, due to heat exchange from the copper microchannels and the manifold outlet channels, this assumption of adiabatic manifold boundary conditions leads to inaccurate performance predictions, in particular for low fluid flow rates.

The temperature change along the manifold inlet channel was calculated for N_{ch} subdivisions according to Eq. 3.47. The heat flux q_i into the manifold fluid consists of the heat coming from the manifold channel base and from the manifold outlet channel, where the microchannel fluid outlet temperature is used. The inset of Figure 3.13 a) shows the schematic thermal resistance model of the manifold inlet channel. The effective microchannel fluid inlet temperature is calculated by taking the average manifold inlet temperature. In Figure 3.13 a), the measured temperature differences between the manifold entrance and the channel end is compared to the computed values for different fluid flow rates. A good agreement between the measured and computed values can be found. The deviation can be related to the not precisely controllable location of the temperature sensing TC at the channel ends, large measurement error induced by the TC and possible parasitic heat fluxes (mainly from the cover of the manifold channels).
Figure 3.13 b) shows the impact of the manifold inlet fluid temperature on the heat transfer resistance of the µHTS with two different microchannel sizes. While the model with adiabatic manifold boundary conditions (dashed lines) displays substantial deviations from the measurements at lower fluid flow rates, the corrected model agrees much better with the measurement results.

Further comparison data of the 1D model to measurements of the 8 x 8 mm µHTS can be found in Table B.3 in Appendix B.
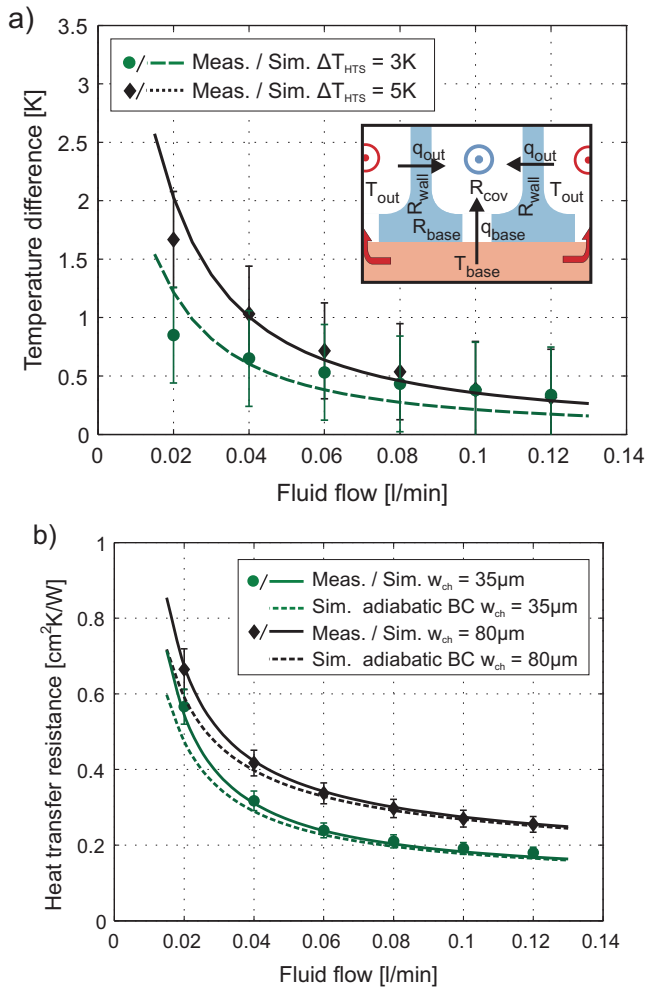
Figure 3.13: a) Measurement and simulations of the temperature increase inside the manifold channels of a small µHTS as a function of the flow rate for different ΔT_{HTS} applied ($w_{ch} = 80\,\mu m$). Inset: Schematic view of the heat fluxes contributing to the temperature change of the manifold inlet temperature. b) Comparison of the computed heat transfer resistance with adiabatic manifold conditions (dashed lines) and heat exchange in the manifold fluid inlet (solid line) to measurements of the small µHTS with two different channel sizes. The remaining µHTS parameters used for measurement and simulations are found in Tab. B.2 in App. B (MF I).

3.2.4 3D FEM unit cell model

In order to compare and optimize the heat transfer and hydrodynamic properties of the 1D model as well as to evaluate the potential of different μHTS design improvements, a 3D finite element method (FEM) model of the microchannel unit cell (see Fig. 3.11) was implemented in COMSOL Multiphysics ®.

The coupled physics interfaces of the 3D model consist of (1) steady-state incompressible Navier-Stokes with temperature dependent fluid variables and (2) general heat transfer for thermal conduction and convection. The major part of the simulations are performed with a symmetric half unit cell in order to reduce computational time. For channels with asymmetric structures, the entire unit cell was simulated. The fluid boundary conditions are set to a fixed fluid velocity at the nozzle inlet, an open boundary at the outlet (equal to zero pressure) and no slip at the channel walls. For the thermal boundaries, a constant fluid inlet and channel base temperature (T_w) is set and isolation/symmetry are used for all remaining boundaries. The heat transfer resistance is calculated by dividing the applied temperature between the inlet and the base by the total dissipated heat flux. The pressure losses are extracted from the average pressure at the nozzle inlet.

The parameter comparison between the 3D-FEM and the 1D model of the unstructured microchannels are found in Table B.3 in Appendix B.

μHTS design optimization

[1]By introducing microstructures and optimizing the fluid flow path inside the microchannel unit cell, a reduction of the thermal and hydrodynamic resistances can be achieved, leading to an overall increase in the power output of the thermoelectric heat exchanger (TEHEX).

Heat transfer enhancements can be achieved by increasing the convective surface area, augmenting the flow vorticity and limiting the growth of fluidic and thermal boundary layers [152]. For this purpose, two different microstructures are integrated into the microchannels: an additional pin-fin structure and triangular protrusions on the sidewall. While the first approach is expected to yield lower heat transfer resistances due to a higher convective surface area, the second one benefits from a simpler and more robust fabrication.
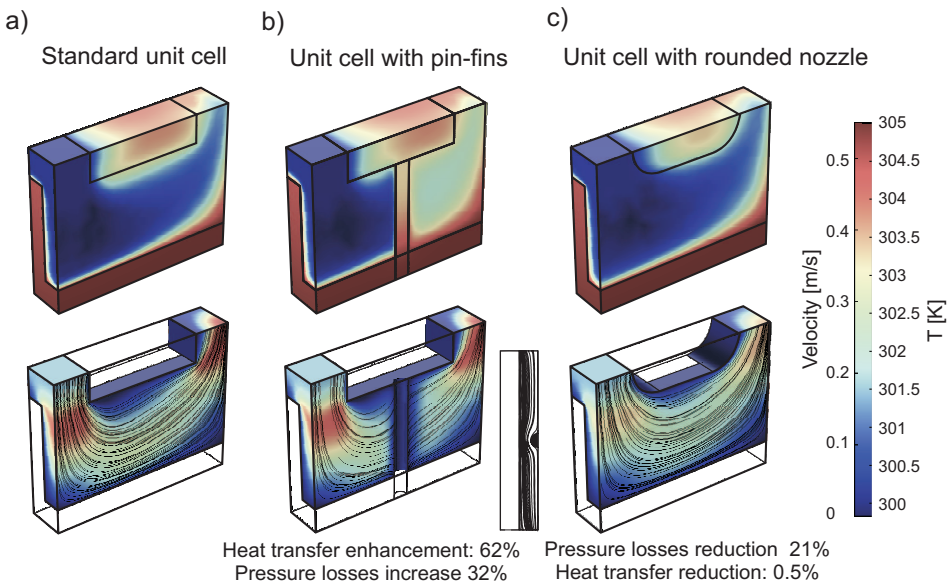Pressure losses can be reduced by a smart fluid path design. Avoiding abrupt

---

[1] The content of the μHTS design optimization by 3D-FEM simulations was published in the proceedings of Transducers 2013 [151] and was reproduced with permission. Copyright © 2013 IEEE.

expansions and constrictions at the microchannel entrance region can decrease the pressure drop without affecting the heat transfer inside the microchannels. Therefore, the geometry of the fluid inlet and outlet nozzle between the manifold and the microchannels is optimized, as well.

The 3D-FEM model of a microchannel unit cell introduced above is used to investigate the impact of the different design changes on the thermal and hydrodynamic performance of the μHTS. For this purpose, the dimensions and spacing of the introduced microstructures, the widths of the microchannels and the fluid flow rates were varied. In Figure 3.14, the temperature and velocity profiles for a microchannel with a) no additional structures (reference), b) pin-fin arrays, and c) with the rounded inlet/outlet nozzle design are depicted. In Figure 3.14 b) and c), the corresponding maximal change in heat transfer and pressure losses is shown with respect to the reference (Fig. 3.14 a)) at a fixed flow rate of 0.1 l/min. The temperature distribution of the pin-fin structures (Fig. 3.14 b)) shows a clear increase in heat exchange compared to an unstructured unit cell (Fig. 3.14 a)). The

a) Standard unit cell b) Unit cell with pin-fins c) Unit cell with rounded nozzle

Heat transfer enhancement: 62% Pressure losses reduction 21%
Pressure losses increase 32% Heat transfer reduction: 0.5%

Figure 3.14: 3D-FEM simulations of a microchannel unit cell showing the temperature profile and velocity profile at $\Delta T_0 = 5\,\text{K}$ and a flow rate of 0.1 l/min for a) a reference microchannel structure, b) a cell with pin-fins and c) with rounded nozzle. The exact microchannel dimensions and boundary conditions used for the simulations are found in Tab. B.4 in App. B. Copyright © 2013 IEEE.

cross cut of the velocity profile indicates an enhanced flow velocity in the constrictions around the pin-fins. Therefore, for the pin and the protrusion structures, the enhanced heat transfer results from the larger convective surface area, the increased fluid flow velocity around the introduced microstructures and resulting vortices at higher flow rates. The thermal resistance, however, is reduced at the expense of an increased hydrodynamic resistance. For the unit cell with rounded inlet/outlet nozzles (Fig. 3.14 c)), no significant change of the temperature profile is noticeable. However, a reduction of the flow velocity enabled by the smoother fluid path is achieved. This way, large pressure losses during expansion and constriction can be avoided, resulting in a significantly lower pumping power consumption.

Figure 3.15 shows the increase in heat flux (green solid lines) and pressure losses Δp (black dashed lines) of a microchannel unit cell with integrated pin-fin structures compared to an unstructured unit cell with equal dimensions and fluid flow rates. In Figure 3.15 a), the percentage increase is plotted as a function of the flow rate for one pin-fin per microchannel unit cell. With increasing flow rates, the relative increase in heat transfer rises, while Δp decreases. The first can be explained with an enhanced impact of the additional heat transfer surface and potential vortices formation at higher flow rates. Since the absolute pressure difference increase with increasing flow rates, the shown reduction in pressure losses can be mainly contributed to a reduced relative influence at higher pressure values. Figure 3.15 b) shows that the optimal pin-fin pitch approximately equals to one unit cell length. Denser spacing of the pin-fin results in a small additional enhancement in heat transfer but large increase in pressure losses. In Figure 3.15 c) and d), the impact of the pin diameter is depicted for four different microchannel widths. The largest difference between the increase in heat transfer and Δp is found at a pin-fin diameter between 30 % and 40 % of the microchannel width (decreasing with reducing channel size).

The most relevant simulation results are summarized in Figure 3.16. In order to show the interdependency between the heat transfer resistance and the corresponding pressure losses, both values are plotted for increasing flow rates between 0.02 and 0.12 l/min (from left to right). Microchannels of varying sizes without the optimization features are shown as a reference (black lines). With decreasing channel width, the curves progress from large K_{HTS} and low pressure loss (100 μm channels) to low K_{HTS} and large pressure loss (40 μm channels). For the channels with the introduced pin-fins structures (green lines), the curves shift towards a regime with low K_{HTS} and low pressure loss, demonstrating an overall system performance enhancement. The results also show that larger channels with pin-fin structures outperform the smaller unstructured channels. The
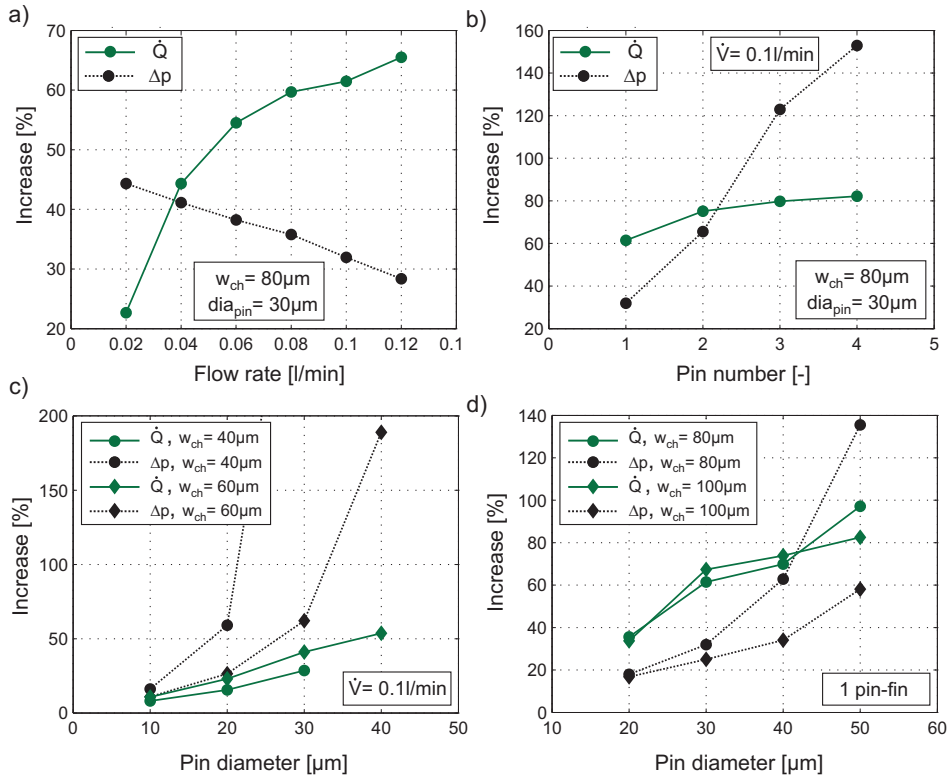
Figure 3.15: 3D-FEM simulations of a microchannel unit cell with integrated pin-fin structures showing the increase in heat flux (green solid lines) and pressure losses (black dashed lines) compared to an unstructured unit cell with same dimensions and flow rates for a) different fluid flow rates ($w_{ch} = 80\,\mu m$, 1 pin-fin), b) different pin-fin numbers ($w_{ch} = 80\,\mu m$, $\dot{V} = 0.1 l/min$) and c), d) different pin-fin diameters and channel widths ($\dot{V} = 0.1 l/min$, 1 pin-fin). The exact microchannel dimensions and boundary conditions used for the simulations are found in Tab. B.4 in App. B.

introduction of pin-fins inside channels below $80\,\mu m$ results in a minor system improvement, mainly due to a large pressure loss increase (see Fig. 3.15 d)). The best results can be achieved by combing the microstructures with the rounded inlet/outlet nozzles (red dashed line). The microchannels with protrusions on the sidewalls (gray line) also show a system improvement compared to unstructured devices; however, the effect is not as pronounced as with the pin-fin structures.
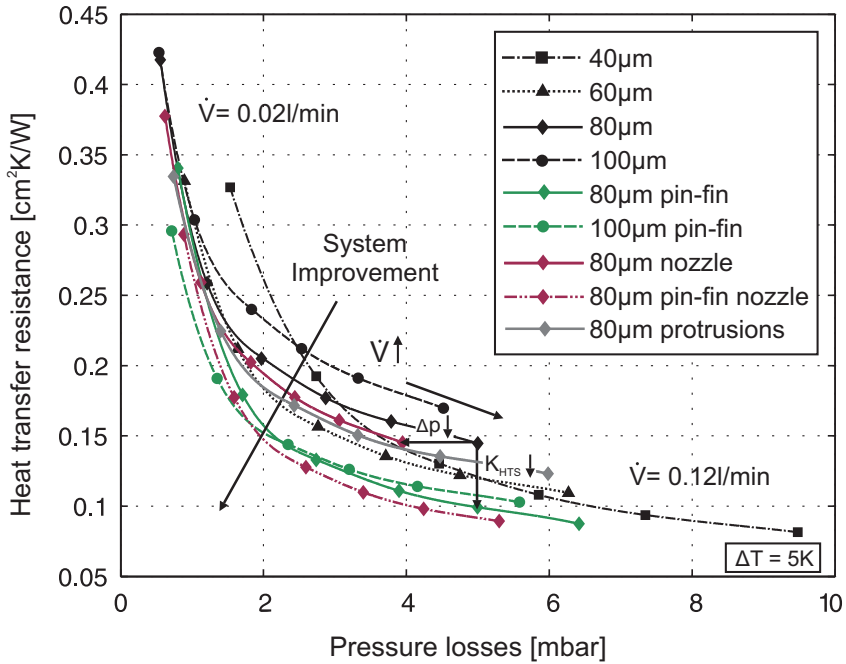
Figure 3.16: Summarized 3D-FEM simulations results showing heat transfer resistance versus pressure losses in a microchannel unit cell without structuring (black lines), with pin-fins (green lines), with sidewall protrusions (gray line) and with rounded nozzles (red lines) for fluid flow rates between 0.02 - 0.12 l/min. The channel height is 200 µm, the pin-fin diameter is 30 µm and the pitch is equal to one unit cell. Copyright © 2013 IEEE.

3.3 Thermoelectric heat exchanger model

The TEG and µHTS models are combined to a thermoelectric heat exchanger model. Figure 3.17 shows the equivalent thermal resistance network of a TEHEX unit cell with µHTSs at the cold and hot fluid sides and a generator in between.

Since the thermal resistance of the µHTS K_{HTS} is also a function of the initially unknown temperature at the microchannel base and wall $T_{w\_h/c}$, the system equations are solved iteratively to converge towards the actual temperature distribution. Figure 3.18 illustrates the computational routine of the combined TEHEX model. After calculating the total TEG thermal and electrical resistances from initial geometric and material parameters, the average microchannel inlet temperature $T_{in\_h/c}$ is computed in two steps. First, $T_{w\_h/c}$ and the microchannel fluid outlet temperature $T_{out\_h/c}$ are found under a constant heat flux
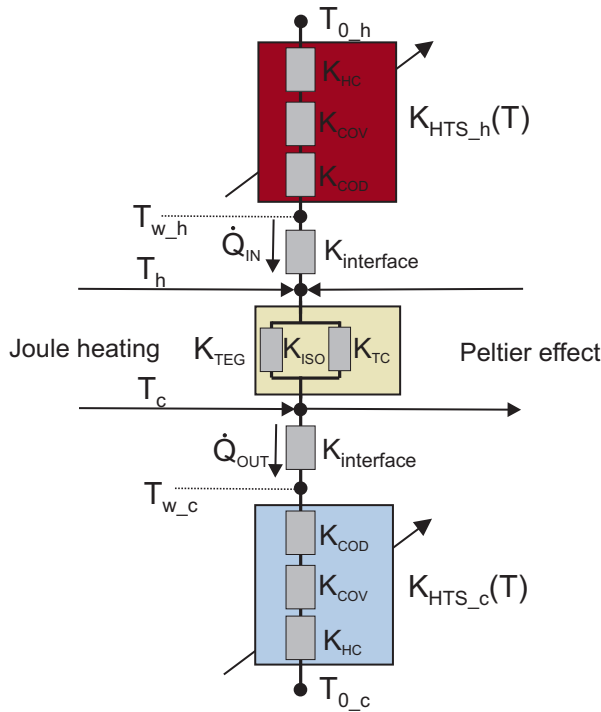
Figure 3.17: Equivalent thermal resistance network of a thermoelectric heat exchanger unit cell.

assumption through the TEHEX (see Eq. 3.18). Second, based on these values, the temperature change inside the manifold inlet channel is estimated and thus the new average $T_{in\_h/c}$ extracted. The corrected $K_{HTS\_h/c}$ is now computed and used to solve the heat balance equations for the TEG (see Eq. 3.12 - Eq. 3.16). With the resulting ΔT_{TEG}, the generator's total output power and, by further subtracting the pumping power, net power can be calculated.

The implemented model allows for the analysis and optimization of most geometric parameters and material properties of the TEG and µHTS by an integrated parameter sweep function.

3.4 Conclusions

The theoretical background necessary for a better understanding of the device modelling and measurement results is introduced.
By means of the 1D TEG model, the electrical and thermal impedance matching,
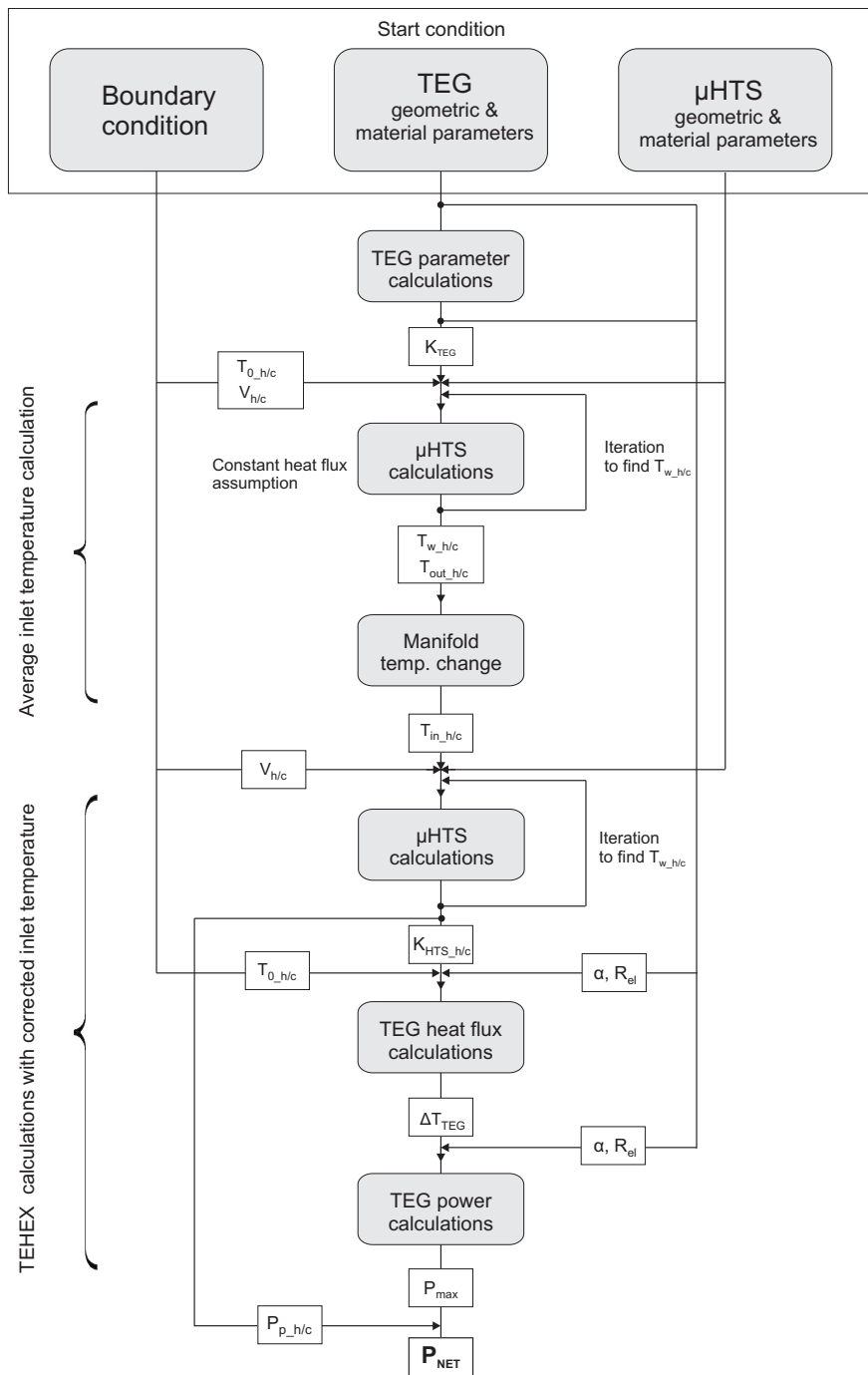
Figure 3.18: Flow chart explaining the computational procedure of the thermo-electric heat exchanger model.

impacts of the reduced thermal contact resistances on the TEG performance as well as important parameter correlations are discussed. Moreover, the reduced relevance of the thermal conductivity in the thermoelectric material with decreasing contact resistances is highlighted.

The existing thermal and hydrodynamic µHTS is extended with a discrete temperature profile inside the microchannels in order to account for the influence of temperature dependent fluid parameters as well as to correctly model the gradual fluid temperature change along the manifold channels. This extension significantly improves the agreement between measurements and model, in particular for the thermal performance at lower fluid flow rates.

Investigations on the improvement of the µHTS design by means of a 3D-FEM unit cell model yield an overall system performance enhancement by introducing high aspect ratio pin-fin structures and implementing a smoother fluid flow path. Finally, the iterative computational procedure of the combined TEHEX model is described and reveals the necessary complexity for accurate system modelling.

4 Fabrication and Experimental

The small and large size TEGs used for the measurements are provided by green-TEG AG and are fabricated and characterized according to [28]. The fabrication of the corresponding 8×8 mm and 9×9 cm µHTSs are described in the first part of this chapter. In the second part, the experimental settings are explained.

4.1 Thermoelectric heat exchanger fabrication

For the fabrication of the small and large size µHTSs, two different approaches are used. The objective of the small µHTS is to develop a high performance system featuring high aspect ratio microchannels in order to demonstrate the technological feasibility and limits of the thermoelectric heat exchanger. The focus of the large size fabrication is set on a straight forward, fast and reliable process in perspective of future commercialization.

4.1.1 Small size micro heat transfer system

[1]The two functional layers of the µHTS, the microchannel and the manifold structure are fabricated in separate processes and assembled on chip level.

**Microchannel fabrication**

The microchannels are fabricated by means of SU-8 based high aspect ratio photolithography and subsequent electrochemical deposition. The detailed process flow is illustrated in Figure 4.1. In the first step, 1 µm of Lift-Off resist (LOR) is spin coated on the wafer for a later release of the microchannels from the support. Next, a copper seed layer (1 µm) and a chromium adhesion layer (10 nm) are deposited by e-beam evaporation (Fig. 4.1 a)). The prepared seed wafer is coated with a 200 µm thick SU-8 3050 film. To improve the layer thickness homogeneity, the spin coating is performed in two steps of 100µm with an edge bead removal by γ-butyrolactone (GBL) after each step. In the subsequent photolithography (Fig. 4.1 b)), reduced baking temperatures as well as long cooling and additional relaxation times are applied for stress reduction in the SU-8. Due to the high aspect ratio and extended length of the mold structures, a reduced

---
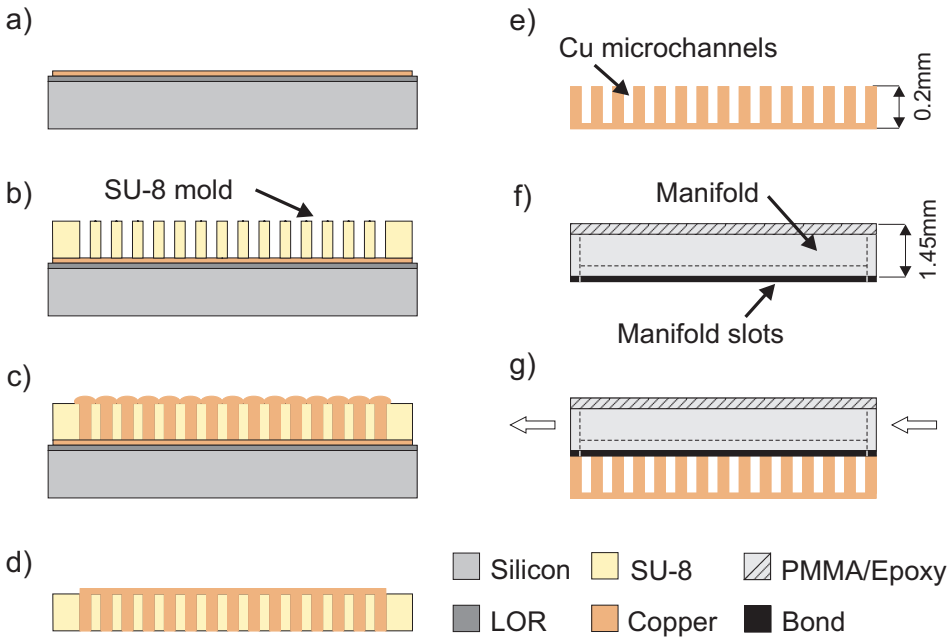
Figure 4.1: Fabrication process flow of the small size µHTS.

intrinsic stress level of SU-8 is crucial for the adhesion to the substrate. The structures are pre-developed in GBL for 5 minutes followed by an extended development (Dmr-Dev 600, micro resist technology GmbH) in an ultrasound bath in order to improve convection inside the high aspect ratio trenches. Figure 4.2 a) shows the results of a not optimized process based on the recommendation of the SU-8 3000 data sheet. The intrinsic stress inside the developed SU-8 leads to delamination from the substrate and lateral sticking of the thin and long beams. After process optimization, good adhesion of the microbeams to the substrate is achieved (Fig. 4.2 b)). Prior to the electrochemical deposition of copper, the structured mold is wetted by IPA, rinsed with DI water and immersed in 10 % nitric acid (HNO_3) for substrate cleaning and removal of a possible native oxide on the Cu seed layer. The copper microchannels are electrochemically grown in an acid copper sulfate bath (see bath composition in Tab. A.4 in App. A) at an applied current density of $3 \, A/dm^2$ resulting in an average growth rate of $0.3 \, \mu m/min$. The mold is overgrown in order to form the base of the microchannels (Fig. 4.1 c)). After a top surface planarization by mechanical polishing, the wafer is released from the support by sacrificial layer etching of the Lift-Off resist and separated into 8×8 mm chips (Fig. 4.1 d)). The seed layer peels off during the release pro-
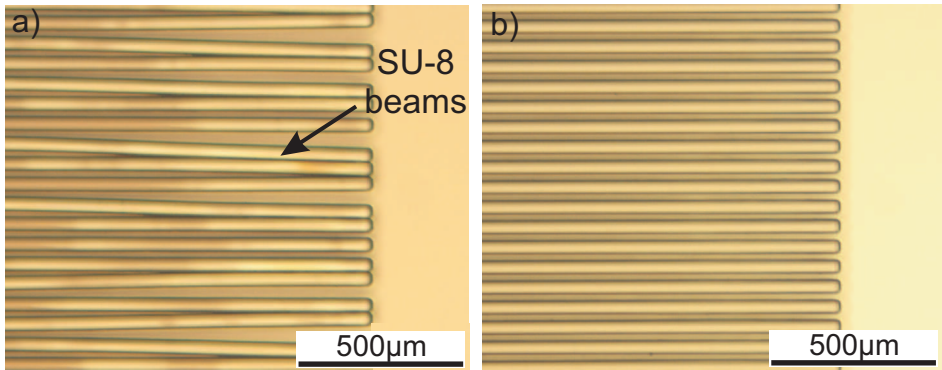
Figure 4.2: Optical microscopy pictures of the photolithographically structured SU-8 mold with beam widths of 35 µm. a) Delaminated/sticking beams fabricated with a not optimized fabrication process and b) good beam adhesion after process optimization.

cess. Finally, the SU-8 mold is removed by wet chemical etching and DI water ultrasound cleaning (Fig. 4.1 e)). The runsheet for the optimized microchannel fabrication process can be found Table A in Appendix A. Figure 4.3 a) shows the top view and b) a cross section view of a 30 ± 5 µm microchannel chip. The depicted channels have an aspect ratio of 7 at a total height of 210 ± 10 µm. The microchannel profile shows a narrowing at the bottom of the fins, which can be explained by UV light scattering at the mask edge during wafer exposure. The average surface roughness of the fin side walls measured by white light interferometry (WLI) is $Ra = 0.57 \pm 0.1$ µm. Microchannels with widths between 30 and 80 µm and a fin to channel width ratio of 1 were successfully fabricated for the experimental measurements.

Microchannels with integrated microstructures

The basic fabrication of microchannels with integrated microstructures for heat transfer enhancement (see Sec. 3.2.4) followed the process flow depicted in Figure 4.1. Additional process optimization and adaptations had to be made in order to address the challenges due to critical feature sizes for the mold preparation and electrochemical deposition of the high aspect ratio structures, in particular the pin-fins.

The copper structures are designed to have excess material after electroplating and are therefore isotropically etched after the SU-8 release in order to obtain the targeted dimensions. The wetting before the electrochemical deposition was improved with an additional deaeration step inside a desiccator with the
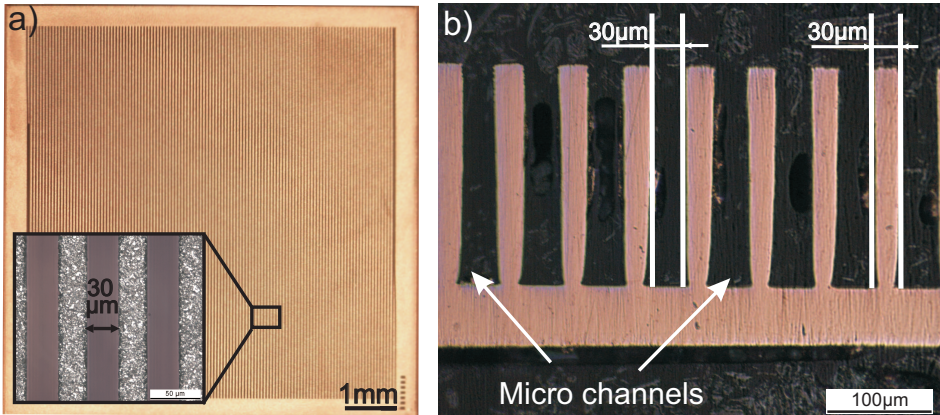
Figure 4.3: Optical microscopy pictures of a copper microchannel chip featuring 30 μm wide channels. a) Top view of entire chip, b) cross section view.

purpose of removing the remaining air bubbles inside the high aspect ratio features. Additionally, a reduced convection and consequently reduced ion supply inside the high aspect ratio pin-fin mold results in a slower growth rate than inside the long microchannels. Thus, the copper deposition is performed in two steps, with a wafer top surface grinding in between. This ensures a strong mechanical linkage between the pin-fins and the chip base during the overgrowth of the microchannels. In order to assure a total removal of the SU-8 mold during the wet chemical etch, the top 50 μm of the polymer are pre-etched by reactive-ion etching.

The fabricated microchannels with heat transfer enhancement structures are shown in Figure 4.4. A microchannel and fin width of 80 ± 5 μm and a channel height of 200 ± 10 μm were set as standard design parameters. Figure 4.4 a) shows the top view and 4.4 b) the side view of the pin-fin microstructures. Pin-fins with a diameter of 30 ± 4 μm and an average and maximal aspect ratio of 7 and 8.1 were achieved, respectively.
In Figure 4.4 c), the top views of the microchannels with sidewall protrusions are depicted. The protrusions are designed to have a width of 50 μm and a height of 30 μm. Samples with a varying microstructure pitch from one to four per unit-cell were fabricated (see Tab. B.4 in App. B for exact dimensions).
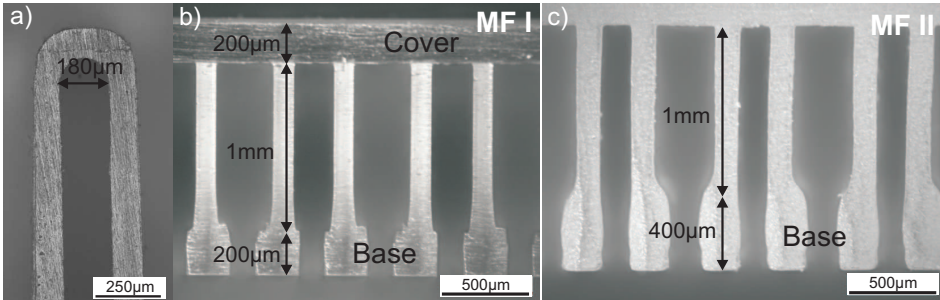
Manifold channel fabrication

The first generation of the manifold distribution channels are fabricated out of PMMA by micro milling. The dimensions are designed based on a parameter
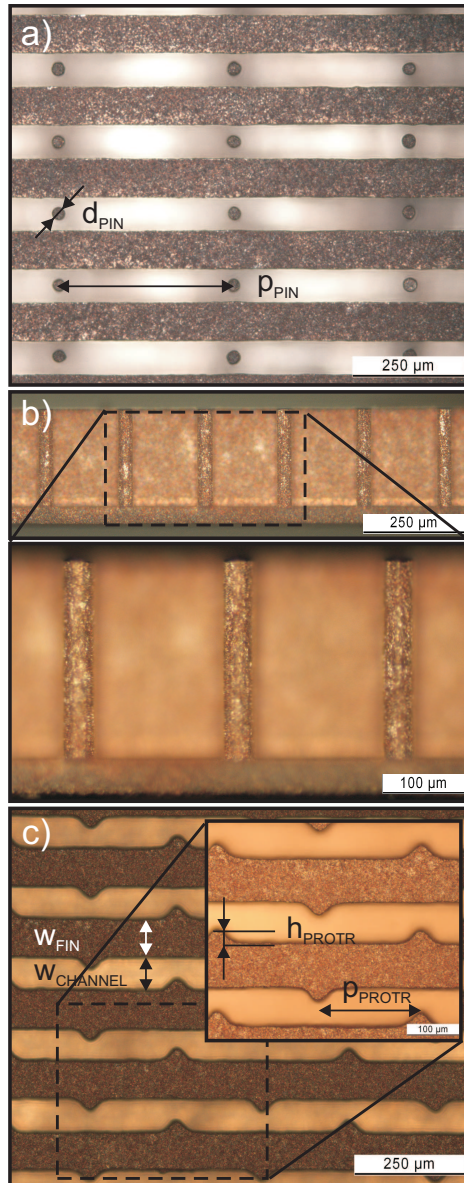
Figure 4.4: Microscope images of 80 µm copper microchannels with heat enhancement structures: a) top view and b) side view of pin-fin structures with a pin diameter of 30 µm, c) top view of channels with sidewall protrusions with a width of 50 µm and a height of 30 µm.

optimization study performed by means of the 1D model introduced in Section 3.3, with the aim to maximise net power output, while still complying with fabrication limits (see Tab. B.2 in App. B for the dimensions). The samples are closed by GBL solvent bonding of a 200 μm PMMA foil. Figure 4.5 a) shows the top view of a channel end and 4.5 b) the cross section view of the PMMA channels with the corresponding dimensions. Due the long processing times

Figure 4.5: Microscope images of manifold distribution channels a) top view and b) cross section view of PMMA channels fabricated by micro milling (MF I). c) Cross section view of epoxy based channels fabricated by microstereolithography (MF II, Accura Xtreme, Proform AG).

and high fabrication costs of the PMMA based structures, they are replaced in a second device generation by epoxy manifold channels (Accura Xtreme, $T_g = 335\,\text{K}$) fabricated by means of microstereolithography (Proform AG). No cover bonding step is needed, since the entire device can be produced in one run. The main differences to the PMMA samples are the thicker base and channel walls resulting in slightly higher pressure losses and thicker μHTSs.

The two different manifold channel designs will be labelled as MF I and MF II for the first and second generation, respectively. The first generation was used for the main small size TEHEX characterization in Section 5.1, while the second was applied for the μHTS design optimization study (Sec. 5.1.1) as well as for the double sided μHTS implemented in the double layer TEHEX (Sec. 5.1.3).

μHTS bonding

The assembly of the copper microchannels with the polymer manifold channels poses the challenge of bonding two structured surfaces of different materials. For the first generation manifold channels, a 10 μm thin double-sided adhesive tape is used as the bond material. Fist, the tape is laminated to the manifold and

the connecting slots at the bottom of the manifold structure are opened by micro laser milling (Fig. 4.1 f)). In a second step, the microchannel chip is mounted onto the manifold by means of an alignment structure (Fig. 4.1 g)).

For the second generation manifolds, a bonding process based on the transfer of a two component epoxy (EPO-TEK 301-2) is developed. Prior to bonding, the surface of the polymer is pre-treated by mechanical polishing and ultrasound cleaning in order to enhance the adhesion. The correlation of bonding strength and surface roughness is shown in Figure 4.6. The mixed epoxy is spin coated on a PMMA disc substrate to achieve an uniform thickness distribution. The manifold structure is pressed onto the thin adhesive layer in order to wet the bottom surface without covering the nozzle slots. Finally, the manifold is bonded to the copper microchannels by means of an alignment structure and cured at $60\,^\circ$C for 4 hours under an applied pressure of 25 ± 5 kPa.
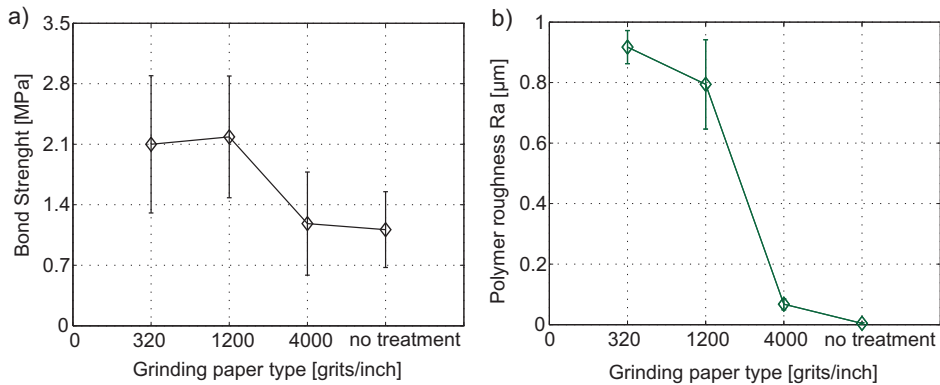
Figure 4.6: a) Epoxy (EPO-TEK 301-2) bond strength between polymer and copper and b) the corresponding polymer surface roughness as a function of the grinding paper grit. The bond strength was measured by a tensile pull-off test (Microtester$^{\text{TM}}$, Instron$^{\circledR}$)) conformable to DIN ISO 4624 (test setup used according to [154]). The error bars correspond to the standard deviation of three measured samples.

Figure 4.7 a) shows the microchannel top view with bonded epoxy adhesive stripes, after the manifold has been removed. A continuous film without clogging of the nozzle slots is achieved with the developed transfer process. In Figure 4.7 b), the cross section of a bond is shown, where the epoxy boundary is indicated by the white dotted line. Due to the bonding pressure applied during the curing, the epoxy partly enters the top of the microchannels. On one hand, this improves the bonding strength and prevents leaks other than through the microchannels. On the other hand, it also slightly reduces the heat transfer area
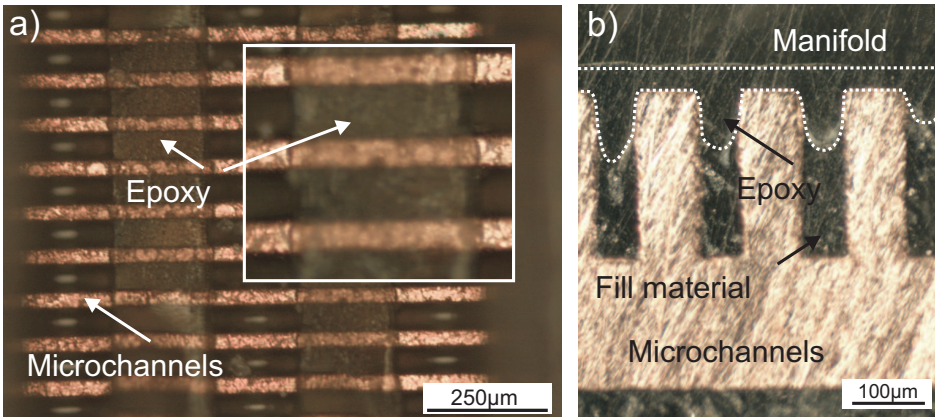
Figure 4.7: Microscope images of microchannel-manifold interface epoxy bond. a) Top view of the microchannels with remaining epoxy stripes after manifold removal and b) bond cross section with epoxy partly entering the microchannels.

and increases the pressure losses inside the microchannels.

TEHEX assembly

The geometric and thermoelectric properties of the μTEG used for the TEHEX measurements are found in Table B.5 in Appendix B. The generators are electrically passivated by spin coating 3 μm photoresist (Microposit S1813). To minimize the interface resistance between the μTEG and the μHTS, the passivated generator was additionally covered with a thin layer of silicone thermal compound (Dow Corning TC-5026) prior to assembly. Figure 4.8 shows a first generation μHTS mounted on a μTEG.

4.1.2 Large size micro heat transfer system

In the scaling up from the small 8 x 8 mm to a 9 x 9 cm μHTS, the same material combination for the two components is maintained, but the microchannel fabrication process is adapted.

Microchannel fabrication

For the fabrication of a large area microchannel layer, two approaches are evaluated: a bottom-up approach based on electroplating into a dry film resist mold and a top-down approach based on photolithography and wet etching. While the first approach has the advantage of producing higher aspect ratio channels, the second approach benefits from simple, fast and low-cost processing. Figure 4.9
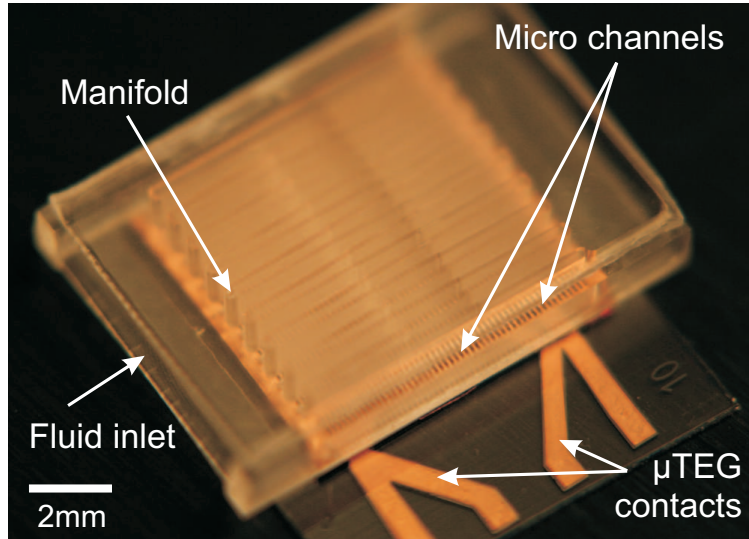
Figure 4.8: Picture of an assembled first generation μHTS/μTEG stack.

shows the two process flows of the microchannel fabrication.

In the bottom-up approach, a 300 μm thin 10 x 10 cm copper plate is used as a base substrate. Prior to resist lamination, the plate is ground (2400 grit sandpaper), shortly etched in copper etchant and cleaned in a 10 % hydrochloric acid (HCL) solution in order to remove the top copper layer and enhance adhesion. Three layers of the 75 μm thick dry film photoresist (Ordyl AM 175) are laminated (Walter Lemmer RLM 419p laminator) on top of each other (Fig. 4.9 a) 1)). Special attention must be paid not to trap air bubbles between the layers. After the photolithography process (Fig. 4.9 a) 2)), the substrate is cleaned with a 10 % HNO_3 solution in order to remove the native oxide and possible contaminants. The microchannels are grown in an acid copper bath (electrolyte AC-80 P, ERNE surface AG) optimized for trench filling at a current density of 1.4 A/dm^2(Fig. 4.9 a) 3)). The excess overgrown material is ground down (Fig. 4.9 a) 4)) and the dry film photoresist is removed with an 5 % Ordyl stripping solution. The final process parameters are found in Table A.2 in Appendix A.

The top-down approach starts with a 500 μm thin 10 x 10 cm copper plate which is pretreated same as the plate used in the bottom-up process. A layer of 30 μm thick dry film resist (Photec H-6230, Enthon) is laminated on both sides of the copper plate (Fig. 4.9 b) 1)). The back side photoresist is used as a protective
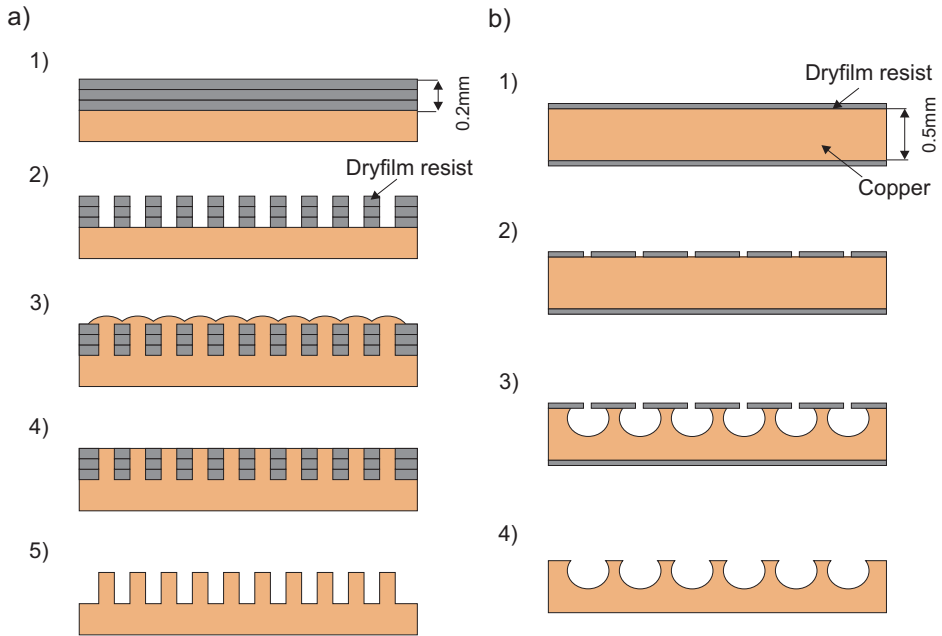
Figure 4.9: Fabrication process flows of the large area microchannels showing the two evaluated approaches: a) bottom-up approach based on electroplating into a dry film resist mold and b) top-down approach based on wet etching.

layer for the subsequent etching step. The channel slots are opened by photolithography (Fig. 4.9 b) 2)) and the plate is etched by spraying the etchant with a continuous rotation movement (Walter Lemmer S21). To ensure homogeneous etching over the large sample area, its position is turned by 90° every 2 minutes. The average measured etch rate is 15 µm/min (Fig. 4.9 b) 3)). In the last step, the photoresist is stripped (Fig. 4.9 b) 4)). The final process parameters can be found in Table A.3 in Appendix A.

Figure 4.10 a) shows a WLI image of microchannels fabricated by the top-down approach and Figure 4.10 b) the cross section view of etched microchannels. Table 4.1 summarizes the achieved aspect ratios for test samples and the final fabricated 9 x 9 cm microchannel plates. The test samples are the result of a feasibility study to investigate the limits of the fabrication technology. The final devices used for measurements are designed in a more conservative way in order to assure high yield. The advantages of the fabrication approach based on electroplating are the better process and dimension control as well as higher
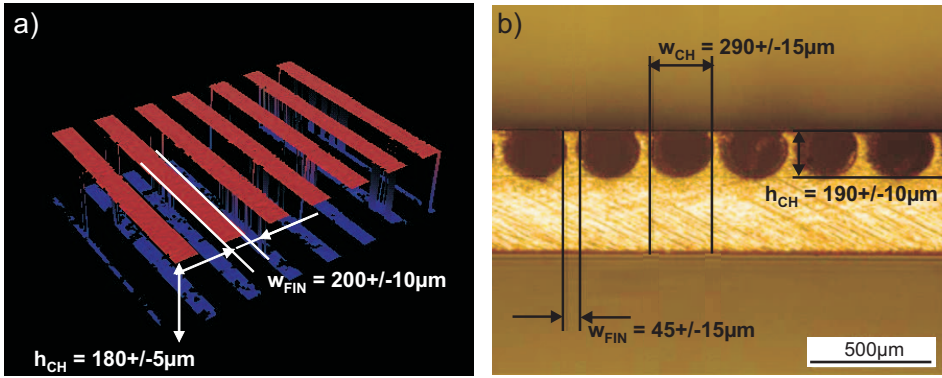
Figure 4.10: a) WLI image of microchannels fabricated by the top-down approach and b) cross section view of microchannels from the top-down fabrication process.

Table 4.1: Dimensions and aspect ratios of test samples and final microchannel plates for the two fabrication approaches.

	Electroplating Bottom-up		Etching Top-down	
	Test samples	Final MC	Test samples	Final MC
Channel width [μm]	140	200	290	220
Channel height [μm]	210	180	190	170
Channel aspect ratio	1.5	0.9	0.7	0.77
Fin aspect ratio	1.8	0.9	4.2	1.55
Fin to channel ratio	0.8	1	0.2	0.5

channel aspect ratios. However, the process flow is more complex and takes significantly longer to complete, compared to the etching based approach. An additional important advantage ot the top-down process is the lower fin to channel width ratio, resulting in smaller pressure losses due to wider microchannels.

An alternative approach for the fabrication of high aspect ratio microchannels would be the application of micro deformation technologies, e.g. as used in micro coolers offered by Wolverine Tube Inc.

Manifold fabrication

The large size manifold channels are fabricated by stereolithography (Proform AG) out of a temperature resistant epoxy (DSM 12120 HT, $T_g = 393$ K). The

optimal number of manifold channels is investigated by 1D simulations and the remaining dimensions are set to match the measurement setup and to comply with the fabrication constrains. The final design parameters can be found in Table B.6 in the Appendix B.

For potential future batch fabrication, the rapid prototyping method could be replaced by injection moulding.

In contrast to the small size µHTS, the large size microchannel plate is not bonded to the manifold channels. The clamping pressure applied in the measurement setup is sufficient for a leak tight operation.

TEHEX assembly

Two different types of large area TEGs are characterized in the scaled up TEHEX. Both samples consist of smaller generators connected electrically in series. The main difference between the applied modules is the total number of thermocouples inside the polymer matrix. The geometrical and TE parameters of both TEGs (labelled MTEG I and MTEG II) can be found in Table B.7 in Appendix B.

The TEGs used for measurements are passivated with a $10\,\mu m$ epoxy film. Nevertheless, electrical breakthroughs have occurred and an additional protection layer is needed. Therefore, the microchannel base is coated with Al_2O_3 deposited by e-beam evaporation and additionally covered by Benzocyclobutene (BCB) applied by spin coating. This double layer ensures a reliable protection during handling and operation combined with a low thermal interface resistance (see Tab. B.8 in App. B for estimated interface resistance values).

Thermal paste is used to reduce the contact resistance between the microchannel plate and the generator. In order to avoid water leakage, the edges of the µHTS/TEG/µHTS stack are sealed with silicone.

An assembled single layer TEHEX is shown in Figure 4.11.Its total weight is $114\,g$, of which the manifold channels account for $46\,g$ and the TEG/microchannel stack for $68\,g$.

4.2 Experimental

4.2.1 Small size thermoelectric heat exchanger

The characterization of the $8 \times 8\,mm$ thermoelectric heat exchanger was performed in different levels of complexity. The fixture assemblies of the four different test modules are schematically depicted in Figure 4.12. First, the thermal
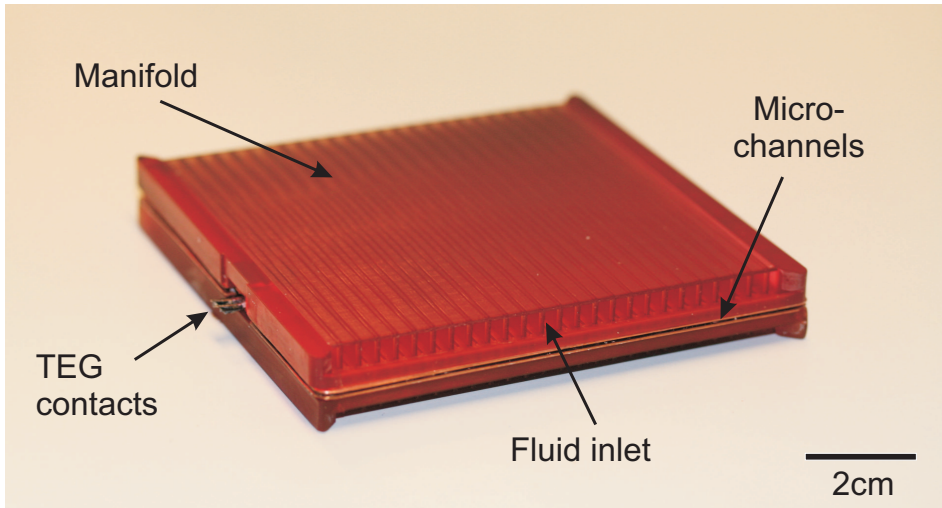
Figure 4.11: Assembled single unit of a large size TEHEX.

and hydrodynamic performance of the µHTS was analysed (Fig. 4.12 a)). Second, a µHTS/µTEG stack (Fig. 4.12 b)) and finally, a TEHEX with one (Fig. 4.12 c)) and two unit stacks (Fig. 4.12 d)) were characterized with respect to the thermoelectric net output power. The corresponding systems were mounted in a clamping fixture and connected to a controlled fluid loop measurement setup.

The µHTS and µHTS/µTEG stack are mounted on a temperature-controlled heat source, consisting of a resistive heater (platinum meander on Al_2O_3 substrate) and a BCB-bonded copper block for homogenous heat distribution. The Cu block temperature is controlled by means of an integrated thermocouple located at the center of the block. The side surface area of the Cu block exposed to ambient air is additionally isolated by polyimide in order to minimize thermal losses through convection. For an improved thermal interface between the Cu block and the µHTS or µTEG, a thermal paste is used and a constant clamping pressure of 660 ± 30 kPa applied. The heat flux through the device is assumed to be equivalent to the necessary heating power of the resistive heater to hold a specific steady state condition (convective thermal losses are neglected). The heat transfer resistance is calculated from the measured heat flux and the applied temperature difference ΔT_0. The µHTSs are connected to the fluid loop by a flexible tube at the manifold fluid inlet and outlet. Figure 4.13 shows the schematics of the cold and hot fluid loop measurement setup for the TEHEX characterization. Only the cold loop was needed for the µHTS and µHTS/µTEG stack characterization.
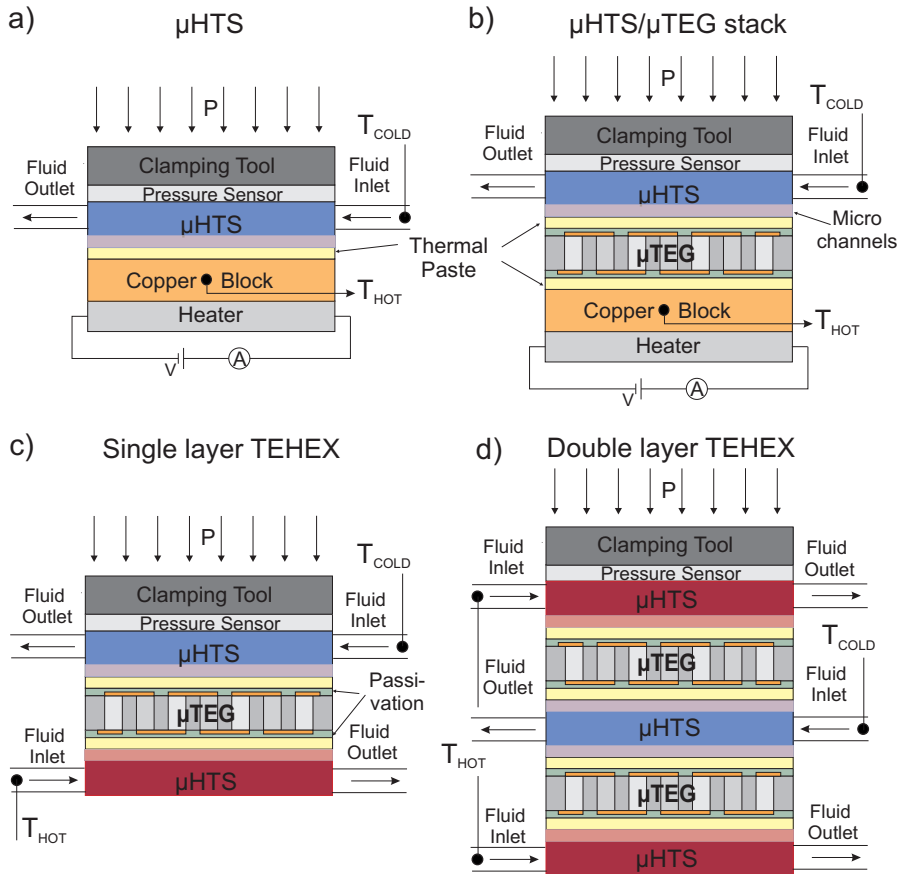
Figure 4.12: Measurement fixtures of a) a µHTS b) a µHTS/µTEG stack and c) a single layer and d) double layer TEHEX test module.

The hot and cold water (deionized) flow is controlled by means of two flow meters (error cold: $\pm 1\%$ of reading, error hot: $\pm 2\,\text{ml/min}$) and gear pumps. The pressure drop over the µHTSs is measured with differential pressure sensors (error cold: $\pm 0.13\,\text{mbar}$, error hot: $\pm 1\,\text{mbar}$). The cold water inlet temperature is kept at $293 \pm 0.1\,\text{K}$. For the µHTS/µTEG and TEHEX system characterization, the thermoelectric power output is calculated from the measured open circuit voltage of the µTEG under electrically matched loads and therefore corresponds to the maximal achievable power output.

The control of the measurement setup and the data acquisition is performed
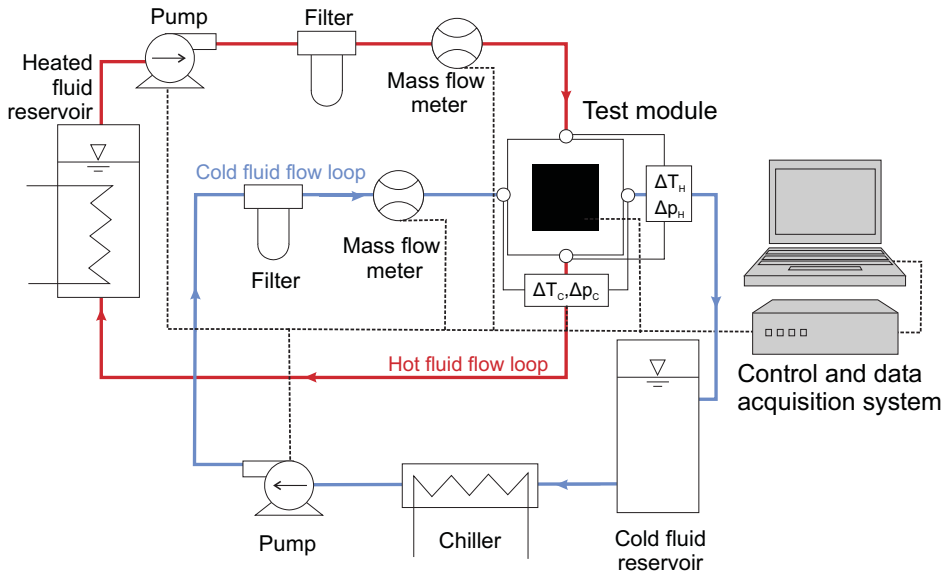
Figure 4.13: Schematic view of the cold and hot fluid loop measurement setup.

by a LabVIEW program, Keithley sourcemeters (Keithley 2400) and a data acquisition board (NI 6259). A measurement duration of 120 s and a sampling frequency of 0.76 s^{-}1 are defined as standard acquisition conditions for one data point under steady state.

The measurement uncertainty was calculated according to ISO/IEC 17025 standards [155]. The resulting standard deviation from the time averaged measurement signals (random error) was combined with measurement equipment errors (systematic errors). The Gauss propagation of uncertainty was used for error calculations of indirectly measured values. The measurement repeatability of the clamping structure was tested by multiple mountings of the same μHTSs and μHTS/μTEG devices. The maximum measured standard deviation errors were below 5.3 % and 0.52 % for the measured heat transfer resistance K_{HTS} and open circuit voltage V_{oc}, respectively. This measured standard deviations of the clamping influence are all below the calculated measurement uncertainty plotted as error bars in the figures.

4.2.2 Large size thermoelectric heat exchanger

The measurement setup for the large size thermoelectric heat exchanger is provided by greenTEG. Figure 4.14 shows the clamping fixture for a single unit
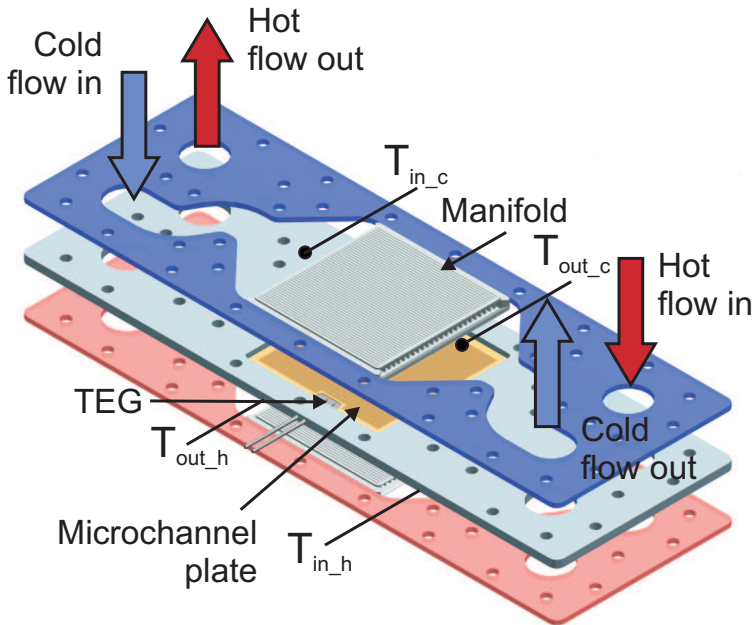
Figure 4.14: Clamping fixture of the large size thermoelectric heat exchanger.

layer TEHEX.

The temperature of the cold and hot fluid flow is measured directly at the inlet and outlet of the manifold channels. The volumetric flow rates and the pressure losses are recorded with an accuracy of $\pm 0.76\,\mathrm{l/min}$ and $\pm 60\,\mathrm{mbar}$, respectively. In order to extract the pressure losses directly over the µHTS, the measurement setup is characterized without the inserted TEHEX and calibrated correspondingly.

4.3 Conclusions

The fabrication technology of the small size µHTS is based on copper electroplating into a SU-8 mould for the microchannels and on micro milling or micro stereolithography for the manifold distribution channels. The key fabrication challenges include the fabrication of stress free high aspect ratio moulds as well as the development of a reliable bonding technique for the joining of copper microchannels and manifold channels. Microchannel widths and pin-fin structures with dimensions down to 30 µm and aspect ratios up to 7 and 8.1 are achieved, respectively.

For the scaled up device, two fabrication approaches are evaluated and compared: a bottom-up approach similar to the small size fabrication process based on electroplating and a top-down approach based on photolithography and etching. With the first approach, higher aspect ratio channels are feasible, while the second method benefits from fast and simple processing as well as low fin to channel ratios and is thus selected for device implementation.

The assembled small and large size devices are mounted in corresponding clamping structures and characterized in controlled fluid loop measurement setups.

5 Device Characterisation

Many different sets of parameters influence the performance of the thermoelectric heat exchanger; namely the dimensions of the μHTS itself, the properties and dimensions of the thermoelectric generator as well as the applied boundary or working conditions.

The 8 x 8 mm systems are used to investigate and understand the different parameter dependencies with the aim of optimizing the overall system's net output performance. The goal of the large 9 x 9 cm TEHEX is to show the feasibility of the device upscaling and to demonstrate its potential for large scale low temperature waste heat recovery.

5.1 Small size thermoelectric heat exchanger

[1]This section focuses on the investigation and characterization of the most important TEHEX system parameters. For this purpose, the complex system is divided into individual subsystems. In the first part, the μHTS itself is characterized with respect to the system's dimensions, flow rates and applied temperature gradients. In the second part, the output performance of the μHTS/μTEG systems is analysed with regard to the microchannel dimensions of the μHTS, boundary conditions, μTEG thermal resistance and thermoelectric properties. In the last section, a complete TEHEX consisting of one and two unit cells is studied. The advantages of variable thermal resistances are discussed and practical aspects of thermal resistance matching are evaluated.

5.1.1 Micro heat transfer system

Figure 5.1 shows the measured and computed thermal and hydrodynamic performance of μHTSs with different microchannel widths relative to the fluid flow rate. Figure 5.1 a) depicts the removed heat flux and Figure 5.1 b) shows the corresponding heat transfer resistance K_{HTS}. The heat flux increases strongly with increasing flow rates, mainly due to the corresponding rise in the heat capacity rate of the fluid. However, towards higher flow rates, the influence of the increasing mass flow on the heat flux is limited by the convective heat transfer. With decreasing channel widths, the heat flux is enhanced mainly due

---
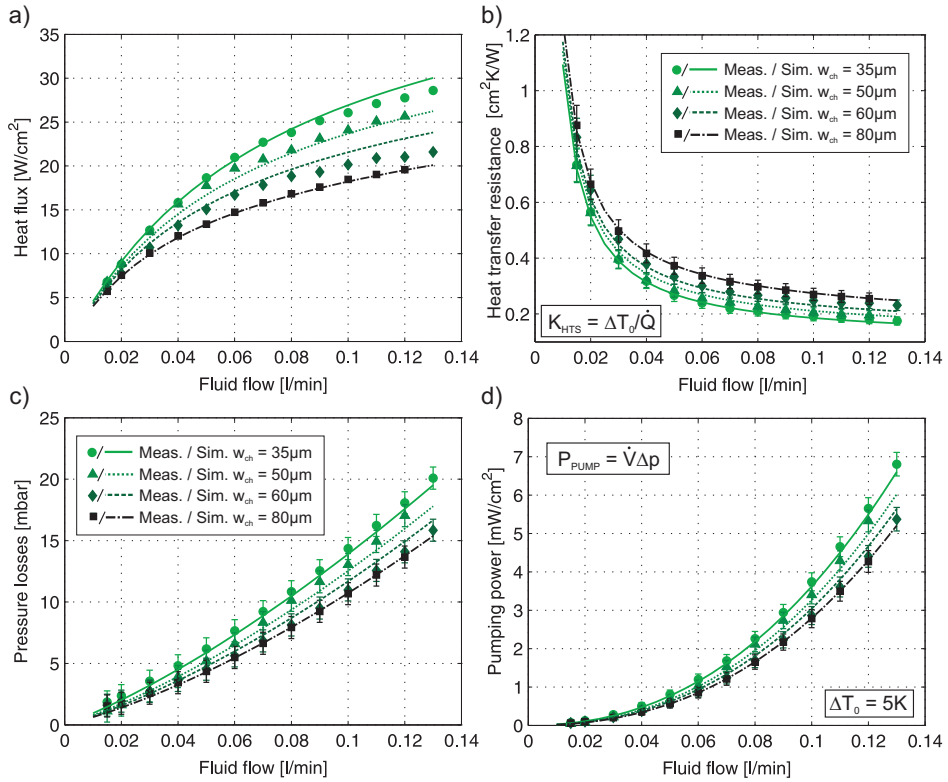
Figure 5.1: Measured (markers) and computed (lines) performance of µHTSs with different microchannel widths as a function of the fluid flow rate at an applied ΔT_0 of 5 K. a) Heat flux, b) heat transfer resistance K_{HTS}, c) pressure losses and d) pumping power. The µHTS parameters used for measurements and simulations are found in Tab. B.2 in App. B (MF I).

to an increase in the convective heat transfer. At smaller microchannel widths, the thermal boundary layer is thinner and therefore the heat convection inside the channel is improved. Additionally, the effective heat transfer area per chip is increased. The heat transfer resistance K_{HTS} resulting from the measured heat flux and applied ΔT_0 is shown in Figure 5.1 b). In agreement with the heat flux, K_{HTS} decreases with increasing fluid flow due to an increase in the heat capacity rate of the fluid. With the smallest channel size of 35 µm, a minimal heat transfer resistance of 0.175 cm²K/W could be reached at a fluid flow of 0.13 l/min. The measured K_{HTS} also includes the interface resistance of the thermal paste located between the µHTS and the heater. The resistance corresponding to a thermal paste layer thickness of approximately 25 µm is estimated to be 0.07 cm²K/W.

The pressure losses and the corresponding power necessary to pump the fluid through the μHTS are plotted in Figure 5.1 c) and d), respectively. The pressure losses increase with larger fluid flows as well as with smaller microchannel dimensions. The former is a result of an increased hydrodynamic resistance due to the increased flow velocity. The latter can be explained by larger shear forces induced by an increased surface area to volume ratio.

The experimental results are in good agreement with the simulation results. The measured thermal properties (Fig. 5.1 a) and b)) show minor deviations with respect to the computed values. These deviations can be attributed to slight variations of the thermal paste layer thickness, since the exact thickness is hard to control. The deviations of the pressure losses and pumping power from the computed values (Fig. 5.1 c) and d)) can be explained by the limited fabrication accuracy of the device. Especially the connecting slots between the top manifold layer and bottom microchannels are likely sources of geometric variations, due to the bonding and slot release processes (see Sec. 4.1.1 MF I).

In order to quantify the influence of the boundary conditions on the thermal and hydrodynamic properties of the μHTS, the fluid inlet temperature and the heater temperature were varied as well. By increasing the fluid temperature, an improvement of the overall system performance was observed. As a result of an inlet temperature increase of 2 K ($T_{in} = 295$ K), the K_{HTS} measured at a fluid flow of 0.04 l/min decreases by 6 % and the pumping power by 7 % (averaged over 3 different samples). The reduction in K_{HTS} originates from the increase of the thermal conductivity of the fluid, resulting in an increased thermal convection at the microchannel walls and thus reduced convective resistance. The higher inlet temperatures of the fluid also reduce the mean fluid density and mean fluid kinetic viscosity. This decreases the hydrodynamic resistance, leading to a smaller pressure drop and consequently smaller pumping powers. The same trend is observed when the heater temperature is increased. However, the effect is less pronounced, since the fluid is heated up indirectly. In this case, an average improvement of 1 % of the heat transfer resistance and 6 % of P_p was measured for a heater temperature increase by 10 K ($T_{hot} = 308$ K) and a fluid flow of 0.04 l/min (averaged over 3 different samples). The measurement results demonstrate an improved thermal and hydrodynamic μHTS performance at higher operation temperatures. However, the influence on the μHTS parameters is rather small in the limited ranges of the investigated temperatures. Additionally, due to the measurement uncertainties, the given changes should be regarded as qualitative trends.

µHTS design optimization

[1]As the 3D FEM simulations of the microchannel unit cell have shown in Section 3.2.4, microchannels with integrated microstructures and an optimized flow path can enhance the thermal and hydrodynamic performance of the µHTS. In order to validate the simulations, µHTSs featuring microchannels with different microstructures and spacings as well as manifolds with rounded nozzles are characterized.

In Figure 5.2, the measured heat transfer resistance K_{HTS} is plotted with respect to the corresponding pressure losses for four different µHTSs. The fluid flow rate is swept between 0.02 and 0.12 l/min in steps of 0.02 l/min. Table 5.1 additionally summarizes the performance of all measured devices relative to the unstructured reference sample at a fixed fluid flow rate of 0.1 l/min.

Table 5.1: Relative µHTS performance with respect to the unstructured sample measured at a flow rate of 0.1 l/min.

Sampel Type	Microstr. Pitch [µm]	ΔK_{HTS} [%]	Δp [%]
Pin-fins	390	-17	19
Pin-fins	195	-22	32
Pin-fins	130	-21	38
Protrusions	390	-5	3
Protrusions	195	-8	16
Protrusions	97.5	-12	34
Pin-fins+nozzle	390	-18	-8

Both results confirm the trends showed in the simulations. All measured devices result in a reduction of the heat transfer resistance, represented by a downwards shift of the coloured lines compared to the black line. The simultaneous increase in pressure losses (shift to the left side) caused by the introduced microstructures could be effectively counterbalanced by the rounded manifold inlet/outlet nozzles (dashed dark red line).

The slight increase in K_{HTS} of the measured samples compared to the simulation data (see Fig. 3.16) can be attributed to the thermal paste between the µHTS and the copper block (see Fig. 4.12 b)) that introduces an additional thermal interface resistance (estimated to be 0.07 ± 0.02 cm^{2}K/W corresponding to a thermal paste thickness of 25 ± 5 µm). Furthermore, the effective microchannel dimensions, in particular the microchannel height, might slightly vary from the values

---

[1] The major part of the µHTS design optimization content was published in the proceedings of Transducers 2013 [151] and was reproduced with permission. Copyright © 2013 IEEE.
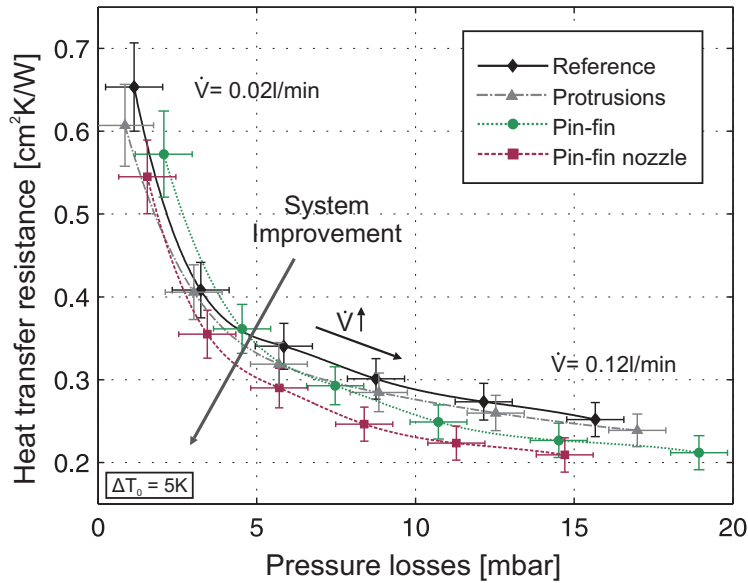
Figure 5.2: Measured heat transfer resistance K_{HTS} and corresponding pressure losses of different µHTSs as a function of the fluid flow rate at and applied $\Delta T_0 = 5\,K$. The µHTS parameters used for the measurements are found in Tab. B.4 (microchannels) and in Tab. B.2 (MF II) in App. B. Copyright © 2013 IEEE.

used in the simulations. This is mainly due the change in the bonding process (Sec. 4.1.1) and possible variations of the channel height related to fabrication tolerances. The increase in pressure losses of the measured µHTSs compared to the computed unit cell results from the additional pressure drop inside the manifold distribution channels (not modelled in the 3D-FEM simulations) as well as a larger nozzle height and reduced effective channel heights. The deviations in manifold dimension and corresponding boding process (MF II instead of MF I) is also a reason for a pressure loss increase compared to the µHTSs characterized in the section above (Fig. 5.1). Additionally, potential influences from microscale effects, such as an increased surface roughness introduced by the copper etching step, must also be kept in mind (see Sec. 3.2.1).

5.1.2 µHTS/µTEG system

In order to evaluate the optimal µHTS/µTEG system performance, the influence of the working conditions, the microchannel widths, the µTEG thickness and TE properties were investigated.

69

Influence of working conditions

Figure 5.3 a) shows the measured Seebeck voltage and the output power of the µHTS/µTEG system with respect to the applied temperature gradient and different fluid flow rates. In Figure 5.3 b), the corresponding net output power is depicted. The slope of the Seebeck voltage (solid line) increases with increasing flow rates, i.e. decreasing heat transfer resistance K_{HTS}, due to an increased
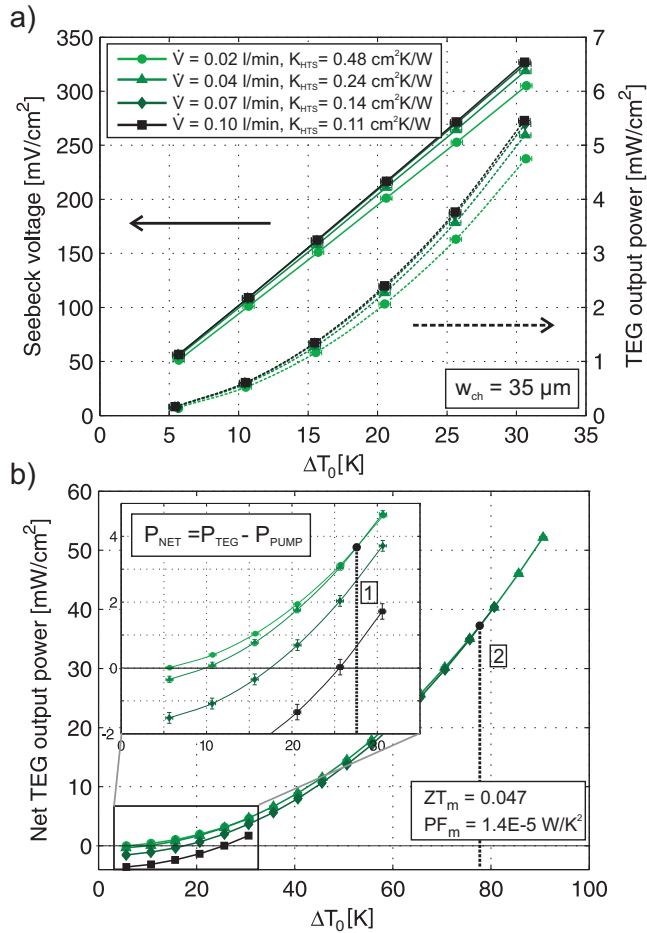
Figure 5.3: a) Seebeck voltage (solid lines) and output power (dashed lines) measurements of the µHTS/µTEG system and b) net output power as a function of the applied ΔT_0 and the fluid flow rate for $w_{ch} = 35\,\mu m$. The µTEG (STEG I) and µHTS (MF I) parameters used for measurements and simulations are found in Tab. B.5 and Tab. B.2 in App. B, respectively.

heat flux and therefore larger actual temperature gradient across the generator. However, the differences in the slopes are relatively small. This is due to a large µTEG thermal resistance of $5.1\,\mathrm{cm^2K/W}$ compared to the K_{HTS} variations of $\Delta K_{HTS} = 0.37\,\mathrm{cm^2K/W}$, thus resulting in a small influence of the overall heat transfer. Correspondingly, the differences in the µTEG output power (dashed lines) show only small deviations between different flow rates. The specific influence of the K_{TEG} to K_{HTS} ratio and the associated thermal matching will be discussed in more detail in Section 5.1.2.

If the consumed pumping power is subtracted from the output power (Fig. 5.3 b)), the influence of the flow rates increases significantly. Larger flows, consuming higher pumping powers, need higher temperature gradients to achieve a positive net output power. However, their slopes are steeper and therefore, at larger applied ΔT_0, higher flow rates outperform lower ones. The transition points for this system are marked in the graph by vertical dashed lines (point 1 and 2). This means that the system performance can be adapted to different operating conditions by varying the fluid flow rate. For operating conditions with small temperature gradients, small flow rates, i.e. large heat transfer resistances and small pumping powers, are advantageous. With increasing temperature gradients, the flow must be increased in order to track the maximal net output power of the system.

Influence of microchannel dimensions

As discussed in Section 5.1.1, a decrease in the microchannel width reduces the heat transfer resistance and increases the consumed pumping power of the µHTS.

The influence of the microchannel dimensions on the Seebeck voltage and the net output power of the generator is plotted for different flow rates in Figure 5.4. A reduction in channel width directly leads to an enhancement of the actual temperature gradient across the µTEG and therefore an increase in the µTEG's performance. However, in the investigated dimension range, the impact of a reduced microchannel width on the Seebeck voltage (and output power) is smaller than the influence of the fluid flow rate. This can be explained with the smaller difference in the heat transfer resistance K_{HTS}, also illustrated in Figure 5.1 b).

When the net µTEG output power is considered (Fig. 5.4 b)), the positive effect of smaller microchannel width is counterbalanced by the simultaneous increase in required pumping power P_p. Therefore, at higher fluid flow rates, where higher pumping powers are needed (e.g. black lines at $\dot{V} = 0.1\,\mathrm{l/min}$), P_p out-
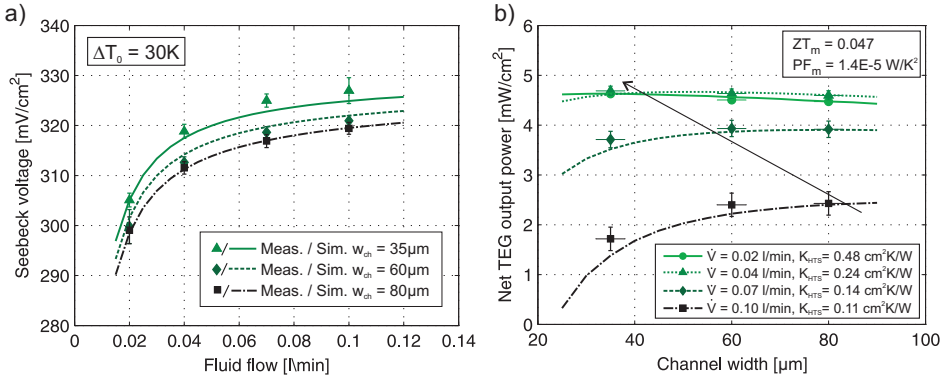
Figure 5.4: a) Measured (markers) and computed (lines) Seebeck voltage of the µHTS/µTEG system for different microchannel widths versus the fluid flow rate. b) Measured and computed net output power as a function of the microchannel width for different fluid flow rates at a ΔT_0 of 30 K. The µTEG (STEG I) and µHTS (MF I) parameters used for measurements and simulations are found in Tab. B.5 and Tab. B.2 in App. B, respectively.

weighs the reduced K_{HTS} for small microchannel widths, and larger channel widths yield better net power results. With decreasing flow rates the optimal channel width shifts towards smaller microchannel dimensions. At $\Delta T_0 = 30$ K, a fluid flow of 0.04 l/min and a channel width of 50 µm results in the maximal net output power. Considering the decreasing relative influence of the pumping power for increasing temperature differences applied, the impact of a reduced K_{HTS} will be more pronounced at higher ΔT_0. According to simulations, at an applied temperature gradient of 90 K, the maximal net power output is reached for this system with a channel width of 35 µm, at a volumetric flow rate of 0.06 l/min. Therefore, by knowing the steady state operating conditions of the system, a custom microchannel design can be applied to achieve an optimal output performance.

Influence of µTEG thermal resistance

As shown in Figure 5.3 a), the influence of the varying heat transfer resistances, i.e. varying fluid flow, on the µTEG output power is small. This can be attributed to the fact that the thermal resistance of the µTEG is significantly larger than the variation in the heat transfer resistance of the µHTS for this specific set-up. To investigate the effect of smaller differences in thermal resistance, the µTEG thickness is reduced in two consecutive steps. The measurement results and corresponding simulations are summarized in Figure 5.5. The Seebeck voltage decreases with
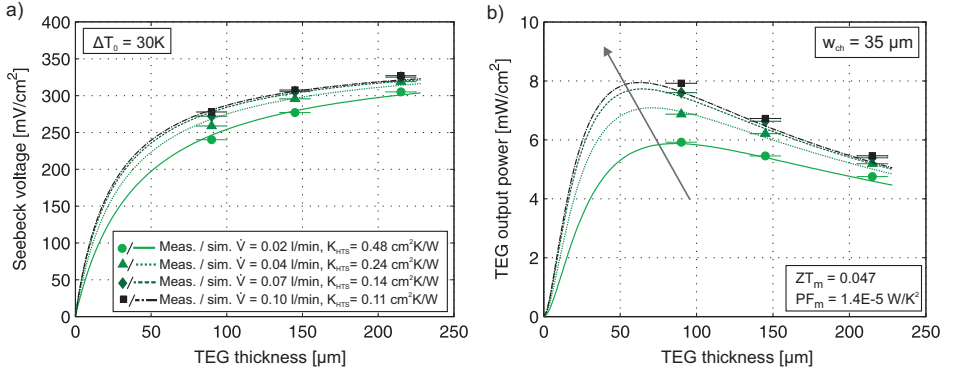
Figure 5.5: Measured (markers) and computed (lines) a) Seebeck voltage and b) output power of the µHTS/µTEG system as a function of the µTEG thickness at an applied ΔT_0 of 30 K and a $w_{ch} = 35$ µm. The µTEG thermal resistances are $K_{TEG}(90\,\mu m) = 2.1\,cm^2K/W$, $K_{TEG}(145\,\mu m) = 3.4 cm^2K/W$ and $K_{TEG}(215\,\mu m) = 5.1\,cm^2K/W$. The total contact resistance K_{con} lies between $0.55\,cm^2K/W\,(0.1l/min)$ - $0.92\,cm^2K/W\,(0.02l/min)$. The µTEG (STEG I) and µHTS (MF I) parameters used for measurements and simulations are found in Tab. B.5 and Tab. B.2 in App. B, respectively.

decreasing µTEG thickness as well as with reduced flow rates (Fig. 5.5 a)). This is a direct consequence of the reduced temperature gradient across the generator. Under constant heat flux assumptions, the Seebeck voltage of a generator can be expressed in a simplified model by inserting Eq. 3.18 in Eq. 3.8

$$V_{oc} = m\,\alpha\,\frac{K_{TEG}}{K_{TEG} + K_{con}}\Delta T_0 \tag{5.1}$$

where K_{con} is defined as the sum of all thermal contact resistances, including the heat transfer resistance of the µHTS K_{HTS} and the interface resistances $K_{interface}$ at both sides of the TEG (electrical passivation and thermal paste, see Fig. 4.12 b)). Each $K_{interface}$ is estimated to be approximately $0.22\,cm^2K/W$, resulting in a total contact resistance K_{con} between $0.55\,cm^2K/W\,(0.1l/min)$ and $0.92\,cm^2K/W$ $(0.02l/min)$. At a µTEG thickness below 50 µm, the slope of the Seebeck voltage is very steep, since the µTEG thermal resistance is smaller than the total contact resistance ($K_{TEG} < K_{con}$). Therefore, a small increase in the µTEG thickness results in a relative large increase in ΔT_{TEG}. With increasing thicknesses ($K_{TEG} > K_{con}$), the curve becomes progressively flat due to the reduced influence of the µTEG thickness on ΔT_{TEG}. At the same time, the influence of varying K_{HTS} becomes smaller with increasing µTEG thickness, which is indicated by the smaller spreading of the Seebeck voltage measurements for the different fluid flows.

This effect is more pronounced for the µTEG output power (Fig. 5.5 b)), where the Seebeck voltage is squared (see Eq. 3.19). The µTEG output power also increases with increasing µTEG thickness, it reaches a maximum and decreases again. In the first section, the power increase is again attributed to the increase of ΔT_{TEG}. At the maximum point, the thermal resistances of the µTEG and the sum of the contacts are approximately matched (see Sec. 3.1.4). On the right side of the maxima, the negative influence of the increased electrical resistance of the generator dominates over the increase in the Seebeck voltage. With an increased applied fluid flow, i.e. reduced K_{HTS}, the point of maximal output power shifts towards higher values and smaller µTEG thicknesses. A reduced heat transfer resistance results in higher ΔT_{TEG} and smaller µTEG thicknesses to achieve thermally matched resistances (see Sec. 3.1.5).

For each temperature operating point of the system, an optimal µTEG thickness can be defined to maximize the power output. For applications with lower ΔT_0 available, where smaller fluid flows can be applied to reach the maximum net output power, the optimal µTEG thickness is around 90 µm. With increasing external temperature gradient and therefore increasing required fluid flows for optimal power exploitation, the µTEG thickness can be reduced even further. The presented optimal µTEG thicknesses are specific values for the µTEG used in this study. Changes in thermal and electrical properties of the generator will result in a shift of the maximal power points to different µTEG thicknesses.

Small thicknesses enabled by the very low heat transfer resistance of the µHTS are of particular interest for waste heat recovery. For example in industrial heat exchanger systems, where high heat fluxes are required to sustain the necessary heat dissipation, a low thermal resistance of the generator is favourable. Additionally, a reduced µTEG thickness brings the advantages of smaller material and fabrication costs, as well reductions in system size and weight.

Influence of µTEG thermoelectric properties

In order to investigate the influence of the generator's TE properties on the performance of the µHTS/µTEG system, different TEGs were mounded in the measurement setup and compared to each other. In addition to the above applied STEG I, two other generators provided by greenTEG and two commercial available modules (Laird Technology, Nextreme) are integrated and characterized. The µTEG TE and geometric specifications can be found in Table B.5 in Appendix B. Figure 5.6 shows the net output power per active µHTS area for the different µTEGs as a function of the applied temperature gradient. The STEG II/III originate from a different fabrication generation than STEG I, where
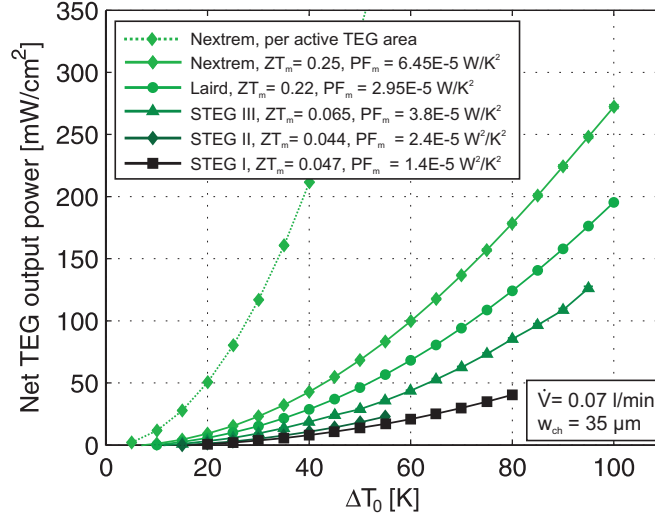
Figure 5.6: Measured net output power of μTEG/μHTS with different TE modules as a function of the applied ΔT_0 at a fluid flow rate of 0.07 l/min and $w_{ch} = 35\,\mu m$.

the thermoelectric material properties, the matrix material and the contacting process have changed.

Although having a slightly smaller module $Z\overline{T}_m$, mainly due to the significantly reduced TEG thermal resistance K_{TEG}, STEG II outperforms STEG I. The STEG II performance improvement can be attributed to the higher module power factor PF_m, in particular the reduced electrical resistance. This confirms the conclusions drawn in Section 3.1.5, where the reduced impact of the material thermal conductivity on the output performance of TEG systems with small thermal coupling resistances is shown. The increase in net output power of the STEG III compared to STEG II is a result of an enhanced Seebeck voltage and thus higher PF_m.

The commercially available Laird TEG (OT20) is a standard Pelier module with a total thickness of 2.18 mm and therefore significantly higher thermal resistance than the remaining TEGs (approx. 6.7 x higher than STEG III). Therefore, the net output increase compared to the STEGs can be accredited to the much higher $Z\overline{T}_m$ mainly due to the very large K_{TEG}, as well as to a slightly larger TEG footprint.

The thermoelectric generator provided by Nextreme (HV56) is based on supper-

lattice thin film materials [24] and is optimized to provide power for high heat flux applications ($> 20\,\mathrm{W/cm^2}$). The company claims to have the highest output power density. With the largest $Z\overline{T}_m$ and PF_m it is the best performing device within the investigated modules. It is important to note that the total footprint of the Nextreme generator is 4.8 x smaller than the one of the STEGs. If the net output power is calculated per active µTEG area instead of per active µHTS area, the power is further increased as shown by the dotted line in the plot (funnelling effects are neglected).

The impact of all TE and geometric parameters on the net output power of the large size TEHEX will be systematically discussed in Section 6.1.

5.1.3 Thermoelectric heat exchanger

[1]In the final investigation of the small $8 \times 8\,\mathrm{mm}$ system, the entire TEHEX is assembled in a single and double layer thermoelectric unit stack and characterized with respect to the applied thermal gradients and fluid flow rates.

Figure 5.7 shows the measured (markers) and computed (lines) µTEG output performance for a single layer thermoelectric heat exchange system. In Figure 5.7 a), the µTEG output power is plotted as a function of the varying cold and hot fluid flow rates for an applied ΔT_0 of 30 K. Analogous to the above discussed µHTS/µTEG system, the total output power increases with increasing flow due to a reduction of the heat transfer resistance K_{HTS}. When the pumping power is subtracted, an optimal flow rate can be found (Fig. 5.7 b)). In Figure 5.7 c), the Seebeck voltage and in d), the net output power are plotted with respect to the flow rates for fluid inlet temperatures differences between 10 K and 60 K. Unlike in Figure 5.3, the effect of the fluid flow rates on the Seebeck voltage is more pronounced. This originates form two main facts: First, the µHTS is used for heat supply and dissipation at both sides of the TEG. Therefore, the fluid flow has a double impact compared to the one-sided system before. Second, the applied µTEG has a smaller thermal resistance K_{TEG} and thus the relative influence of the µHTS is enhanced (see Fig. 5.5). At the lowest applied ΔT_0 of 10 K, no positive net power can be reached with this system, since the pumping power outweighs the µTEG output (Fig. 5.7 d)). Thus, there is a critical minimal temperature difference, where the TEHEX can be applied in order to produce a net gain. With increasing ΔT_0, the power gain and the optimal flow rate are increasing.

---

[1] The main content of this section was published in [157] and was reproduced with kind permission from Springer Science and Business Media.
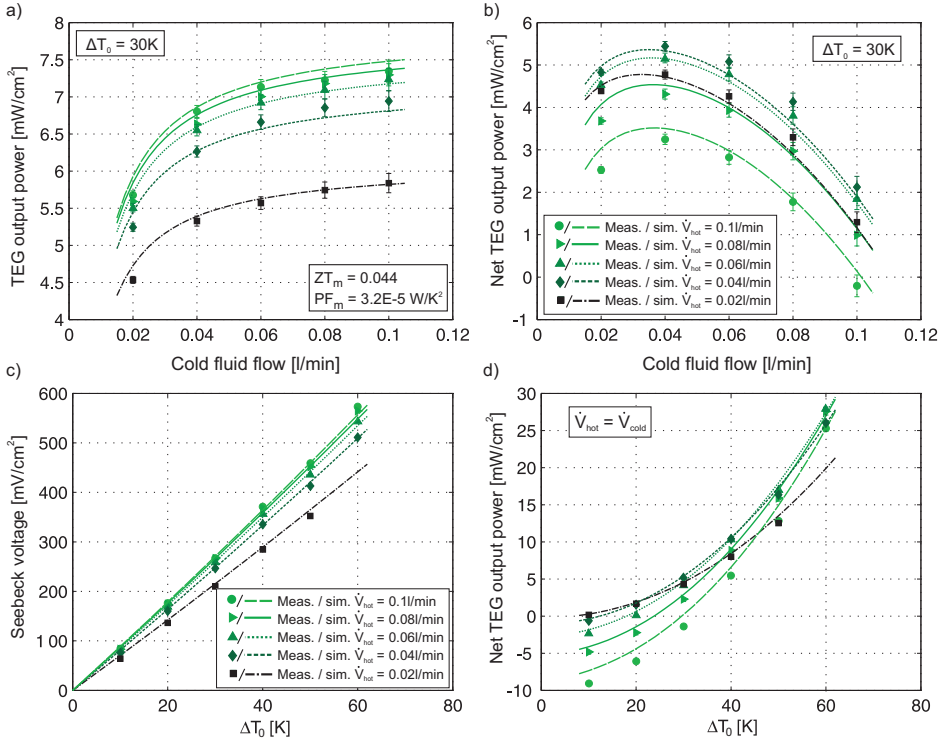
Figure 5.7: Measurements (markers) and simulations (lines) of a single layer small thermoelectric heat exchange system. a) Total and b) net output power at different hot and cold fluid flow rates for a fluid inlet temperature difference of $\Delta T_0 = 30\,\mathrm{K}$. c) Seebeck voltage and d) net output power for different ΔT_0 and different fluid flow rates, where the hot and cold flow rates are equal. The µHTS and µTEG parameters used for the experimental measurements and corresponding simulations can be found in Tab. B.5 (STEG IV) and Tab. B.2 (MF I with $w_{ch} = 45\,\mu\mathrm{m}$) in App. B.

Figure 5.8 shows the total and net output power of a double layer system in dependence of the applied fluid inlet temperature difference for different fluid flow rates. The power output was approximately doubled compared to a single layer system. The slight differences in the performance result from not identical system parameters, since different TEGs and double sided heat transfer systems are used. The reduced manifold channel height in a double sided µHTS (limited by the fabrication process) caused a significant increase in pumping power, showing its biggest impact at low temperatures and high flow rates. On the other hand, the improved net power at higher temperatures is a result of the higher Seebeck coefficient of the µTEGs used.
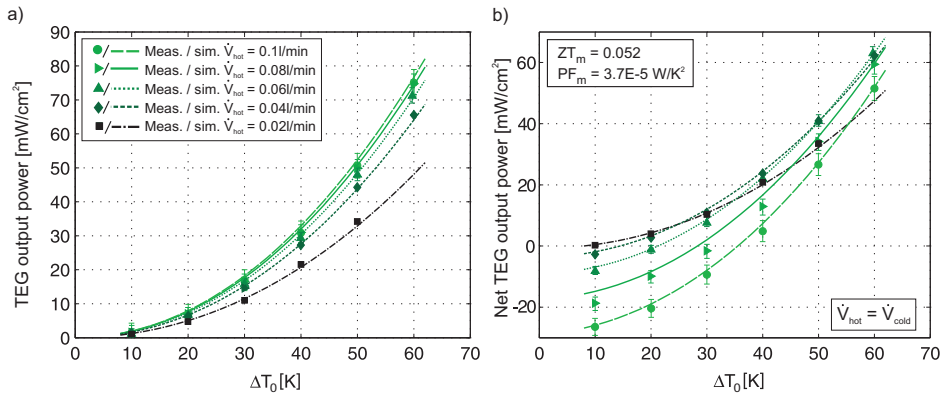
Figure 5.8: Measurements (markers) and simulations (lines) of a small double layer TEHEX. a) Total and b) net output power for different fluid flow rates with respect to the applied ΔT_0. The µHTS and µTEG parameters used for the experimental measurements and corresponding simulations can be found in Tab. B.5 (STEG V) and Tab. B.2 (MF I and MF II for the double sided µHTS with $w_{ch} = 45\,\mu m$) in App. B.

The measurement results are in good agreement with the computed values. The present deviations might be attributed to inaccuracies in dimensions and properties of the µHTSs and µTEGs, potential changes in $K_{interface}$ and a possible increased error of the fluid flow measurements caused by the operation outside the specified temperature range (for $\Delta T_0 = 60\,K$ only).

5.2 Large size thermoelectric heat exchanger

Two different types of large area TEGs with a different ratio of active thermoelectric area (see Tab. B.7 in App. B) are characterized in the scaled up thermoelectric heat exchanger unit (see Sec. 4.2.2 for experimental settings).

Figure 5.9 shows the output characteristic and the corresponding simulations of the first TEHEX (featuring MTEG I with a active TEG area of 20 %) as function of the hot and cold fluid flow rate at an applied ΔT_0 of 50 K. With increasing flow rates, higher Seebeck voltages and powers can be reached (Fig. 5.9 a) and b)). However, the large pumping power caused by high pressure losses at the hot side µHTS significantly reduces the systems net performance, in particular at higher fluid flow rates (Fig. 5.9 b)). A maximal net power is found at a hot and cold flow rate of around 2 l/min. The large pressure losses are a result of a
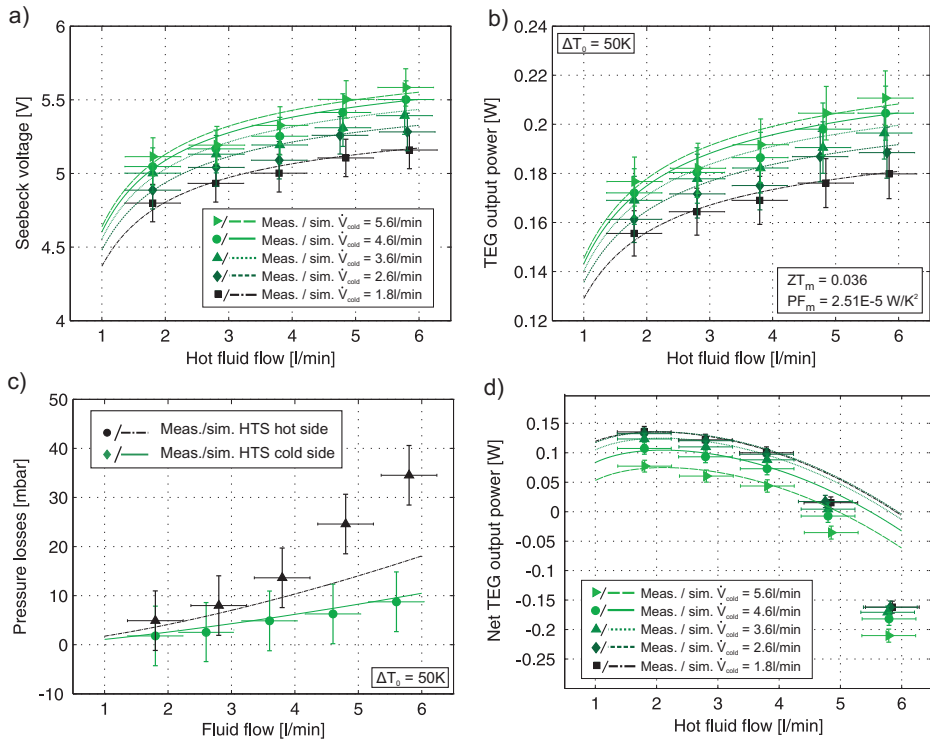
Figure 5.9: Measurements (markers) and simulations (lines) of the large size TE-HEX I. a) Seebeck voltage b) output power c) pressure losses and d) net output power as a function of the fluid flow rate at a fluid inlet temperature difference of $\Delta T_0 = 50$ K. The µHTS and TEG parameters used for the experimental measurements and corresponding simulations can be found in Tab. B.7 (MTEG I) and Tab. B.6 (MF$_{hot}$ I) in App. B.

too small manifold channel height at the hot side and therefore the occurrence of turbulent flow (Re $\gg$ 2300). This is also the reason for large model deviations, since turbulent flow is not taken into account in the 1D model.

Figure 5.10 a) shows the temperature difference between the inlet and outlet of the µHTSs. The larger heat absorption at the cold fluid side can be explained by the 20 µm reduced microchannel width (see Tab. B.6). The resulting calculated heat flux through the heat exchanger ranges from 400 to 520 W (increases with increasing flow rate). In Figure 5.10 b), the temperature change inside the manifold inlet channels are plotted. At the hot µHTS side, a slightly higher temperature difference is measured. On one hand, this can be explained by the decreased convective resistance K_{cnv} due to shorter manifold channels and
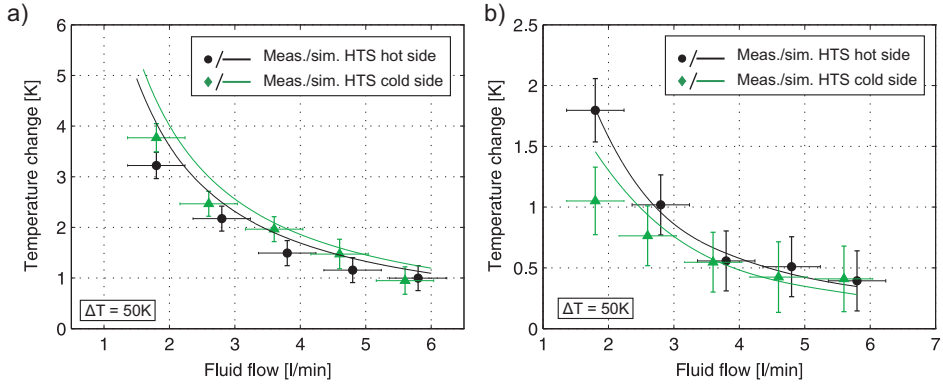
Figure 5.10: Measurements (markers) and simulations (lines) of temperature changes inside the TEHEX I with respect to the fluid flow rate. Temperature change between a) the fluid inlet and outlet and b) the fluid inlet and the end of the manifold inlet channel.

higher thermal conductivity of the fluid, and on the other hand by the difficult geometric placement of the thermocouple. Although the measured temperature difference is smaller than 2 K within the investigated flow and temperature range, this parasitic temperature change can influence the device performance, especially at lower flow rates.

Figure 5.11 a) shows the computed temperature gradients with respect to the fluid flow rate at four different points along the TEHEX cross-section: the fluid inlet ΔT_0, the effective average inlet ΔT_{in} after heat exchange inside the manifold channels, ΔT_w at the bottom of the microchannel base and ΔT_{TEG} directly across the generator. The temperature gradient drop from ΔT_{in} to ΔT_w occurs at the μHTSs ($K_{HTS_c} = 0.56$ - $1\,\text{cm}^2\text{K/W}$, $K_{HTS_h} = 0.52$ - $0.96\,\text{cm}^2\text{K/W}$) and from ΔT_w to ΔT_{TEG} at the interface (estimated $K_{interface} = 1.1\,\text{cm}^2\text{K/W}$, see Tab. B.8 for exact composition). The influence of the heat exchange inside the manifold channels causing the effective inlet temperature gradient ΔT_{in} to decrease is small compared to the temperature gradient drops produced by the μHTS and at the interfaces to the TEG. However, at a flow rate of 1 l/min, the effective inlet temperature is reduced by approximately 2.2 K and its effect can therefore not be neglected.
The total thermal contact resistance adds up to 2.2 - 3.1 cm²K/W, which is still smaller than the total generators resistance of 3.7 cm²K/W. Consequently, the TEG thickness should be further reduced.

For the second characterization run, an improved μHTS design, a decreased
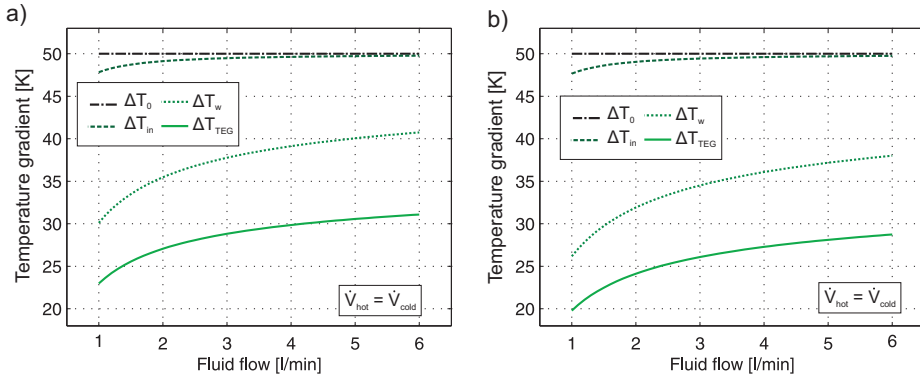
Figure 5.11: Simulated temperature gradients at four different points of the TEHEX with respect to the fluid flow for a) TEHEX I and b) TEHEX II. At smaller fluid flow rates, the impact of the heat exchange in the manifold channels is clearly visible (dashed line).

thermal interface resistance and a generator with higher active TE area is used (see MTEG II in Tab. B.7 in App. B, active TEG area of 51 %). The main redesign of the µHTS concerns the increase in manifold height at the hot fluid side. The interface resistance is lowered by depositing thinner passivation layers and using a thermal paste with higher conductivity.

The characterization results of the TEHEX II are summarized in Figure 5.12. With the increase of the active TE area form 20 to 51 % and lowered thermal interface resistance, a significantly higher Seebeck voltage and output power could be reached. The decrease in pumping power enabled by the higher manifold channels improved the net performance and shifted the optimal flow rates to higher values. In Figure 5.11 b), the simulated temperature profile across the second TEHEX is depicted. With an increased number of TC inside the polymer matrix, the generators thermal resistances K_{TEG} is reduced thus the effective thermal gradient across the TEG decreased. However, the smaller temperature gradient is compensated by the larger amount of TC and a smaller electrical resistance of the TEG. Additionally, the combination of a lower K_{TEG} (2.7 cm²K/W) and a total contact resistance K_{con} between 1.9 and 2.8 cm²K/W brings the TEHEX II closer to a thermally matched system.

In the optimal case where the active TEG area would be covered 100 % by TCs, the thermal resistance of the generator with the same thickness would reduce further to approximately 2 cm²K/W. This would potentially result in matched system even at higher fluid flow rates.
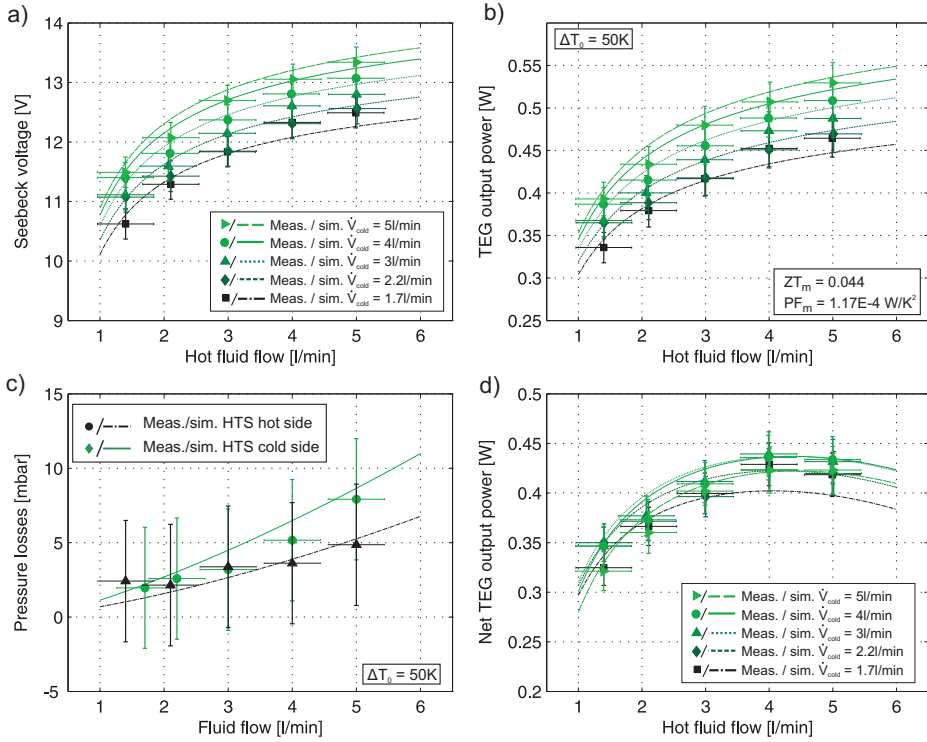
Figure 5.12: Measurements (markers) and simulations (lines) of the large size TEHEX II. a) Seebeck voltage b) output power c) pressure losses and d) net output power as a function of the fluid flow rate at a fluid inlet temperature difference of $\Delta T_0 = 50$ K. The µHTS and TEG parameters used for the experimental measurements and corresponding simulations can be found in Tab. B.7 (MTEG II) and Tab. B.6 (MF$_{hot}$ II) in App. B.

In order to evaluate the performance of the large size heat transfer system itself and better compare the TEHEX to state of the art devices, the thin film TEGs provided by greenTEG where exchanged with four 4×4 cm commercial TEGs (Eureca, see Tab. B.7 in App. B for details). Same µHTSs (Tab. B.6 (MF$_{hot}$ II) in App. B) and boundary conditions ($\Delta T_0 = 50$ K) were used as in the second characterization run. At a cold and hot fluid flow rate of 5 l/min, a Seebeck voltage of 11.6 ± 0.25 V, corresponding to a total and net output power of 4.92 ± 0.23 W and 4.76 ± 0.24 W was measured, respectively. This significantly higher output power of the TEHEX with commercial TEGs compared to the ones with thin film TEGs mainly results from reduced electrical resistance of the four TEGs connected in series (4×1.7 Ohm).

5.3 Conclusions

The net output performance of two differently sized TEHEX are characterized with respect to the applied boundary conditions, flow rates and system dimensions.
With the small size system, heat transfer resistances between $0.17 - 0.88\,\text{cm}^2\text{K/W}$ at corresponding low pumping powers of $6.8 - 0.06\,\text{mW/cm}^2$ are achieved. It is shown that by introducing high aspect ratio pin-fin structures inside the microchannels and combining it with an optimized fluid flow path, a further reduction of the heat transfer resistance and pressure losses can be reached at the same time.
Due to the coupled influence of TEHEX system parameters and boundary conditions, the net output performance can be optimized for different operating conditions by a careful design of the microchannels, an adaptation of the generator thickness and by applying an optimal fluid flow rate. A trade-off must be made between a low heat transfer resistance, i.e. a high effective temperature gradient, and the consumed pumping power. At smaller operating temperature differences, the impact of the pumping power outweighs the reduced K_{HTS} and thus smaller flows, wider channels and thicker TEGs lead to higher net powers. With a larger temperature gradient applied, the influence of the consumed pumping power decreases and the optimal flow rate increases, whereas the optimal microchannel width and generators thickness decrease as well.
The two layer small size TEHEX system reach up to $75\,\text{mW/cm}^2$ total power and $63\,\text{mW/cm}^2$ net power at ΔT_0 of $60\,\text{K}$. With a device height of $4.7\,\text{mm}$, this results in an absolute and net volumetric efficiency factor (VEF) of $44\,\text{W/m}^3\text{K}^2$ and $37\,\text{W/m}^3\text{K}^2$, respectively.

Two different designs of the scaled up TEHEX are successfully integrated and characterized. For the second TEHEX with improved design, a maximal output power of $0.53\,\text{W}$ and a net power of $0.44\,\text{W}$ is reached at an optimal fluid flow rate of $4\,\text{l/min}$ and an applied temperature gradient of $50\,\text{K}$. The corresponding total and net VEF reached are $3.1\,\text{W/m}^3\text{K}^2$ and $2.6\,\text{W/m}^3\text{K}^2$, respectively. If the fact is considered that only $51\,\%$ of the generator area is containing TC, the VEF for $100\,\%$ active area reaches $6.15\,\text{W/m}^3\text{K}^2$ total and $5.1\,\text{W/m}^3\text{K}^2$ net power, respectively. The large decrease in VEF compared to the small size TEHEX mainly lies in reduced TE performance of the TEGs (different PF_m per area), higher total contact resistance due to larger microchannels and thicker interfaces, and a less compact system caused by the upscaling of the manifold channels.
The large size TEHEX with integrated commercial TEGs reaches a total and net VEF of $23.3\,\text{W/m}^3\text{K}^2$ and $22.5\,\text{W/m}^3\text{K}^2$, respectively, due to the improved thermoelectric properties of the applied generators.

Figure 5.13 compares the presented results with data reported in literature. The small size TEHEX outperforms the best reported system by a factor of 4.8.
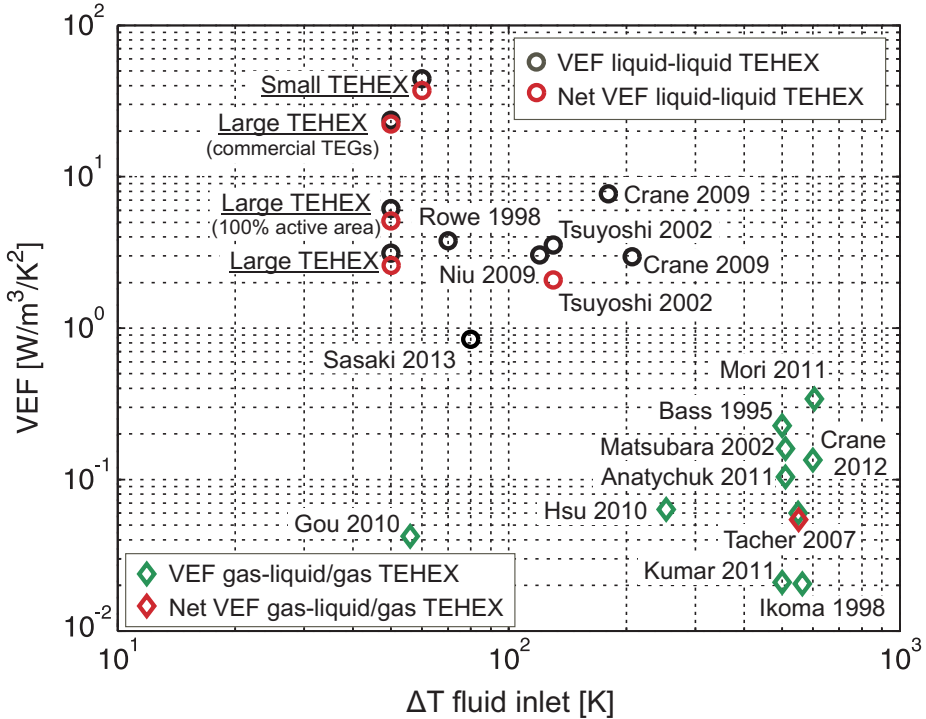
Figure 5.13: Volumetric efficiency factor VEF as a function of the applied fluid inlet temperature difference comparing published TEHEXs with results achieved in this work (marked with underlined labels).

The scaled up TEHEX also features the highest net VEF among the compared systems, despite the low TE performance of the TEGs applied.

The experimental results are in good agreement with the simulated small and large size system behavior. The validated 1D model can therefore be used for further system analysis and optimization in order to demonstrate its maximal potential.

6 Thermoelectric Heat Exchanger Simulations

In this chapter, the validated model described in Chapter 3 is applied for a systematic analysis and optimization of the characterized thermoelectric heat exchanger. Additionally, a case study is presented, where an estimation of the output performance and cost effectiveness for waste heat recovery in a marine propulsion engine is given.

6.1 Simulation results

In the first part of this section, the impact of individual TEG and µHTS parameters on the net output power and net VEF at an applied temperature gradient of 50 K are discussed. The second part deals with an overall system optimization with respect to the operating conditions.

The following system parameters are used and assumptions are made for the subsequent simulations:

- Same or similar TEG and µHTS parameters as in the 2nd large size TEHEX are used as standard simulation values (see Tab. B.9 col. 1 in App. B)

- A TEG with 100 % active area is used

- 1 periodic unit of the TEHEX is simulated

- µHTS dimensions are set identical for the hot and cold side (for Sec. 6.1.1 only)

- Matched electrical load for maximal power output according to Eq. 3.24

- Pump efficiency and losses at the connecting supply tubes are neglected

6.1.1 Impact of individual parameters

Figure 6.1 shows the influence of the microchannel width, TEG height and Seebeck coefficient on the net TEG output power with respect to the fluid flow rate. In Figure 6.2, the impact of most relevant system parameters on the net VEF is shown. In order to visualize the impact of the individual parameters, only the

Figure 6.1: TEHEX unit simulations of the large size device with respect to the fluid flow rates and different system parameters at a fluid inlet temperature difference of $\Delta T_0 = 50$ K. a) Heat transfer resistance and corresponding pumping power. Net output power as a function of b) the microchannel width, c) TEG height and d) the Seebeck coefficient.

parameter of interest is varied, while the remaining ones are kept constant according to Table B.9 in Appendix. B.

In Figure 6.1 a), the total heat transfer resistance K_{HTS} (sum of cold and hot side) and corresponding pumping power are plotted against different cold and hot fluid flow rates. The corresponding computed heat transfer coefficients vary from 1.1×10^4 to 1.58×10^4 W/m^{2}K at the hot side and from 1.06×10^4 to 1.44×10^4 W/m^{2}K at the cold side, respectively. In Figure 6.1 b), the influence of the microchannel width on the net power is depicted. With decreasing channel widths, the net power increases and the optimal fluid flow rate shifts to lower flow rates, analogous to the small size µHTS/µTEG system in Section 5.1.2. For the simulated TEHEX design and applied ΔT_0, the best performance is expected with a channel width of approximately 60 µm. However, the implementation of

such small channel widths has the disadvantage of potential channel clogging, apart from fabrication related challenges.

In Figure 6.1 c), the impact of the TEG height on the net power is shown. With increasing height and thus increasing TEG thermal resistance, the optimal flow rate will be reduced, i.e. the contact resistance increased. An enhanced Seebeck coefficient (Fig. 6.1 d)) will significantly increase the net power and shift the optimal fluid flow rate to higher values due to a reduced impact of the pumping power.

Figure 6.2 a) and b) show the relative change of the net VEF with respect to the variation of the parameter of interest from the standard values for the TEG and μHTS, respectively. For this impact comparison, the maximal achieved net value at the optimal flow rate is used. According to the conclusion in Section 3.1.5, the impact of the thermal conductivity is reduced compared to the electrical resistivity of the TE material. The influence of the spacing s between the TC has a significant effect on the geometric parameters of the TEG. The plot also shows that for a set distance of $s = 300\,\mu m$, not smaller, but large TC diameters will improve the performance. For the μHTS parameters (Fig. 6.2 b)), mainly a reduction of the microchannel width, the fin to channel ratio and manifold height as well as an increase in microchannel height would lead to a further system improvement. The decrease in manifold height, however, is strongly limited by the occurrence of turbulent flow and consequently incorrect model predictions (see Fig. 5.9 c)). A further reduction of the interface resistance would also significantly enhance the overall performance.
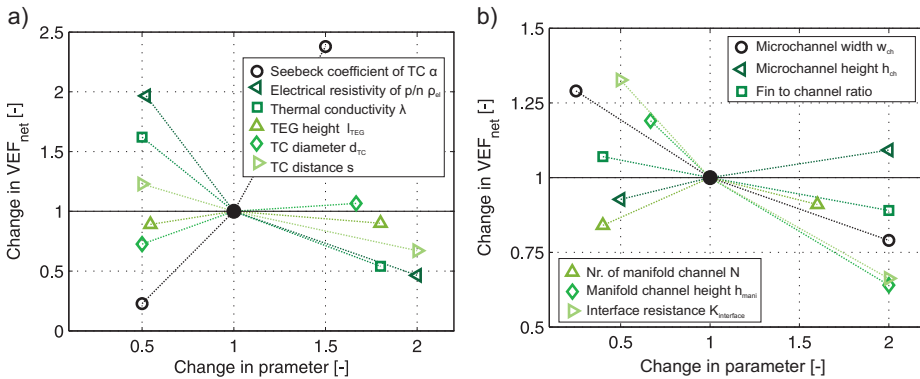
Figure 6.2: Relative change of the net VEF with respect to the variation of the parameter of interest from the standard values (see Tab. B.9) for a) the TEG and b) the μHTS at a $\Delta T_0 = 50\,K$.

The graphs show that the geometric parameters of both, the TEG and especially the µHTS, already are designed close to an optimal system. This design, complying with the current fabrication process constraints, results in very low heat transfer resistances and an approximately thermally matched system. Therefore, an enhancement of the figure of merit ZT or in particular of the power factor PF of the TEG is showing the largest effect on the TEHEX performance.

In Table 6.1, an overview of the major interdependencies or optimization trends of the TEG and µHTS geometric parameters for a maximal net performance of the TEHEX is given. Since the impact of the TE material properties are clear form the definition of ZT (see Eq. 3.2), they are omitted in the table.

Table 6.1: Overview of the major interdependencies or optimization trends of the TEG and µHTS parameters and operation conditions in order to maximize the net performance of the TEHEX. $f(x)$ stand for the dependency and $\Uparrow$ for the trend of the optimal parameter value of x.

	Name	Symbol	Trend
TEG	TEG length	l_{TEG}	$f(\Delta T_0, s, d_{TC}, \lambda)$
	TC diameter	d_{TC}	$f(\Delta T_0, s, l_{TEG}, \lambda)$
	TC distance	s	$\Downarrow$
	inactive/active mat.	AV	$f(\Delta T_0, s, \lambda)$
µHTS	microchannel width	w_{mc}	$f(\Delta T_0, h_{mc}, \chi)$
	microchannel height	h_{mc}	$\Uparrow$
	fin/channel ratio	χ	$\Downarrow$
	nr. of manifold channels	N	$f(\Delta T_0, para_{mc})$
	manifold channel height	h_{mani}	$f(\Delta T_0, para_{mc})$
	manifold channel base	l_{noz}	$\Downarrow$
Operating conditions	hot side flow rate	$\dot{V}_{cold}$	$f(\Delta T_0, para_{\mu HTS})$
	cold side flow rate	$\dot{V}_{hot}$	$f(\Delta T_0, para_{\mu HTS})$

6.1.2 System level optimization

Since the optimal parameters are dependent on the applied boundary condition as well as on each other, a combined parameter optimization to find the best overall design is necessary.

Figure 6.3 shows an example how the optimal flow rate and TEG thickness can change for three different temperature gradients applied. As a comparison, the effect on the TE conversion efficiency η (Eq. 3.10) is added to the graph (right side axis). With increasing ΔT_0 applied, the maximal net output power
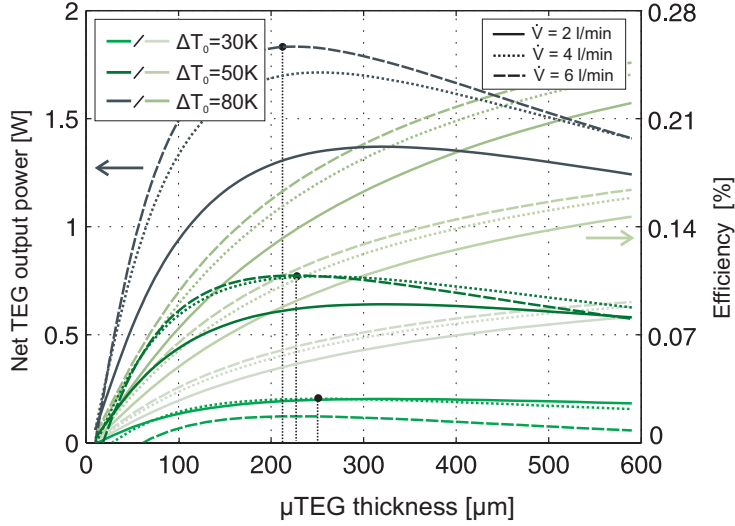
Figure 6.3: Effect of the TEG thickness and applied fluid flow rate on the net output power (dark green lines) and thermoelectric conversion efficiency (light green lines) of the TEHEX for three different fluid inlet temperature differences ΔT_0.

point (marked in the figure) shifts towards higher fluid flow rates and thinner TEGs. The optimal TEG thickness results from the matching of the TEG thermal resistance K_{TEG} with the sum of all the contact resistances K_{con} (see Sec. 3.1.4). Due to an increase in the optimal flow rate with increasing thermal gradients and corresponding reduction of the cold and hot heat transfer resistances, the optimal TEG thickness decreases as well. This influence on the optimal TEG thickness can be explained by the decrease in thermal coupling resistance K_{con} with respect to K_{TEG} (see Eq. 3.30).

The thermoelectric conversion efficiency continuously increases with rising fluid flow rates and thicker TEGs. The influence of the TEG thickness on η is a result of an increase in the ratio between ΔT_{TEG} across the generator and the externally applied ΔT_0 (refer to Eq. 3.30 and Fig. 3.8 for further details). A η of 0.25 % at a flow rate of 6 l/min and a ΔT_0 of 80 K corresponds to a second order efficiency of 1.7 % (Eq. 3.11). This low efficiency value has three main reasons: (1) low temperature operating ranges, (2) relatively low material and module ZT and PF and (3) low generator thicknesses for maximal power output. This shows that efficiency is not a suited measure for system optimization or comparison in low temperature thermoelectric waste heat recovery.

In Figure 6.4, the combination of the optimal values with respect to the applied thermal gradient is shown for the most relevant parameters. The optimal flow rate at the hot side shows a steeper slope than at the cold side (Fig. 6.4 a)). This can be explained with the temperature impact on the consumed pumping power: higher temperatures lead to a lower mean fluid density and mean fluid kinetic viscosity and thus a decreased pressure loss inside the channels. The influence is additionally enhanced by the larger manifold channel height at the hot side in order to avoid turbulent flow (see Tab. B.9 in App. B). The optimal TEG thickness and microchannel width reduce by approximately half of their value between a ΔT_0 of 10 K and a ΔT_0 of 80 K (Fig. 6.4 a) and b)). With decreasing TEG thickness, the optimal TC diameter decreases as well (see Fig. 3.6). The steadiness of the slope depends on the chosen step size between the discrete optimization simulations.
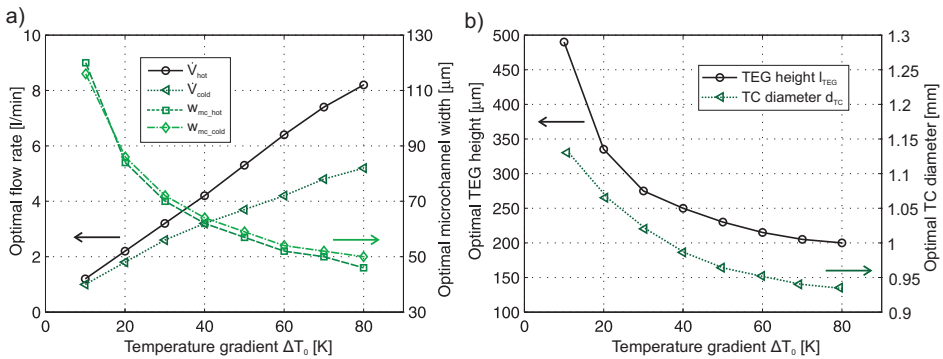
Figure 6.4: Optimal parameter values with respect to the applied temperature gradient: a) Hot and cold fluid flow rates and microchannel widths, b) TEG thickness and TC diameter.

6.1.3 Optimization routine

Due to complex parameter interdependencies and long computational times to determine the optimal parameter constellations, an optimization routine based on the 1D model is implemented and compared to the simulation results. A gradient based algorithm for multi-variable minimization revealed to be most suitable for the complex optimization problem (Matlab® *fmincon* with inter-point).

Three different methods for the computation of the starting points are applied and tested with respect to accuracy and execution time. Since the algorithm is programmed to find the closest local maximum, it is dependent on a suitable

starting point selection in order to converge to the global maximum. Table 6.2 summarizes the working principle, accuracy and computational time of all three starting point methods. Figure 6.5 shows the corresponding deviation of the net VEF from the simulation study with respect to the applied temperature gradients.

Table 6.2: Description of the applied starting point methods including the average deviations and computation times for an optimization study of five parameters.

Starting point method	Description	∅ Dev. [%]	∅ Time [s]
middle boundary	Takes the middle parameter value of the set min. and max. boundary	1.49	1366
multi-start	Randomly generates a specified number of starting points within the given boundaries	0.52	15178
global search	Applies an evolutionary algorithm to find optimal starting points	0.22	53331
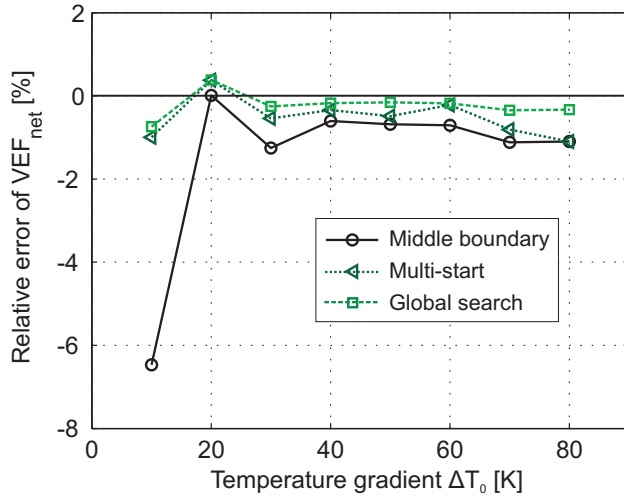
Figure 6.5: Relative deviation of the VEF computed by the optimization routine (for 5 parameters) applying three different starting point methods with respect to the simulation study as a function of the applied temperatures gradients.

The results found by the optimization algorithm are in good agreement with the values extracted by simulations for the 'global search' and 'multi-start' methods. However, the computational time is significantly higher compared to the 'middle boundary' starting point (see Tab. 6.2). Thus, a trade-off between run time and optimization accuracy must be made. The large deviation at lower temperatures are a result of the large relative error impact on the small net output power value. The deviation results of the individual parameters optimized for maximal net VEF can be found in Table B.2 in Appendix. B.

In Figure 6.6, the net output power and net VEF determined by the optimization routine are plotted and compared to the not optimized parameters from Table B.9 at a constant hot and cold fluid flow rate of 3 l/min. The optimization confirms the significant gain in net output performance by adapting geometrical parameters and operating conditions.
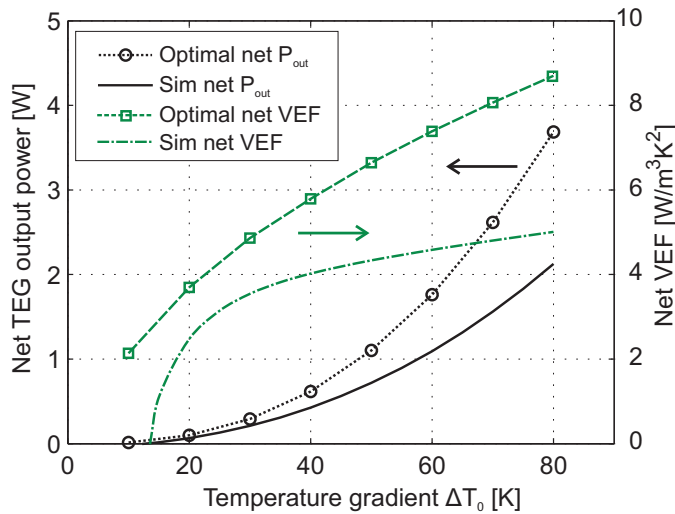
Figure 6.6: Optimal net output power and net VEF compared to simulated values with standard parameters from Tab. 6.2 and constant fluid flow rates of 3 l/min.

In order to demonstrate the potential of the TEHEX, the optimization routine is used to compute the net performance of a TEHEX combining improved thermoelectric properties with optimal system level parameters. For this calculations, the TE properties of the commercially available Bi_2Te_3 TEGs from Eureca (see Tab. B.7 in App. B) are used. The overall system optimization yields a maximum TEHEX unit net power of 11.8 W at an applied ΔT_0 of 50 K, resulting in a VEF

of $71.6\,\text{W}/\text{m}^3\text{K}^2$. The used TE properties and the computed optimal TEHEX dimensions and operation conditions can be found in Table B.10 in Appendix. B.

A graphical user interface (GUI) is implemented for a straight forward application of the 1D simulation model and the optimization code, including all three starting point methods (see App. C for more details).

6.2 Case study: marine propulsion engine

In order to evaluate the potential of the presented TEHEX for commercial use, the output performance is estimated in a concrete application scenario. As a promising example, the propulsion engine of a marine cargo vessel is chosen. The vessels are run by large diesel engines that need constant cooling during operation. With a shaft power efficiency close to 50 % [158], the engines generate large amounts of waste energy, mainly dissipated by the exhaust gas and by the cooling water into the environment.

In Figure 6.7, a schematic section of the cooling cycle of a 14 cylinder engine from Wärtsilä used for cargo vessels of approximately 300 m length is depicted[1].
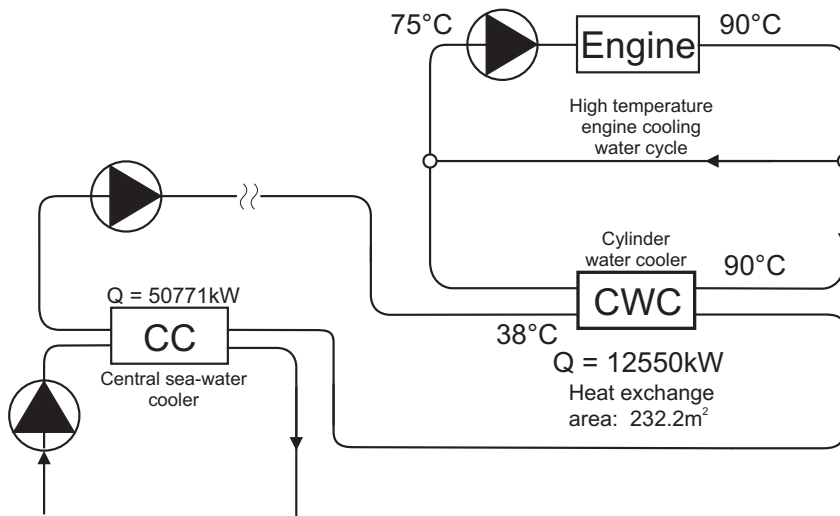
Figure 6.7: Schematic section of an exemplary cooling cycle of a 14 cylinder 14RT-flex-96C-B engine running at 85 % load.

---

[1]Data provided by Wärtsilä for the semester thesis of Barbara Schaffner.

The given data of the sample cooling cycle with a separate high temperature cycle for the engine correspond to normal propulsion under 85 % load. At the cylinder water cooler (CWC) heat exchanger, a water inlet temperature gradient of 52 K is available and a total heat amount of 12550 kW needs to be dissipated. The heat extracted by the engine jacket water corresponds to approx. 6.3 % of the total fuel input [158]. There are two possibilities to recover a part of this waste heat: either with an installed pre-cooler TEHEX or by directly replacing the existing heat exchanger with the proposed TEHEX. The latter option will be discussed here in more detail.

With the optimized design under optimal fluid flow rates for maximal net power and at the ΔT_0 of 52 K, a total heat flux of 873 W can be dissipated by one TEHEX unit. In order to extract the total necessary heat of 12550 kW, a total heat exchange area of 92 m^2 is needed. This is a factor 2.5 smaller than the area of the actually implemented CWC heat exchanger. The additional thermal resistance introduced by the thin film TEG can thus be successfully compensated with the efficient heat transfer system resulting in a higher heat flux per heat exchange area. With the current TE material properties of the modules ($PF_m = 4.7 \times 10^{-2}$ W/K^2, $ZT_m = 0.045$), a total of 16.8 kW net power could be generated.

In Figure 6.8, the net power of the directly installed TEHEX is plotted with respect to the power factor PF_m and TE figure of merit ZT_m. The three marked points in the graph correspond to the generator's TE properties with (1) the currently used Bi$_2$Te$_3$ material (material 1), (2) the state of the art single crystal Bi$_2$Te$_3$ [159] (material 2) and (3) nanostructured material with enhanced power factor like reported for Bi$_{0.52}$Sb$_{1.48}$Te$_3$ p-type material in [160] (material 3). With an improved material, up to 145 kW could potentially be recovered with the TEHEX installed in the high temperature engine cooling cycle and used to cover parts of the required ship service power.

This is only one possible example of waste heat recovery from the marine engine. Several other waste heat sources are available within the entire propulsions and service power plant, such as the central sea water cooler, the lubricant oil system, scavenge air cooler and the exhaust gas of the main and auxiliary engines [158].

6.2.1 Cost analysis

Based on the net output power values presented in the last section, the cost effectiveness of the TEHEX for the application in marine propulsion engines is estimated. In Figure 6.9 a), the investment cost per generated Watt is plotted with
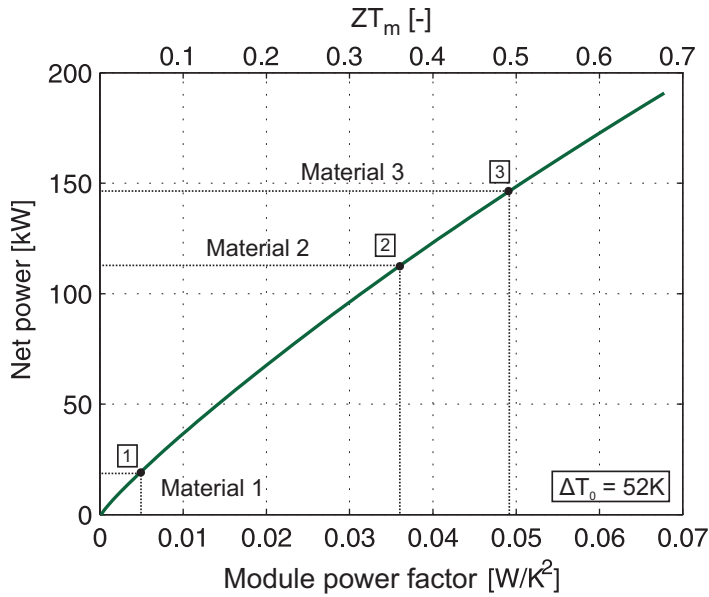
Figure 6.8: Net output power of the TEHEX installed in cooling cycle of a marine propulsion engine as a function of the PF_m and ZT_m of the TE module. The thermal conductivity of the TE material was kept constant at $2\,\text{W/mK}$ for the sweep of ZT_m.

respect to the price of the TEHEX unit for the three TE material properties of the module presented in Figure 6.8. Figure 6.9 b) shows the cost per kWh as a function of the device operation time for the three different TE materials for a TEHEX unit price of 40 CHF (marked in Fig. 6.9 a)). Maintenance costs are not included in the calculations. The two horizontal dashed lines mark the electricity prices offered by the ewz (Elektrizitätswerk der Stadt Zürich) for the year 2014 (Fig. 6.9 b)). With the assumed cost scenario and boundary conditions, a price of <1 CHF/kWh could be obtained for all three TE materials after a depreciation period of 4 years. With material 3, the price of standard electric power in Zurich could be reached after an operation time of two years.

6.3 Conclusions

The impact of the TEHEX design parameters on the net performance is demonstrated by means of the 1D model. Relevant parameter interdependencies as well as the importance of a system level optimization are highlighted and discussed. With the optimized design, a net performance enhancement of 65 % is shown com-
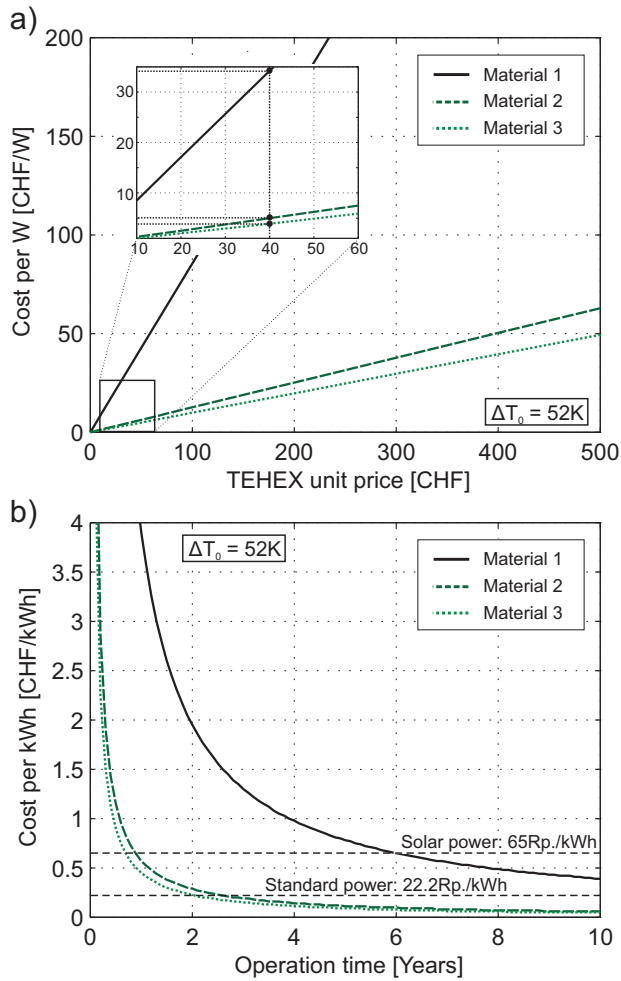
Figure 6.9: Net power costs for TEHEXs with three different TE materials calculated for the marine propulsion engine case study with an applied ΔT_0 of 52 K. a) Investment costs per generated Watt as a function of the TEHEX unit price. b) Cost per kWh with respect to the operation time for a TEHEX unit price of 40 CHF. The marked electricity prices are valid for private customers in Zurich for 2014.

pared to a TEHEX with the initial dimensions and a fixed fluid rate of 3l/min at a ΔT_0 of 50 K. To demonstrate the potential of the TEHEX, the system level optimization is used to compute the net performance of a device featuring improved thermoelectric properties. With a ZT_m and PF_m of 0.5 and 7.52×10^{-2} W/K^2, respectively, a net VEF of 71.6 W/m^{3}K^2 could potentially be achieved, which is an order of magnitude higher than best reported values.

An optimization routine is implemented and verified, which allows for a straightforward and fast system optimization for given specific boundary conditions and TE parameters of the module. With the optimized TEHEX design, a realistic case study on the application in a marine propulsion engine is conducted. It is shown that by installing the TEHEX in the engine cylinder cooling cycle, up to 145 kW could be harvested by applying improved TE materials. This power output corresponds to 1.16 % net and 10.1 % 2nd order efficiency, which is considerable for a high heat flux application and the low temperature of the waste heat recovered. A cost analysis yielded a minimal investment cost of 4 CHF/Watt or a power cost of 0.11 CHF/kWh for the assumed cost scenario and a payback period of 4 years. Furthermore, it is concluded that not the efficiency but rather the total net power must taken as a measure to compare different TEHEX systems for low temperature waste heat recovery in high heat flux applications.

7 Conclusion and Outlook

To overcome the present limitations of thermoelectric heat exchangers for low temperature waste heat recovery, a novel concept combining multi-layer high performance heat transfer systems and thin film generators is introduced. The µHTS consists of polymer manifold distribution channels sandwiched between copper plates featuring high aspect ratio microchannels. The system combines the advantage of very efficient heat dissipation and supply enabled by the microchannels as well as low pressure losses and homogeneous heat transfer enabled by the manifold distribution channels. Both characteristics are essential for an enhanced net performance of the TEHEX. Additionally, the implementation of an efficient µHTS allows for the application of µTEGs with thicknesses in the micrometer range in order to achieve a thermally matched system and thus optimal system conditions. This brings several advantages with respect to compactness, weight and cost and makes the system suitable for high heat flux waste heat recovery applications.

The proposed system is fabricated on two different size scales: a small 8 x 8 mm system for concept validation, detailed device analysis and potential demonstration and a large 9 x 9 cm system to prove the feasibility of a scalable fabrication process and investigate the suitability of the system for a commercial application in WHR. The main focus of the technology development is set on the fabrication of high aspect ratio copper microchannels. The small size fabrication process is based on electrochemical deposition of copper into a SU-8 mold structured by photolithography. Microchannel widths down to 30 µm with a channel aspect ratio of 7 are reached. The fabrication of additional heat transfer enhancement structures inside the microchannels resulted in vertical 30 µm wide pin-fins with aspect ratios of up to 8.1. An epoxy based bonding process is developed to assemble the microchannel chips to the polymer manifold channels fabricated by means of microstereolithography.

For the large size system, two microchannel fabrication approaches are evaluated: a bottom-up approach based on electroplating into a dry film resist mold and a top-down approach based on photolithography and etching. The latter approach yielded superior results with respect to process simplicity, processing time and fin to channel ratios and was therefore applied for the final demonstrator fabrication. Microchannel plates with 170 ± 10 µm high and 220 ± 15 µm wide channels and a fin to channel ratio of 0.5 ± 0.1 are implemented in the large size TEHEX.

The fabricated and assembled TEHEX are characterized in controlled fluid loops with respect to the generated net output power and net volumetric efficiency factor. The small size µHTS achieved heat transfer resistances between 0.17 and 0.88 cm²K/W at corresponding low pumping powers of 6.8 - 0.06 mW/cm². By combining pin-fin structures with rounded inlet/outlet nozzles, a further overall µHTS improvement can be reached. Due to the coupled influence of the µHTS and µTEG parameters and boundary conditions, the system's net output performance can be optimized for different operating conditions by the applied fluid flow rate and optimal system dimensions. With a two unit TEHEX, a net power of 63 mW/cm² at ΔT_0 of 60 K is reached, resulting in a net VEF of 37 W/m³K². This value can be further enhanced by reducing the µTEG thickness for optimal thermal matching and by implementing the proposed µHTS heat transfer improvements into the TEHEX.

Furthermore, it is concluded that for systems with good thermal coupling, the thermoelectric material optimization must focus more on the power factor instead of the figure of merit ZT itself, since the influence of the thermal resistance of the TE material is reduced.

The improved scaled up TEHEX with a 51 % active TEG area reached a maximal net power of 0.44 W at an optimal fluid flow rate of 4 l/min and an applied temperature gradient of 50 K. With the total volume of only 67.7 cm³, a net VEF of 2.6 W/m³K² is achieved for the current TEG and 5.1 W/m³K² could be reached for a 100 % active area TEG (see Fig. 5.13 in Chap. 5.3). Despite the low TE efficiency of the applied generators, this is the highest reported net VEF value, demonstrating the potential of the compact system over state of the art TEHEX.

A one-dimensional numerical TEHEX model is developed based on a network of thermal resistances. The model combines a precise TEG model including Joule heating and Peltier effect with a µHTS model implemented in an iterative computation routine. The influence of the temperature-dependent fluid parameters on the thermal resistance and pressure loss calculations in the µHTS is accounted for by introducing a discrete temperature profile inside the microchannels. Due to the small heat exchange between the manifold and the microchannel, a gradual fluid temperature change along the manifold channels is modelled as well. The implemented model allows for analysis and optimization of most geometric and material properties of the TEHEX, and shows a good agreement with the experimental results.

The verified model is applied for a detailed investigation of parameter impacts and interdependencies as well as a system level optimization. The impact of the pumping power on the overall system performance is large at smaller operating

temperature differences. Thus, smaller flow rates and wider channels and therefore thicker µTEGs and larger TC diameters lead to higher net performances in this operation regime. With a larger temperature gradient applied, the influence of the consumed pumping power decreases and the optimal flow rate increases, whereas the optimal microchannel width, µTEG thickness and TC diameter decrease. With a system level optimized TEHEX, a significant net performance enhancement and a net power gain starting form an applied thermal gradient of 10 K is predicted.

Based on the findings of the optimization study, a concrete example of waste heat recovery from a marine propulsion engine is calculated. With improved TE materials up to 145 kW could be harvested from the high temperature cylinder cooling cycle at an estimated investment cost of 4 CHF/Watt for a TEHEX unit cost of 40 CHF (footprint area of 81 cm^2).

Outlook

With respect to a further improvement of the technology, several investigations need to be conducted.

A reliable protective microchannel coating against corrosion and potential residue deposition must be developed and applied. The lifetime expectation and reliability of the TEHEX should be tested in an application related environment, in particular with respect to the durability of the polymer manifold channels. The effects of potential microchannel clogging caused by impurities in the feed water should be investigated in order to figure out the minimal applicable microchannel width for the specific applications or tolerable pressure loss introduced by fluid filters. An increase in microchannel height based on the bottom-up approach or alternative fabrication technologies should be explored. Moreover, further device upscaling will be necessary for most waste heat recovery applications.

As a next step, a promising application should be selected for field experiments, e.g. the proposed marine propulsion engine. The implemented design optimization tool can be applied to compute the optimal TEHEX design within given fabrication technology constraints and microchannel size limits imposed by the application. Finally, first prototypes can be built, installed and tested in a field environment.

Nevertheless, high density TEGs, improved TE material properties as well as low fabrication cost of the TEHEX are essential for successful commercialization.

A Processing

Process Runsheets

Table A.1: Fabrication runsheet for small size copper microchannels.

Process steps	Parameters	[Units]
Substrate cleaning		
Acetone/IPA US	5 @ 9	[min @ level]
Plasma asher	5 @ 600	[min @ W]
LOR layer		
Dehydration bake	5 @ 200	[min @ $^\circ$C]
LOR type/amount	10B/3	[-/ml]
Spreading	500/1000/15	[rpm/rpms^{-1}/s]
Spinning	3000/1000/30	[rpm/rpms^{-1}/s]
Bake	6 @ 195	[min @ $^\circ$C]
Seed layer evaporation		
Cr/Cu/Cr	10/1000/15	[nm/nm/nm]
SU-8 spin coating		
Dehydration	20 @ 140	[min @ $^\circ$C]
SU-8 type/amount	3050/5.5	[-/ml]
Spreading	500/100/20	[rpm/rpms^{-1}/s]
Spinning	1200/300/40	[rpm/rpms^{-1}/s]
Edge bead removal		
GBL placement	Directly on edge bead	[-]
Spread	600/300/8	[rpm/rpms^{-1}/s]
Spinning	1000/300/10	[rpm/rpms^{-1}/s]
Leveling	15	[min]
SU-8 Softbake		
Step 1	10 @ 65 ramped	[min @ $^\circ$C]

Continued on next page

Table A.1 – *Continued from previous page*

Process steps	Parameters	[Units]
Duration SB1/SB2	15 @ 80/55 @ 80	[min @ °C/min @ °C]
Ramping down	~1.2 to RT	[°Cmin^{-1}]
Cooling/relaxation 1,2	5/20	[min/min]
SU-8 exposure		
Type	Hard contact	[-]
Dose	1200	[mJcm^{-1}]
Step/pause times	10/30	[s/s]
SU-8 PE bake		
Duration	55 @ 65 ramped	[min @ °C]
Cooling/relaxation	15	[h]
SU-8 development		
Immersion in GBL	5	[min]
Immersion in mr-Dev 600	15	[min]
US agitation	4/2/1	[level]
Cu deposition		
Wetting	IPA/DI Water	[-]
Cleaning in 10% HNO$_3$	1	[min]
Degasing	5	[min]
Current density	3	[Adm^{-2}]
Deposition time	15	[h]
Lift-Off		
Immersion in DMSO	15	[h]

Table A.2: Fabrication runsheet of the large size copper microchannels for the bottom-up approach based on electroplating into a dry film resist mold.

Process steps	Parameters	[Units]
Substrate cleaning		
Polishing	2400	[-]
5% WaPS and H_2SO_4	3	[min]
HCL 10%	1	[min]
DFR lamination		
DFR type	Ordyl AM 175	[-]
DFR thickness	75	[μm]
1st run - adhesion	1 @ 95	[m/s @ $^\circ$C]
2nd run - lamination	0.2 @ 105	[m/s @ $^\circ$C]
Nr. of lamination	3	[-]
DFR exposure		
Type	Contact	[-]
Dose	58	[mJcm^{-1}]
DFR development		
Immersion in 2% $NaCO_3$	18	[min]
Rinsing in water	1	[min]
Cu deposition		
Wetting	IPA/DI Water	[-]
Cleaning in 10% HNO_3	1	[min]
Current density	1.4	[Adm^{-2}]
Deposition time	24	[h]
DFR stripping		
5% Ordyl Stripper 5600	1	[min]
Passivation		
Al_2O_3 e-beam evaporation	1	[μm]
BCB 3022-35 spincaoting	3000/1.3	[rpm/μm]

Table A.3: Fabrication runsheet of the large size copper microchannels for the top-down approach based on etching.

Process Steps	Parameters	[Units]
Substrate cleaning		
Polishing	2400	[-]
5% WaPS and H_2SO_4	3	[min]
HCL 10%	1	[min]
DFR lamination		
DFR type	Photec H-6230	[-]
DFR thickness	30	[μm]
1st run - adhesion	1 @ 60	[m/s @ °C]
2nd run - lamination	0.3 @ 95	[m/s @ °C]
Nr. of lamination	1	[-]
DFR exposure		
Type	Contact	[-]
Dose	40	[mJcm^{-1}]
DFR development		
Immersion in 2% $NaCO_3$	4	[min]
Rinsing in water	1	[min]
Cu etching[1]		
Etching time	12±1	[min]
Rinsing in water	1	[min]
DFR stripping		
5% Ordyl Stripper 5600	1	[min]
Passivation		
Al_2O_3 e-beam evaporation	1	[μm]
BCB 3022-35 spincaoting	3000/1.3	[rpm/μm]

[1]Etching solution consists of 500 g/l of $FeCl_3$ hexahydrate and 50 ml/l HCL solution (37 %).

Chemical Solutions

Table A.4: Composition of the copper electroplating bath for a bath volume of one liter.

Chemicals	Formula	Amount	Units
Copper sulfate	$CuSO_4$ - $5H_2O$	170-200	[g]
Sulfuric acid	H_2SO_4	60-70	[g]
Sodium chloride	NaCl	100-120	[mg]
Deionized water	H_20	-	[-]
CUMAC 9000WA[1] (brightener)	-	8-12	[ml]
CUMAC 9000B[1] (brightener)	-	1.8-2.3	[ml]
CUMAC 9000M[1] (additive)	-	0.5-0.8	[ml]

[1]The series of CUMAC 9000 is supplied by MacDermid Plc.

B Measurement and Simulation Data

Supporting equations

Thermoelectric generator
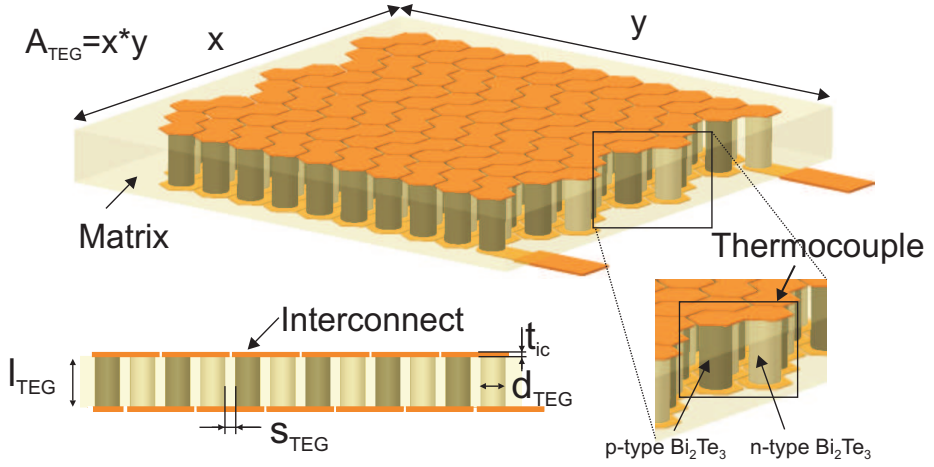
Figure B.1: Schematic of a thermoelectric generator.

The TEG thermal resistance reads

$$K_{TEG} = \frac{A_{TEG}}{m} \frac{l_{TEG}}{\left(\lambda_p A_{a-p} + \lambda_n A_{a-n} + \lambda_{is}(A_{i-p} + A_{i-n})\right)} = \frac{A_{TEG}}{2mA_a} \frac{l_{TEG}}{\lambda + AV\lambda_{is}}$$
(B.1)

where m is the number of thermocouples, A_{TEG} is the area of the generator, l_{TEG} is the TC lenght, λ_p and λ_n are the thermal conductivities and A_{a-p} and A_{a-n} are the cross section areas of the p and n type TC, respectively. λ_{is} the thermal conductivity of the matrix and A_{i-p} and A_{i-n} the corresponding matrix areas of the two thermocouples. The second part of Eq. B.1 is valid for same properties of the p and n type TC ($\lambda_p = \lambda_n = \lambda$ and $A_{a-p} = A_{a-n} = A_a$). The number of TC is

$$m = \frac{A_{TEG}}{(A_{a-p} + A_{a-n})(1 + AV)}$$
(B.2)

The total TEG electrical resistance is the sum of three terms

$$R_{el} = m \left(R_{tc} + R_{ic} + R_c \right) \tag{B.3}$$

where R_{tc} is the electrical resistance of the thermocouples, R_{ic} is the interconnect and R_c the electrical contact resistance. With

$$R_{tc} = \frac{\rho_{el\_n}}{A_{a-p}} l_{TEG} + \frac{\rho_{el-p}}{A_{a-n}} l_{TEG} = 2 \frac{\rho_{el}}{A_a} l_{TEG} \tag{B.4}$$

where the second part of Eq. B.4 is valid for same properties of the p and n type TC ($\rho_{el-p} = \rho_{el\_n} = \rho_{el}$ and $A_{a-p} = A_{a-n} = A_a$).

$$R_{ic} = 4 \frac{\rho_{ic} \, t_{ic}}{2 \, A_a} + 2 \frac{0.5 \sqrt{3} \, d_{TEG} + s}{d_{TEG} \, t_{ic}} \tag{B.5}$$

where ρ_{ic} is the electrical resistivity of the interconnect material, t_{ic} is the interconnect thickness, d_{TEG} is the TC diameter and s is the distance between the piles.

$$R_c = 2 \left(R_{c-p} + R_{c\_n} \right) = 4 \frac{\rho_c}{d_{TEG}} \tag{B.6}$$

where ρ_c is the specific contact resistance.

The transformed basic heat balance equations at the hot and cold junction are

$$Q_{in} = (A - B) \, T_h^2 - (A - 2B) \, T_h \, T_c - B \, T_c^2 + \frac{(T_h - T_c)}{K_{TEG}} \tag{B.7}$$

$$Q_{out} = B \, T_h^2 + (A - 2B) \, T_h \, T_c - (A - B) \, T_c^2 + \frac{(T_h - T_c)}{K_{TEG}} \tag{B.8}$$

with

$$A = \frac{m^2 \, \alpha^2}{R_l + R_{el}} \tag{B.9}$$

and

$$B = \frac{m^2 \, \alpha^2}{2(R_l + R_{el})^2} \, R_{el} \tag{B.10}$$

Micro heat transfer system

The apparent friction factor-Reynolds number product $f_{app}\text{Re}$ in non-circular ducts for laminar developing flow is given as a function of the aspect ratio of

the duct according to [124, 125]

$$f_{app} \, \mathrm{Re} = \left[\left(\frac{12}{\sqrt{\epsilon} \, (1 + \epsilon) \left[1 - \frac{192\epsilon}{\pi^5} \tanh(\frac{\pi}{2\epsilon}) \right]} \right)^r + \left(\frac{3.44}{\sqrt{x^+}} \right)^r \right]^{1/r} \quad \text{(B.11)}$$

where ϵ is the aspect ratio of the duct, $x^+ = x/(d \, \mathrm{Re})$ is the dimensionless position for hydrodynamically developing flows, and r is a correlation parameter which lies in the range of $1.5 < r < 3.6$. Eq. B.11 should predict the friction factor for most of the non-circular ducts within $\pm 10\%$ accuracy.

The Nusselt number correlation for constant wall heat flux boundary condition and simultaneously developing flow provided by [127] reads

$$\mathrm{Nu}(x^*) = \left[\left(\frac{C_4 f(\mathrm{Pr})}{\sqrt{x^*}} \right)^b + \left(\left\{ C_2 C_3 \left(\frac{f_{app} \mathrm{Re}}{x^*} \right)^{1/3} \right\}^5 + \left\{ C_1 \left(\frac{f_{app} \mathrm{Re}}{8\sqrt{\pi} \epsilon^\tau} \right) \right\}^5 \right)^{b/5} \right]^{1/b} \quad \text{(B.12)}$$

where $b = 2.27 + 1.65 \, \mathrm{Pr}^{1/3}$ is a blending parameter, $x^* = x/(d \, \mathrm{Re} \, \mathrm{Pr})$ is the dimensionless position for thermally developing flows, ϵ is the aspect ratio of the duct, τ is a shape parameter and C_{1-4} are parameters depending on the boundary condition and the application of the local or average Nusselt number. The Prandtl number (Pr) correlates the kinematic viscosity or momentum diffusivity to the thermal diffusivity. It is defined as

$$\mathrm{Pr} = \frac{\nu}{\kappa} = \frac{c_p \, \mu}{\lambda_f} \quad \text{(B.13)}$$

where κ is the thermal diffusivity, ν is the kinematic viscosity, c_p is the specific heat capacity, μ is the dynamic viscosity, and λ_f is the thermal conductivity of the fluid. For large Prandtl numbers, the convection dominates over conduction (for small Prandtl numbers vice versa).

The fin efficiency is defined by [161]

$$\eta_f = \frac{\tanh{(n \, h_{fin})}}{n \, h_{fin}} \quad \text{(B.14)}$$

111

where h_{fin} is the fin height and n is

$$n = \sqrt{\frac{\overline{h}_{fin}\, p_{fin}}{\lambda_{Cu}\, w_{fin}}} = \sqrt{\frac{\overline{h}_{fin}\, 2(w_{fin} + l_{uc})}{\lambda_{Cu}\, w_{fin}\, l_{uc}}} \cong \sqrt{\frac{2\overline{h}_{fin}}{\lambda_{Cu}\, w_{fin}}} \qquad \text{(B.15)}$$

where p_{fin} is the perimeter, d_{fin} is the width and l_{uc} is length of the fin.

Simulation and device parameters

Table B.1: Parameters of the thermoelectric generator used for the theory visualisations and simulation in Sec. 3.1 (if not varied or otherwise specified).

	Symbol	Value	Unit
Material properties	α	661	μV/K
	ρ_{el}	1.38	E-5 Ω m
	λ	1.4	W/mK
	λ_{is}	0.47	W/mK
	$Z\overline{T}$	1.73	-
Geometric parameters	l_{TEG}	200	μm
	d_{TC}	680	μm
	s	330	μm
	AV	1.44	-
	t_{ic}	15	μm
TEG properties	R_{el}	1.35	Ω
	K_{TEG}	2.35	cm^{2}K/W
	$Z\overline{T}_m$	1	-
	A_{TEG}	0.42	cm^2
Boundary cond.	K_{con}	2.35	cm^{2}K/W
	ΔT_0	10	K

Table B.2: µHTS parameters used for measurement and simulations in Sec. 3.2.3 and Sec. 5.1. In the 1D model a thermal paste thickness of 25 µm was assumed, corresponding to a total thermal resistance of 0.07 cm^{2}K/W.

	Channel height	Channel width	Fin/chan. wall width	Base/noz. height	Channel number	Slot size	Total area
	[µm]	[µm]	[µm]	[µm]	[-]	[µm]	[µm]
Micro-channels	185	diff	w_{ch}	50	diff	-	8x8
Manifold MF I	1000	150-300	110	200	9	150	8.5x12
Manifold MF II	1000	150-300	140	400	9	150	8.5x12

Table B.3: Comparison of relevant parameters of the 1D µHTS model from Sec. 3.2.3 to the 3D FEM simulations of the unit cell and to µHTS measurements for different channel widths w_{ch}, fluid flow rates $\dot{V}$ and applied temperature gradients ΔT_0.

w_{ch}	$\dot{V}$	ΔT_0	Dev. from 3D FEM			Dev. from measurements			
[µm]	[l/min]	[K]	[%]			[%]			
			K_{HTS}	Δp_{mc}	ΔT_{mc}	K_{HTS}	Δp_{HTS}	ΔT_{mc}	ΔT_{MF}
80	0.02	5	12.3	-28.9	-3.0	1.3	-28.3	14.3	17.8
80	0.04	5	7.1	-11.5	1.5	1.3	-7.3	4.2	-2.6
80	0.06	5	4.6	-7.3	1.0	1.3	-2.1	-6.2	-12.2
80	0.08	5	1.0	1.9	-4.8	1.2	-1.1	-20.9	-17.1
80	0.1	5	-0.4	3.5	-8.5	1.6	-0.9	-25.7	-8.3
80	0.12	5	-2.2	7.6	-13.6	0.6	-0.5	-26.0	-10.6
60	0.04	5	6.1	-18.6	11.0	-2.7	-2.1	7.7	-
35	0.04	5	-2.8	-39.4	16.0	-2.1	-0.6	8.3	19.7
80	0.04	10	7.4	-16.8	1.4	2.0	-7.8	5.8	-
80	0.04	20	7.7	-3.9	1.8	2.0	-5.6	66.0	-

Table B.4: Simulation and design parameters of microchannels with integrated microstructures.

	ΔT_0 [K]	w_{mc} [μm]	w_{fin} [μm]	h_{mc} [μm]	$w_{noz/2}$ [μm]	l_{noz} [μm]	d_{pin} [μm]	prot. [μm]	pitch [μm]
3D FEM	5	40-100	w_{mc}	200	150	60	20-50	30/50	97.5/130-390
Meas.	5	80	80	200+10	150	400	30	30/50	97.5/130-390

Table B.5: Parameters of the small size thermoelectric modules.

TEG label	size [mm]	V_{sb} [mV/K]	R_{el} [Ω]	K_{TEG} [cm²K/W]	$Z\overline{T}_m$[1] [-]	PF_m [E-5 W/K²]	l_{TEG} [μm]
STEG I	7x7 ± 0.2	5.8 ± 0.3	2.4 ± 0.05	5.1 ± 0.3	0.047 ± 0.01	1.4 ± 0.1	215 ± 15
STEG II	7x7 ± 0.2	5.5 ± 0.3	1.3 ± 0.05	2.7 ± 0.3	0.044 ± 0.01	2.4 ± 0.1	210 ± 10
STEG III	7x7 ± 0.2	6.7 ± 0.3	1.2 ± 0.05	2.4 ± 0.3	0.065 ± 0.01	3.8 ± 0.1	215 ± 10
Laird [2]	8.1x8.1	11.74	4.7	16.2	0.22	2.95	2180
Nextreme[3]	3.3x3.1	25	9.7	1.34	0.25	6.45	570
STEG IV	7x7 ± 0.2	6.15 ± 0.3	1.2 ± 0.05	2[4] ± 0.3	0.044 ± 0.01	3.2 ± 0.1	215 ± 10
STEG V[5]	7x7 ± 0.2	6.7 ± 0.3	1.2 ± 0.05	2[4] ± 0.3	0.052 ± 0.01	3.7 ± 0.1	215 ± 10

[1]At $\overline{T}$ = 300 K.
[2]Device OT20, V_{sb} and K_{TEG} were calculated from technical data found in the datasheet.
[3]Device TEG HV56.
[4]Thermal resistance calculated based on thermal conductivity data provided by greenTEG.
[5]Average values of the two TEGs used.

Table B.6: Large size µHTS parameters used for measurements and simulations in Sec. 5.2.

	Channel height	Channel width	Fin/chan. wall width	Base/noz. height	Channel number	Slot size	Total area
	[mm]	[mm]	[µm]	[µm]	[-]	[µm]	[cm]
MC_{cold}	0.17	0.23	100	230	242	-	9x9
MC_{hot}	0.17	0.21	120	230	242	-	9x9
MF_{cold}	3.9	0.35-2.35	300	700	25	300	9x9
MF_{hot} I	1.6	0.35-2.35	300	500	25	300	9x9
MF_{hot} II	3.9	0.35-2.35	300	700	25	300	9x9

Table B.7: Parameters of the large size thermoelectric modules.

TEG label	size [cm^2]	A_{act} [3] [%]	#TCx#TEG [-]	V_{sb} [mV/K]	R_{el} [Ω]	K_{TEG} [cm^{2}K/W]	$Z\overline{T}_m$ [1] [-]	l_{TEG} [µm]
MTEG I	64 ± 0.2	20 ± 1	29x30 -	165 ± 12	37 ± 0.5	3.7[2] ± 0.3	0.036 ± 0.01	220 ± 15
MTEG II	64 ± 0.2	51 ± 1	116x20 -	443[4] ± 20	84 ± 1	2.7[2] ± 0.3	0.044 ± 0.01	220 ± 15
Eureca[5]	64 ± 0.5	100 -	200x4 ± 0.15	329.2 ± 7	6.8 ± 0.3	10.3 ± 0.2	0.77 ± 0.015	3200 -

[1] At $\overline{T} = 300$ K.
[2] Thermal resistance calculated based on thermal conductivity data provided by greenTEG: $\lambda_{n/p} = 2$ W/mK $\lambda_{is} = 0.47$ W/mK.
[3] Defined as percentage of active TE area with integrated TC to the total TEG area.
[4] Estimated, since not measured.
[5] Device TEG1-40-40-10/100. Data is given for four modules connected in series. Calculated $PF_m = 15.9$ E-3 W/K^2.

Table B.8: Composition of the thermal interface layers of the large size TEHEX.

	Thickness [μm]	Thermal conductivity [W/mK]	Thermal resistance [cm^{2}K/W]
Epoxy package	2x10	0.3	0.66
Thermal paste	2x30	3.6	0.14
Al$_2$O$_3$	2x1.5	30	0.001
BCB	2x2.6	0.2	0.32
TEHEX I	total		**1.1**
Epoxy package	2x10	0.3	0.67
Thermal paste	2x30	12.5	0.05
Al$_2$O$_3$	2x1	30	0.0007
BCB	2x1.3	0.2	0.13
TEHEX II	total		**0.85**

Table B.9: Set of standard parameters of the TEHEX used for the simulation in Sec. 6.1.1 (if not varied or otherwise specified).

Device	Properties	Symbol	Mat. 1	Mat. 2	Mat. 3	Unit
TEG	Mater. proper.	α	200^1	390^4	450^5	µV/K
		ρ_{el}	2.3^1	1^4	1	E-5Ω m
		λ	2^1	2^4	2	W/mK
		λ_{is}	0.47^1	0.47^1	0.47^1	W/mK
		$Z\overline{T}^2$	0.0652	0.57	0.76	-
	Geom. param.	l_{TEG}	220	280	280	µm
		d_{TC}	600	980	980	µm
		s	300	300	300	µm
		AV	1.48	0.83	0.83	-
		t_{ic}	15	15	15	µm
	TEG properties	R_{el}	255	27.5	27.5	Ω
		V_{sb}	1.1	1.09	1.26	V/K
		K_{TEG}	2.03	2.15	2.15	cm^{2}K/W
		$Z\overline{T}_m$	0.045	0.37	0.49	-
		PF_m	4.7	37	49	E-3 W/K^2
		A_{TEG}	64	64	64	cm^2
µHTS	Microchannels	w_{mc}	200	200	200	µm
		h_{mc}	200	200	200	µm
		χ	0.5	0.5	0.5	-
		t_{base}	300	300	300	µm
	Manifold ch.	N	25	25	25	-
		h_{mani}	3^3	3/4.5	3/4.5	mm
		l_{noz}	800	800	800	µm
		w_{noz}	300	300	300	µm
Interface resistance		$K_{interface}$	0.85	0.85	0.85	cm^{2}K/W

[1] Parameter based on current small size TEGs data provided by greenTEG.

[2] At $\overline{T} = 300$ K

[3] For the optimization in Sec. 6.1.2, the hot side manifold was increased to 4.5 mm in order to avoid turbulent flow at higher temperatures.

[4] Single crystal Bi$_2$Te$_3$ [159]

[5] Bi$_{0.52}$Sb$_{1.48}$Te$_3$ p-type material [160]
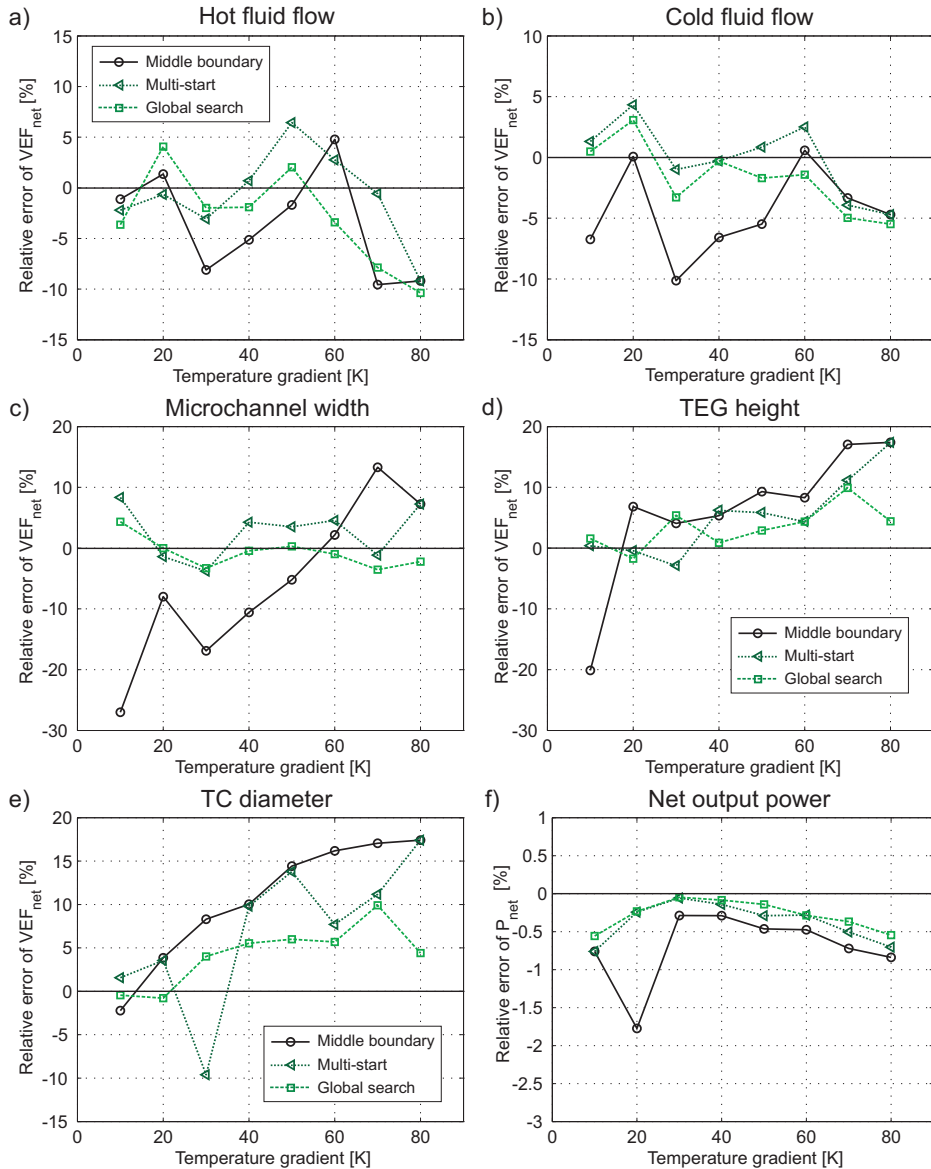
Figure B.2: Results of the optimization routine applying three different starting point methods showing the relative deviations of individual TEHEX parameters optimized for maximal net VEF (a)-e)) and of the maximal net output power (f)) with respect to the simulation study (Tab. 6.4 in Sec. 6.1.2) as a function of the applied temperatures gradients.

Table B.10: TE properties and by means of the system level optimization routine computed optimal TEHEX dimensions and operation conditions used for the estimation of the TEHEX potential in Sec. 6.1.3.

Device	Properties	Symbol	Mat. 1	Unit
TEG	Mater. proper.	α	410[1]	µV/K
		ρ_{el}	0.7[1]	E-5Ω m
		λ	2[1]	W/mK
		λ_{is}	0.47[2]	W/mK
		$Z\overline{T}$[3]	0.94	-
	Geom. param.	l_{TEG}	190	µm
		d_{TC}	1060	µm
		s	300	µm
		AV	0.76	-
		t_{ic}	25	µm
	TEG properties	R_{el}	13.9	Ω
		V_{sb}	1.02	V/K
		K_{TEG}	1.42	cm^{2}K/W
		$Z\overline{T}_m$	0.5	-
		PF_m	75.3	E-3 W/K^2
		A_{TEG}	64	cm^2
µHTS	Microchannels	w_{mc}	40	µm
		h_{mc}	200	µm
		χ	0.5	-
		t_{base}	300	µm
	Manifold ch.	N	25	-
		h_{mani}	3/4.5	mm
		l_{noz}	800	µm
		w_{noz}	300	µm
Interface resistance		$K_{interface}$	0.85	cm^{2}K/W
Hot flow rate		$\dot{V}_{hot}$	8	l/min
Cold flow rate		$\dot{V}_{cold}$	7	l/min

[1]Estimated parameter of Eureca TEG1-40-40-10/100.
[2]Parameter based on current small size TEGs data provided greenTEG.
[3]At $\overline{T} = 300\,\text{K}$

C GUI

The graphical user interface (GUI) is implemented for a straight forward hand-
ling of the complex 1D model and the optimization routine. The user interface
is divided into four sections: definition of the parameters (Fig. C.1), simulation
(Fig. C.2), optimization (Fig. C.3) and graphical interpretation (Fig. C.4).

In the parameter and boundary definition section, the values for the µTEG,
µHTS and the boundary conditions can be defined. It can be chosen from the op-
tions of selecting standard predefined values for the small or large size devices, of
defining own values or performing a parameter sweep of any selected parameter.

Figure C.1: Definition of the input parameters for the TEG, the µHTS and the
boundary conditions.

The GUI allows for the simulation of the μTEG or μHTS alone, the μHTS/μTEG system or the periodic TEHEX unit. The simulated output data can be scanned to find the optimal dimension and flow rate constellation, either for the net output power or the net VEF. Additionally, data can be imported or exported into or from the GUI, respectively.
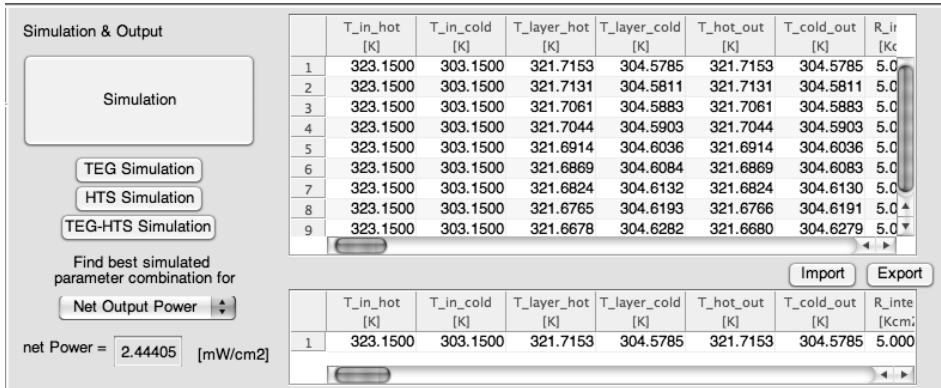
Figure C.2: Simulation run and parameter output including selection of optimal parameters for maximal net power or net VEF.

In the optimization section, the target parameter to be optimized (net output power, net VEF) as well as the staring point method (middle boundary, multistart, global search) can be selected. The output data will be displayed in the table below.
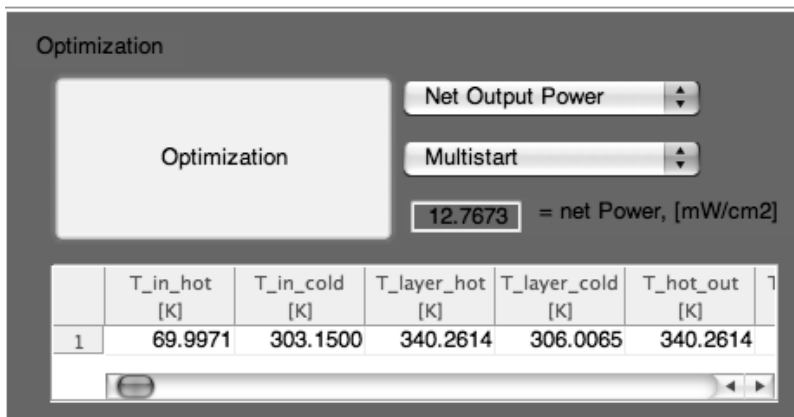
Figure C.3: Optimization run and parameter output including selection of the objective value and starting point method.

In the graphical interpretation of the simulated data, the number of displayed plots and the parameter of interest can be chosen. Furthermore, the plots can be exported for further usage.
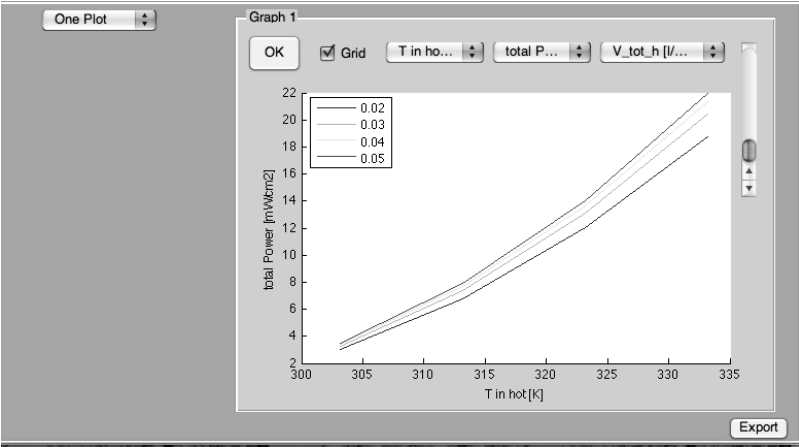
Figure C.4: Graphical interpretation of the simulated data.

Bibliography

[1] J. Yagi and T. Akiyama, "Storage of thermal-energy for effective use of waste heat from industries," *Journal of Materials Processing Technology*, vol. 48, no. 1-4, pp. 793–804, 1995.

[2] A. S. Rattner and S. Garimella, "Energy harvesting, reuse and upgrade to reduce primary energy usage in the USA," *Energy*, vol. 36, no. 10, pp. 6172–6183, 2011.

[3] K. M. Saqr and M. N. Musa, "Critical review of thermoelectrics in modern power generation applications," *Thermal Science*, vol. 13, no. 3, pp. 165–174, 2009.

[4] "Annual electric generator report," U.S. Energy Information Administration, Tech. Rep., 2001.

[5] A. B. Little and S. Garimella, "Comparative assessment of alternative cycles for waste heat recovery and upgrade," *Energy*, vol. 36, no. 7, pp. 4492–4504, 2011.

[6] C. N. Markides, "The role of pumped and waste heat technologies in a high-efficiency sustainable energy future for the UK," *Applied Thermal Engineering*, vol. 53, no. 2, pp. 197–209, 2013.

[7] E. J. Chaisson, "Long-term global heating from energy usage," *Eos, Transactions American Geophysical Union*, vol. 89, no. 28, pp. 253–254, 2008.

[8] B. Nordell and B. Gervet, "Global energy accumulation and net heat emission," *International Journal of Global Warming*, vol. 1, no. 1-3, pp. 378–391, 2009.

[9] G. Min and D. Rowe, "Peltier devices as generators," in *CRC Handbook of Thermoelectric*, 1st ed., ch. 38, D. Rowe, Ed., Boca Raton, FL: CRC Press, 1995.

[10] S. B. Riffat and X. L. Ma, "Thermoelectrics: a review of present and potential applications," *Applied Thermal Engineering*, vol. 23, no. 8, pp. 913–935, 2003.

[11] L. E. Bell, "Cooling, heating, generating power, and recovering waste heat with thermoelectric systems," *Science*, vol. 321, no. 5895, pp. 1457–1461, 2008.

[12] C. B. Vining, "An inconvenient truth about thermoelectrics," *Nature Materials*, vol. 8, no. 2, pp. 83–85, 2009.

[13] D. Rowe, "Thermoelectric waste heat recovery as a renewable energy source," *International Journal of Innovations in Energy Systems and Power*, vol. 1, no. 1, pp. 13–23, 2006.

[14] D. M. Rowe, "Thermoelectric harvesting of low temperature natural/waste heat," *9th European Conference on Thermoelectrics (ECT'11), Proceedings*, vol. 1449, pp. 485–492, 2012.

[15] J. C. Bass, R. J. Campana, and N. B. Elsner, "Thermoelectric generator for diesel trucks," *10th International Conference on Thermoelectrics (ICT'91), Proceedings*, 1991.

[16] J. H. Yang and F. R. Stabler, "Automotive applications of thermoelectric materials," *Journal of Electronic Materials*, vol. 38, no. 7, pp. 1245–1251, 2009.

[17] M. Kishi, H. Nemoto, T. Hamao, M. Yamamoto, S. Sudou, and M. Mandai, "Micro thermoelectric modules and their application to wristwatches as an energy source," *18th International Conference on Thermoelectrics (ICT'99), Proceedings*, pp. 301–307, 1999.

[18] R. J. M. Vullers, R. van Schaijk, I. Doms, C. Van Hoof, and R. Mertens, "Micropower energy harvesting," *Solid-State Electronics*, vol. 53, no. 7, pp. 684–693, 2009.

[19] A. Elefsiniotis, D. Samson, T. Becker, and U. Schmid, "Investigation of the performance of thermoelectric energy harvesters under real flight conditions," *Journal of Electronic Materials*, vol. 42, no. 7, pp. 2301–2305, 2013.

[20] D. M. Rowe, "Applications of nuclear-powered thermoelectric generators in space," *Applied Energy*, vol. 40, no. 4, pp. 241–271, 1991.

[21] G. L. Bennett, R. J. Hemler, and A. Schock, "Space nuclear power: An overview," *Journal of Propulsion and Power*, vol. 12, no. 5, pp. 901–910, 1996.

[22] T. R. Lamp and B. D. Donovan, "Unattended power sources for remote, harsh environments," *29th Intersociety Energy Conversion Engineering Conference, Proceedings, Pts 1-4*, pp. 688–693, 1994.

[23] T. K. Hunt, R. K. Sievers, and A. C. Patania, "Small AMTEC systems as battery substitutes," *Space Technology and Applications International Forum, Pts 1 and 2*, vol. 504, pp. 1356–1360, 2000.

[24] R. Venkatasubramanian, E. Siivola, T. Colpitts, and B. O'Quinn, "Thin-film thermoelectric devices with high room-temperature figures of merit," *Nature*, vol. 413, no. 6856, pp. 597–602, 2001.

[25] T. C. Harman, P. J. Taylor, M. P. Walsh, and B. E. LaForge, "Quantum dot superlattice thermoelectric materials and devices," *Science*, vol. 297, no. 5590, pp. 2229–2232, 2002.

[26] J. P. Heremans, M. S. Dresselhaus, L. E. Bell, and D. T. Morelli, "When thermoelectrics reached the nanoscale," *Nature Nanotechnology*, vol. 8, no. 7, pp. 471–473, 2013.

[27] W. Glatz, "Development of flexible micro thermoelectric generators," Dissertation, ETH Zurich, Diss ETH No. 17766, 2008.

[28] E. Schwyter, "Fully characterized flexible micro thermoelectric generator based on a large scale fabrication approach," Dissertation, ETH Zurich, Diss ETH No. 20891, 2013.

[29] Y. Lin, Y. Tzeng, M. Dai, C. Liu, L. Liao, H. Chien, Y. Chen, and K. Wang, "Multi-force-field assisted self-assembly process of thermoelectric device," *17th International Conference on Solid-State Sensors, Actuators and Microsystems, Proceedings*, pp. 818–821, 2013.

[30] J. W. Stevens, "Optimal design of small DT thermoelectric generation systems," *Energy Conversion and Management*, vol. 42, no. 6, pp. 709–720, 2001.

[31] J. R. Couper, W. R. Penney, J. R. Fair, and S. M. Walas, "Heat transfer and heat exchangers," in *Chemical process equipment selection and design*, 3rd ed., ch. 8, pp. 161–221., Waltham, Mass.: Butterworth-Heinemann, 2012.

[32] D. B. Tuckerman and R. F. W. Pease, "High-performance heat sinking for vlsi," *Electron Device Letters*, vol. 2, no. 5, pp. 126–129, 1981.

[33] G. L. Morini, "Single-phase convective heat transfer in microchannels: a review of experimental results," *International Journal of Thermal Sciences*, vol. 43, no. 7, pp. 631–651, 2004.

[34] B. Agostini, M. Fabbri, J. E. Park, L. Wojtan, J. R. Thome, and B. Michel, "State of the art of high heat flux cooling technologies," *Heat Transfer Engineering*, vol. 28, no. 4, pp. 258–281, 2007.

[35] C. E. Hunt, C. A. Desmond, D. R. Ciarlo, and W. Benett, "Direct bonding of micromachined silicon wafers for laser diode heat exchanger applications," *Journal of Micromechanics and Microengineering*, vol. 1, no. 3, pp. 152–156, 1991.

[36] E. G. Colgan, B. Furman, M. Gaynes, N. LaBianca, J. H. Magerlein, R. Polastre, R. Bezama, K. Marston, and R. Schmidt, "High performance and subambient silicon microchannel cooling," *Journal of Heat Transfer-Transactions of the ASME*, vol. 129, no. 8, pp. 1046–1051, 2007.

[37] W. Escher, T. Brunschwiler, B. Michel, and D. Poulikakos, "Experimental investigation of an ultrathin manifold microchannel heat sink for liquid-cooled chips," *Journal of Heat Transfer-Transactions of the ASME*, vol. 132, no. 8, p. 081402 (10pp), 2010.

[38] L. Boteler, N. Jankowski, B. Geil, and P. McCluskey, "A micromachined manifold microchannel cooler," *ASME International Mechanical Engineering Congress and Exposition (IMCE2009), Proceedings*, vol. 5, no. 43789, pp. 61–68, 2009.

[39] G. P. Peterson and C. S. Chang, "Two-phase heat dissipation utilizing porous-channels of high-conductivity material," *Journal of Heat Transfer-Transactions of the ASME*, vol. 120, no. 1, pp. 243–252, 1998.

[40] Y. Peles, A. Kosar, C. Mishra, C. J. Kuo, and B. Schneider, "Forced convective heat transfer across a pin fin micro heat sink," *International Journal of Heat and Mass Transfer*, vol. 48, no. 17, pp. 3615–3627, 2005.

[41] A. Kosar and Y. Peles, "Thermal-hydraulic performance of MEMS-based pin fin heat sink," *Journal of Heat Transfer-Transactions of the ASME*, vol. 128, no. 2, pp. 121–131, 2006.

[42] A. Renfer, M. K. Tiwari, F. Meyer, T. Brunschwiler, B. Michel, and D. Poulikakos, "Vortex shedding from confined micropin arrays," *Microfluidics and Nanofluidics*, vol. 15, no. 2, pp. 231–242, 2013.

[43] T. Brunschwiler, H. Rothuizen, M. Fabbri, U. Kloter, B. Michel, R. J. Bezama, and G. Natarajan, "Direct liquid jet-impingement cooling with micronsized nozzle array and distributed return architecture," *10th Intersociety Conference on Thermal and Thermomechanical Phenomena in Electronics Systems, Proceedings*, vol. 1 and 2, pp. 196–203, 2006.

[44] W. Escher, B. Michel, and D. Poulikakos, "A novel high performance, ultra thin heat sink for electronics," *International Journal of Heat and Fluid Flow*, vol. 31, no. 4, pp. 586–598, 2010.

[45] D. M. Rowe, "The NEDO/Cardiff thermoelectric project to economically recover low temperature waste heat," *17th International Conference on Thermoelectrics (ICT'98), Proceedings*, pp. 18–24, 1998.

[46] K. Matsuura, D. M. Rowe, A. Tsuyoshi, and G. Min, "Large scale thermoelectric generation of low grade heat," *10th International Conference on Thermoelectrics (ICT'91), Proceedings*, pp. 233–241, 1991.

[47] A. Tsuyoshi and K. Matsuura, "A trial manufacture of a thermoelectric generator powered by high-temperature heat transfer medium oil," *Electrical Engineering in Japan*, vol. 141, no. 1, pp. 36–44, 2002.

[48] X. Niu, J. L. Yu, and S. Z. Wang, "Experimental study on low-temperature waste heat thermoelectric generator," *Journal of Power Sources*, vol. 188, no. 2, pp. 621–626, 2009.

[49] D. T. Crane, J. W. LaGrandeur, F. Harris, and L. E. Bell, "Performance results of a high-power-density thermoelectric generator: Beyond the couple," *Journal of Electronic Materials*, vol. 38, no. 7, pp. 1375–1381, 2009.

[50] K. Sasaki, D. Horikawa, and K. Goto, "Consideration of thermoelectric power generation by using hot spring thermal energy or industrial waste heat," *32nd International Conference on Thermoelectrics (ICT'13)*, 2013.

[51] U. Birkholz, E. Grob, U. Stohrer, K. Voss, D. O. Gruden, and W. Wurster, "Conversion of waste exhaust heat in automobiles using $FeSi_2$ thermoelements," *7th International Conference on Thermoelectric Energy Conversion (ICT '88), Proceedings*, pp. 124–128, 1988.

[52] J. C. Bass, N. B. Elsner, and F. A. Leavitt, "Performance of the 1 kW thermoelectric generator for Diesel engines," *13th International Conference on Thermoelectrics (ICT'94), Proceedings*, no. 316, pp. 295–298, 1995.

[53] J. C. Bass, A. S. Kushch, and N. B. Elsner, "Thermoelectric generator (TEG) for heavy diesel trucks," *20th International Conference on Thermoelectrics (ICT'01), Proceedings*, pp. 1–5, 2001.

[54] K. Ikoma, M. Munekiyo, K. Furuya, M. Kobayashi, T. Izumi, and K. Shinohara, "Thermoelectric module and generator for gasoline engine vehicles," *17th International Conference on Thermoelectrics (ICT'98), Proceedings*, pp. 464–467, 1998.

[55] K. Matsubara, "Development of a high efficient thermoelectric stack for a waste exhaust heat recovery of vehicles," *21st International Conference on Thermoelectrics (ICT'02), Proceedings*, pp. 418–423, 2002.

[56] D. T. Crane and G. S. Jackson, "Optimization of cross flow heat exchangers for thermoelectric waste heat recovery," *Energy Conversion and Management*, vol. 45, no. 9-10, pp. 1565–1582, 2004.

[57] E. F. Thacher, B. T. Helenbrook, M. A. Karri, and C. J. Richter, "Testing of an automobile exhaust thermoelectric generator in a light truck," *Proceedings of the Institution of Mechanical Engineers Part D-Journal of Automobile Engineering*, vol. 221, no. D1, pp. 95–107, 2007.

[58] X. L. Gou, H. Xiao, and S. W. Yang, "Modeling, experimental study and optimization on low-temperature waste heat thermoelectric generator system," *Applied Energy*, vol. 87, no. 10, pp. 3131–3136, 2010.

[59] C. T. Hsu, D. J. Yao, K. J. Ye, and B. Yu, "Renewable energy of waste heat recovery system for automobiles," *Journal of Renewable and Sustainable Energy*, vol. 2, no. 1, 2010.

[60] C. R. Kumar, A. Sonthalia, and R. Goel, "Experimental study on waste heat recovery from an internal combustion engine using thermoelectric technology," *Thermal Science*, vol. 15, no. 4, pp. 1011–1022, 2011.

[61] L. I. Anatychuk, Y. Y. Rozver, and D. D. Velichuk, "Thermoelectric generator for a stationary diesel plant," *Journal of Electronic Materials*, vol. 40, no. 5, pp. 1206–1208, 2011.

[62] L. I. Anatychuk and R. V. Kuz, "Computer design and test results of automotive thermoelectric generator," in *Thermoelectrics Goes Automotive*, vol. 2nd, pp. 191–208, D. Jänsch, Ed., Renningen: expert verlag, 2011.

[63] L. I. Anatychuk, O. J. Luste, and R. V. Kuz, "Theoretical and experimental study of thermoelectric generators for vehicles," *Journal of Electronic Materials*, vol. 40, no. 5, pp. 1326–1331, 2011.

[64] M. Mori, T. Yamagami, M. Sorazawa, T. Miyabe, S. Takahashi, and T. Haraguchi, "Fuel economy simulation of series hybrid utilizing thermoelectric heat recovery system," in *Thermoelectrics Goes Automotive*, pp. 154–167, D. Jänsch, Ed., Renningen: expert verlag, 2011.

[65] D. Crane, L. Bell, and J. LaGrandeur, "Progress report on vehicular waste heat recovery using a cylindrical thermoelectric generator," in *Thermoelectrics Goes Automotive*, vol. 2nd, pp. 83–91, D. Jänsch, Ed., Renningen: expert verlag, 2011.

[66] D. T. Crane, C. R. Koripella, and V. Jovovic, "Validating steady-state and transient modeling tools for high-power-density thermoelectric generators," *Journal of Electronic Materials*, vol. 41, no. 6, pp. 1524–1534, 2012.

[67] D. Crane, J. LaGrandeur, V. Jovovic, M. Ranalli, M. Adldinger, E. Poliquin, J. Dean, D. Kossakovski, B. Mazar, and C. Maranville, "TEG on-vehicle performance and model validation and what it means for further TEG development," *Journal of Electronic Materials*, vol. 42, no. 7, pp. 1582–1591, 2013.

[68] T. Kajikawa, "Present state of R&D on thermoelectric technology in Japan," *20th International Conference on Thermoelectrics (ICT'01), Proceedings*, pp. 49–56, 2001.

[69] H. H. Braess and U. Seiffert, *Vieweg Handbuch Kraftfahrzeugtechnik*, 6th ed., Springer DE, 2011.

[70] J. L. Creveling, "Means for utilizing waste energy," US Patent US1 118 269 A, 1914.

[71] A. J. Neild, "Portable thermoelectric generators," *SAE-645A (Society of Automotive Engineers)*, 1963.

[72] D. Jaensch, *Thermoelectric Goes Automotive*, 2nd ed., p. 295., Renningen: expert verlag, 2011.

[73] J. Salvador, "Challenges for future implementation of thermoelectric waste heat recovery," *32nd International Conference on Thermoelectrics (ICT'13)*, 2013.

[74] M. Linde, B. Mazar, A. Eder, S. Neugebauer, and R. Brueck, "Der AGR-TEG: Ein Pilotprojekt auf dem Weg zur Industrialisierung der Thermoelektrik im Kraftfahrzeug," in *Thermoelectrics Goes Automotive*, vol. 2nd, pp. 71–82, D. Jänsch, Ed., Renningen: expert verlag, 2011.

[75] J. Yang and F. R. Stabler, "Automotive applications of thermoelectric materials," in *Thermoelectrics and its energy harvesting. Modules, systems, and applications in thermoelectrics*, D. M. Rowe, Ed., Boca Raton, FL: CRC Press, 2012.

[76] D. B. Heymann, C. D. Meyer, N. R. Jankowski, and B. C. Morgan, "Modeling the system impact of cooling performance on a compact thermoelectric generator," *PowerMEMS 2009, Proceedings*, 2009.

[77] D. Astrain, J. G. Vian, A. Martinez, and A. Rodriguez, "Study of the influence of heat exchangers' thermal resistances on a thermoelectric generation system," *Energy*, vol. 35, no. 2, pp. 602–610, 2010.

[78] K. Yazawa and A. Shakouri, "Cost-efficiency trade-off and the design of thermoelectric power generators," *Environmental Science & Technology*, vol. 45, no. 17, pp. 7548–7553, 2011.

[79] A. Rezania and L. A. Rosendahl, "Evaluating thermoelectric power generation device performance using a rectangular microchannel heat sink," *Journal of Electronic Materials*, vol. 40, no. 5, pp. 481–488, 2011.

[80] A. Rezania and L. A. Rosendahl, "Thermal effect of a thermoelectric generator on parallel microchannel heat sink," *Energy*, vol. 37, no. 1, pp. 220–227, 2012.

[81] A. Rezania, L. A. Rosendahl, and S. J. Andreasen, "Experimental investigation of thermoelectric power generation versus coolant pumping power in a microchannel heat sink," *International Communications in Heat and Mass Transfer*, vol. 39, no. 8, pp. 1054–1058, 2012.

[82] B. Mathew, B. Jakub-Wood, E. Ogbonnaya, and L. Weiss, "Investigation of a MEMS-based capillary heat exchanger for thermal harvesting," *International Journal of Heat and Mass Transfer*, vol. 58, no. 1-2, pp. 492–502, 2013.

[83] T. J. Seebeck, *Magnetische Polarisation der Metalle und Erze durch Temperatur-Differenz*, p. 120., Leipzig: Wilhelm Engelmann, 1823.

[84] S. Middelhoek and S. Audet, *Silicon sensors*, ser. Microelectronics and signal processing, p. 376., London: Academic Press In, 1989.

[85] R. Pelster, R. Pieper, and I. Huettl, "Thermospannung - Viel genutzt und fast immer falsch erklärt," in *PhyDid*, vol. 1, pp. 10–22, 2005.

[86] M. Cutler and N. F. Mott, "Observation of Anderson localization in an electron gas," *Physical Review*, vol. 181, no. 3, pp. 1336–1340, 1969.

[87] H. Fritzsch, "General expression for thermoelectric power," *Solid State Communications*, vol. 9, no. 21, pp. 1813–1815, 1971.

[88] N. W. Ashcroft and N. D. Mermin, *Solid state physics*, 1st ed., p. 826., New York: Holt, Rinehart and Winston, 1976.

[89] M. Freunek, "Untersuchung der Thermoelektrik zur Energieversorgung autarker Systeme," Dissertation, University Freiburg, 2010.

[90] A. F. Ioffe, *Semiconductor Thermoelements and Thermoelectric Cooling.*, London: Infosearch, ltd, 1957.

[91] L. D. Hicks and M. S. Dresselhaus, "Effect of quantum-well structures on the thermoelectric figure of merit," *Physical Review B*, vol. 47, no. 19, pp. 12 727–12 731, 1993.

[92] L. D. Hicks and M. S. Dresselhaus, "Thermoelectric figure of merit of a one-dimensional conductor," *Physical Review B*, vol. 47, no. 24, pp. 16 631–16 634, 1993.

[93] L. D. Hicks, T. C. Harman, X. Sun, and M. S. Dresselhaus, "Experimental study of the effect of quantum-well structures on the thermoelectric figure of merit," *Physical Review B*, vol. 53, no. 16, pp. 10 493–10 496, 1996.

[94] Y. M. Lin, X. Z. Sun, and M. S. Dresselhaus, "Theoretical investigation of thermoelectric transport properties of cylindrical Bi nanowires," *Physical Review B*, vol. 62, no. 7, pp. 4610–4623, 2000.

[95] J. P. Heremans, C. M. Thrush, D. T. Morelli, and M. C. Wu, "Thermoelectric power of bismuth nanocomposites," *Physical Review Letters*, vol. 88, no. 21, 2002.

[96] K. F. Hsu, S. Loo, F. Guo, W. Chen, J. S. Dyck, C. Uher, T. Hogan, E. K. Polychroniadis, and M. G. Kanatzidis, "Cubic AgPb$_m$SbTe$_{2+m}$: Bulk thermoelectric materials with high figure of merit," *Science*, vol. 303, no. 5659, pp. 818–821, 2004.

[97] D. M. Rowe, "Theoretical optimization of thermoelectric figure of merit of heavily doped hot-pressed germanium-silicon alloys," *Journal of Physics F-Metal Physics*, vol. 7, no. 13, pp. 1843–1846, 1974.

[98] G. A. Slack and M. A. Hussain, "The maximum possible conversion efficiency of silicon-germanium thermoelectric generators," *Journal of Applied Physics*, vol. 70, no. 5, pp. 2694–2718, 1991.

[99] D. G. Cahill, W. K. Ford, K. E. Goodson, G. D. Mahan, A. Majumdar, H. J. Maris, R. Merlin, and P. Sr, "Nanoscale thermal transport," *Journal of Applied Physics*, vol. 93, no. 2, pp. 793–818, 2003.

[100] J. Yang, W. Zhang, S. Q. Bai, Z. Mei, and L. D. Chen, "Dual-frequency resonant phonon scattering in Ba$_x$R$_y$Co$_4$Sb$_1$2 (R=La, Ce, and Sr)," *Applied Physics Letters*, vol. 90, no. 19, 2007.

[101] A. I. Hochbaum, R. K. Chen, R. D. Delgado, W. J. Liang, E. C. Garnett, M. Najarian, A. Majumdar, and P. D. Yang, "Enhanced thermoelectric performance of rough silicon nanowires," *Nature*, vol. 451, no. 7175, pp. 163–167, 2008.

[102] K. Biswas, J. Q. He, I. D. Blum, C. I. Wu, T. P. Hogan, D. N. Seidman, V. P. Dravid, and M. G. Kanatzidis, "High-performance bulk thermoelectrics with all-scale hierarchical architectures," *Nature*, vol. 489, no. 7416, pp. 414–418, 2012.

[103] J. P. Heremans, V. Jovovic, E. S. Toberer, A. Saramat, K. Kurosaki, A. Char-oenphakdee, S. Yamanaka, and G. J. Snyder, "Enhancement of thermoelec-tric efficiency in PbTe by distortion of the electronic density of states," *Science*, vol. 321, no. 5888, pp. 554–557, 2008.

[104] K. Matsuura and D. Rowe, "Low-temperature heat conversion," in *CRC Handbook of Thermoelectric*, 1st ed., ch. 44, D. Rowe, Ed., Boca Raton, FL: CRC Press, 1995.

[105] C. Wu, "Analysis of waste-heat thermoelectric power generators," *Applied Thermal Engineering*, vol. 16, no. 1, pp. 63–69, 1996.

[106] M. Strasser, "Entwicklung und Charakterisierung mikrostrukturierter ther-moelektrischer Generatoren in Silizium-Halbleitertechnologie," Dissertation, Technische Universität München, 2002.

[107] L. G. Chen, J. Z. Gong, F. R. Sun, and C. Wu, "Effect of heat transfer on the performance of thermoelectric generators," *International Journal of Thermal Sciences*, vol. 41, no. 1, pp. 95–99, 2002.

[108] M. Strasser, R. Aigner, C. Lauterbach, T. F. Sturm, M. Franosch, and G. Wachutka, "Micromachined CMOS thermoelectric generators as on-chip power supply," *Sensors and Actuators A: Physical*, vol. 114, no. 2-3, pp. 362–370, 2004.

[109] M. Freunek, M. Muller, T. Ungan, W. Walker, and L. M. Reindl, "New physical model for thermoelectric generators," *Journal of Electronic Materials*, vol. 38, no. 7, pp. 1214–1220, 2009.

[110] Y. Apertet, H. Ouerdane, O. Glavatskaya, C. Goupil, and P. Lecoeur, "Optimal working conditions for thermoelectric generators with realistic thermal coupling," *EPL*, vol. 97, no. 2, 2012.

[111] C. N. Rollinger and J. E. Sunderland, "The performance of a convectively cooled thermoelement used for power generation," *Solid-State Electronics*, vol. 3, no. 3-4, pp. 268–277, 1961.

[112] B. R. West, "A method for designing a thermoelectric generator based on the thermal characteristics of the device," *Advanced Energy Conversion*, vol. 2, pp. 209–218, 1962.

[113] M. Strasser, R. Aigner, M. Franosch, and G. Wachutka, "Miniaturized ther-moelectric generators based on poly-Si and polySiGe surface micromachin-ing," *Sensors and Actuators A: Physical*, vol. 97-8, pp. 535–542, 2002.

[114] W. Glatz, S. Muntwyler, and C. Hierold, "Optimization and fabrication of thick flexible polymer based micro thermoelectric generator," *Sensors and Actuators A: Physical*, vol. 132, no. 1, pp. 337–345, 2006.

[115] J. Stevens, "Optimized thermal design of small DT thermoelectric generators," *34th Intersociety Energy Conversion Engineering Conference, Proceedings*, pp. 1999–01–2564, 1999.

[116] Y. Ma, Q. Hao, B. Poudel, Y. C. Lan, B. Yu, D. Z. Wang, G. Chen, and Z. F. Ren, "Enhanced thermoelectric figure-of-merit in p-type nanostructured bismuth antimony tellurium alloys made from elemental chunks," *Nano Letters*, vol. 8, no. 8, pp. 2580–2584, 2008.

[117] W. Kim, J. Zide, A. Gossard, D. Klenov, S. Stemmer, A. Shakouri, and A. Majumdar, "Thermal conductivity reduction and thermoelectric figure of merit increase by embedding nanoparticles in crystalline semiconductors," *Physical Review Letters*, vol. 96, no. 4, 2006.

[118] T. C. Harman, M. P. Walsh, B. E. Laforge, and G. W. Turner, "Nanostructured thermoelectric materials," *Journal of Electronic Materials*, vol. 34, no. 5, pp. L19–L22, 2005.

[119] D. Narducci, "Do we really need high thermoelectric figures of merit? a critical appraisal to the power conversion efficiency of thermoelectric materials," *Applied Physics Letters*, vol. 99, no. 10, 2011.

[120] F. Incropera, D. P. Dewitt, T. L. Bergman, and A. S. Lavine, *Fundamentals of heat and mass transfer*, 6th ed., p. 997., Hoboken, NJ: John Wiley & Sons, 2007.

[121] R. W. Hanks and H. C. Ruo, "Laminar-turbulent transition in ducts of rectangular cross section," *Industrial & Engineering Chemistry Fundamentals*, vol. 5, no. 4, pp. 558–561, 1966.

[122] R. K. Shah and A. L. London, *Laminar Flow Forced Convection in Ducts*.Academic Press, New York, 1978.

[123] M. M. Yovanovich and Y. S. Muzychka, "Solutions of poisson equation within singly and doubly connected domains," *AIAA Paper*, vol. 97-3880, pp. 1–11, 1997.

[124] Y. S. Muzychka and M. M. Yovanovich, "Modeling friction factors in non-circular ducts for developing laminar flow," *AIAA Paper*, vol. 98-2492, pp. 1–12, 1998.

[125] Y. S. Muzychka and M. M. Yovanovich, "Pressure drop in laminar developing flow in noncircular ducts: A scaling and modeling approach," *Journal of Fluids Engineering-Transactions of the ASME*, vol. 131, no. 11, 2009.

[126] L. C. Burmeister, *Convective heat transfer*, 2nd ed., p. 619., New York: Wiley, 1993.

[127] Y. S. Muzychka and M. M. Yovanovich, "Laminar forced convection heat transfer in the combined entry region of non-circular ducts," *Journal of Heat Transfer-Transactions of the ASME*, vol. 126, no. 1, pp. 54–61, 2004.

[128] J. Pfahler, J. Harley, H. Bau, and J. Zemel, "Liquid transport in micron and submicron channels," *Sensors and Actuators A: Physical*, vol. 22, no. 1-3, pp. 431–434, 1989.

[129] W. Urbanek, J. N. Zemel, and H. H. Bau, "An investigation of the temperature dependence of Poiseuille numbers in microchannel flow," *Journal of Micromechanics and Microengineering*, vol. 3, no. 4, pp. 206–209, 1993.

[130] I. Papautsky, J. Brazzle, T. Ameel, and A. B. Frazier, "Laminar fluid behavior in microchannels using micropolar fluid theory," *Sensors and Actuators A: Physical*, vol. 73, no. 1-2, pp. 101–108, 1999.

[131] G. M. Mala and D. Q. Li, "Flow characteristics of water in microtubes," *International Journal of Heat and Fluid Flow*, vol. 20, no. 2, pp. 142–148, 1999.

[132] W. L. Qu, G. M. Mala, and D. Q. Li, "Pressure-driven water flows in trapezoidal silicon microchannels," *International Journal of Heat and Mass Transfer*, vol. 43, no. 3, pp. 353–364, 2000.

[133] Z. Y. Guo and Z. X. Li, "Size effect on microscale single-phase flow and heat transfer," *International Journal of Heat and Mass Transfer*, vol. 46, no. 1, pp. 149–159, 2003.

[134] G. L. Morini, "Viscous heating in liquid flows in micro-channels," *International Journal of Heat and Mass Transfer*, vol. 48, no. 17, pp. 3637–3647, 2005.

[135] C. L. Ren and D. Q. Li, "Electroviscous effects on pressure-driven flow of dilute electrolyte solutions in small microchannels," *Journal of Colloid and Interface Science*, vol. 274, no. 1, pp. 319–330, 2004.

[136] X. F. Peng, G. P. Peterson, and B. X. Wang, "Frictional flow characteristics of water flowing through rectangular microchannels," *Experimental Heat Transfer*, vol. 7, no. 4, pp. 249–264, 1994.

[137] X. N. Jiang, Z. Y. Zhou, X. Y. Huang, and C. Y. Liu, "Laminar flow through microchannels used for microscale cooling systems," *1st Electronic Packaging Technology Conference 1997, Proceedings*, pp. 119–122, 1997.

[138] B. Xu, K. T. Ooi, N. T. Wong, and W. K. Choi, "Experimental investigation of flow friction for liquid flow in microchannels," *International Communications in Heat and Mass Transfer*, vol. 27, no. 8, pp. 1165–1176, 2000.

[139] P. Gao, S. Le Person, and M. Favre-Marinet, "Scale effects on hydrodynamics and heat transfer in two-dimensional mini and microchannels," *International Journal of Thermal Sciences*, vol. 41, no. 11, pp. 1017–1027, 2002.

[140] J. Judy, D. Maynes, and B. W. Webb, "Characterization of frictional pressure drop for liquid flows through microchannels," *International Journal of Heat and Mass Transfer*, vol. 45, no. 17, pp. 3477–3489, 2002.

[141] D. Liu and S. V. Garimella, "Investigation of liquid flow in microchannels," *Journal of Thermophysics and Heat Transfer*, vol. 18, no. 1, pp. 65–72, 2004.

[142] K. V. Sharp and R. J. Adrian, "Transition from laminar to turbulent flow in liquid filled microtubes," *Experiments in Fluids*, vol. 36, no. 5, pp. 741–747, 2004.

[143] M. J. Kohl, S. I. Abdel-Khalik, S. M. Jeter, and D. L. Sadowski, "An experimental investigation of microchannel flow with internal pressure measurements," *International Journal of Heat and Mass Transfer*, vol. 48, no. 8, pp. 1518–1533, 2005.

[144] M. Akbari, D. Sinton, and M. Bahrami, "Pressure drop in rectangular microchannels as compared with theory based on arbitrary cross section," *Journal of Fluids Engineering-Transactions of the ASME*, vol. 131, no. 4, 2009.

[145] R. Baviere, F. Ayela, S. Le Person, and M. Favre-Marinet, "Experimental characterization of water flow through smooth rectangular microchannels," *Physics of Fluids*, vol. 17, no. 9, 2005.

[146] W. Escher, "Ultra thin high efficiency heat sinks with water or nanofluid for electronics," Dissertation, ETH Zurich, Diss ETH No. 8667, 2009.

[147] G. J. Michna, E. A. Browne, Y. Peles, and M. K. Jensen, "Single-phase microscale jet stagnation point heat transfer," *Journal of Heat Transfer-Transactions of the ASME*, vol. 131, no. 11, p. 111402 (8pp), 2009.

[148] S. G. Kandlikar, "Single-phase liquid flow in minichannels and microchannels," in *Heat transfer and fluid flow in minichannels and microchannels*, 1st ed.,

ch. 3, pp. 87–136., Amsterdam, Netherlands ; San Diego, CA ; Oxford, UK: Elsevier, 2006.

[149] W. L. Qu and I. Mudawar, "Experimental and numerical study of pressure drop and heat transfer in a single-phase micro-channel heat sink," *International Journal of Heat and Mass Transfer*, vol. 45, no. 12, pp. 2549–2565, 2002.

[150] W. Bohl and W. Elmendorf, "Inkompressible Strömungen," in *Technische Strömungslehre*, 13th ed., ch. 4., Würzburg: Vogel Business Media, 2005.

[151] N. Wojtas and C. Hierold, "Microfluidic heat transfer systems optimized for thermoelectric heat exchangers," *17th International Conference on Solid-State Sensors, Actuators and Microsystems, Proceedings*, pp. 1368–1371, 2013.

[152] F. Kreith, R. M. Manglik, and M. Bohn, *Principles of heat transfer*, 7th ed., p. 696., Stamford, CT: Cengage Learning, 2011.

[153] N. Wojtas, E. Schwyter, W. Glatz, S. Kühne, W. Escher, and C. Hierold, "Power enhancement of micro thermoelectric generators by microfluidic heat transfer packaging," *Sensors and Actuators A: Physical*, vol. 188, pp. 289–295, 2012.

[154] F. Umbrecht, D. Muller, F. Gattiker, C. M. Boutry, J. Neuenschwander, U. Sennhauser, and C. Hierold, "Solvent assisted bonding of polymethylmethacrylate: Characterization using the response surface methodology," *Sensors and Actuators A: Physical*, vol. 156, no. 1, pp. 121–128, 2009.

[155] UKAS, "The expression of uncertainty and confidence in measurement," 2007.

[156] N. Wojtas, L. Ruthemann, W. Glatz, and C. Hierold, "Optimized thermal coupling of micro thermoelectric generators for improved output performance," *Renewable Energy*, vol. 60, pp. 746–753, 2013.

[157] N. Wojtas, M. Grab, W. Glatz, and C. Hierold, "Stacked micro heat exchange system for optimized thermal coupling of microTEGs," *Journal of Electronic Materials*, vol. 42, no. 7, pp. 2103–2109, 2013.

[158] H. Schmid, "Less emissions through waste heat recovery," *Green Ship Technology Conference '04, Proceedings*, 2004.

[159] H. J. Goldsmid, A. R. Sheard, and D. A. Wright, "The performance of bismuth telluride thermojunctions," *British Journal of Applied Physics*, vol. 9, no. 9, pp. 365–370, 1958.

[160] W. J. Xie, X. F. Tang, Y. G. Yan, Q. J. Zhang, and T. M. Tritt, "Unique nano-structures and enhanced thermoelectric performance of melt-spun BiSbTe alloys," *Applied Physics Letters*, vol. 94, no. 10, 2009.

[161] J. I. Lienhard and J. V. Lienhard, "Analysis of heat conduction and some steady one-dimensional problems," in *A heat transfer textbook*, ch. 4, pp. 141–191., Cambridge, Massachusetts: Phlogiston Press, 2008.

Acknowledgement

I would like to thank Prof. Hierold for offering me the opportunity to conduct this PhD thesis in the Micro and Nanosystems group at ETH Zürich. Furthermore, I would like to thank my co-referee Prof. Poulikakos for the final review of this work.

Many thanks for interesting discussion, support and great company go to all the current and previous members of the MNS group. In particular special thanks go to Etienne Schwyter who introduced me to the topic of thermoelectricity during my master thesis and has also helped me with interesting inputs during the course of the project. I am very much obliged to Stéphane Kühne for valuable processing advices, help with the measurement setup and proof reading this thesis. Also the processing support, interesting discussions and continuous 'funny' jokes from Yunjia Li are greatly appreciated. Furthermore, I would like to thank Emine Cagin for great scientific and personal conversations and for proofreading many English reports, including main parts of this PhD thesis. I really enjoyed sharing the office with her.

Also many thanks go to the greenTEG team for providing me with TEG samples, processing opportunities and great support. Special thanks go Thomas Helbling for valuable scientific inputs, Florian Umbrecht for building the large scale measurement setup, Michele Zahner for the help with the large scale microchannel fabrication and Wulf Glatz for initiating the TEG project with his work on flexible micro thermoelectric generators.

I am very much indebted to all my master, semester and bachelor thesis students who greatly contributed to the success of this project: Barbara Schaffner, Davud Sadihov, Floria Ottonello, Franziska Ryser, Gion-Andri Büsser, Lukas Rüthemann, Maarten Flink, Martina Grab, Patrick Streit, Samuel Ruckstuhl, Silvan Staufert and Stefan König.

I would also like to thank Werner Escher for providing me with the generic part of the μHTS model and answering many of my questions as well as Salvador Pané i Vidal for the help with the copper electroplating process. Furthermore, many thanks go to Donat Scheiwiller and Stefan Blunier for running the CLA-FIRST clean room, where most of the processing was carried

Publications

Reviewed Articles

A1 N. Wojtas, L. Rüthemann, W. Glatz, and C. Hierold, "Optimized thermal coupling of micro thermoelectric generators for improved output performance," Renewable Energy, vol. 60, pp. 746-753, 2013.

A2 N. Wojtas, M. Grab, W. Glatz, and C. Hierold, "Stacked Micro Heat Exchange System for Optimized Thermal Coupling of MicroTEGs," Journal of Electronic Materials, vol. 42, pp. 2103-2109, 2013.

A3 N. Wojtas, E. Schwyter, W. Glatz, S. Kühne, W. Escher, and C. Hierold, "Power enhancement of micro thermoelectric generators by microfluidic heat transfer packaging," Sensors and Actuators A: Physical, vol. 188, pp. 289 -295, 2012.

A4 U. Lang, T. Süss, N. Wojtas, and J. Dual, "Novel Method for Analyzing Crack Growth in Polymeric Microtensile Specimens by In Situ Atomic Force Microscopy," Experimental Mechanics, vol. 50, pp. 463-472, 2010.

Conference Proceedings

C1 N. Wojtas and C. Hierold, "Microfluidic heat transfer systems optimized for thermoelectric heat exchangers," Proceedings of the 17th International Conference on Solid-State Sensors, Actuators and Microsystems, June 16-20, Barcelona, Spain, pp. 1368-1371, 2013.

C2 N. Wojtas, F. Umbrecht, and C. Hierold, "Towards efficient fluidic waste heat recovery by a large scale micro thermoelectric heat exchange system," Proceedings of the 32nd International Conference on Thermoelectrics , June 30 - July 3, Kobe, Japan, 2013.

C3 N. Wojtas, M. Grab, and C. Hierold, "Stacked micro heat exchange system for optimized thermal coupling of microTEGs," Proceedings of the 31st International Conference on Thermoelectrics, July 9 - 12, Aalborg, Denmark, 2012.

C4 N. Wojtas, E. Schwyter, W. Glatz, S. Kühne, W. Escher, and C. Hierold, ”Power enhancement of micro thermoelectric generators by micro fluidic heat transfer packaging,” Proceedings of the 16th International Conference on Solid-State Sensors, Actuators and Microsystems, June 5-9, Beijing, China, pp. 731-734, 2011.

C5 W. Glatz, L. Durrer, E. Schwyter, M.G. Granada, M. Schnippering, F. Umbrecht, M. Kugler, P. Stein, N. Wojtas, and C. Hierold, ”Producion of Low-Cost, Low-Weight and Flexible Thermoelectric Converters,” in Thermoelectrics goes Automotive, Dec. 9-10, Berlin, Germany, pp. 34-41, 2010.

Conference Talks and Invited Talks

T1 N. Wojtas and C. Hierold, ”Thermoelectric Power Generation - Focus on Micro Fluidic Waste Heat Recovery,” DENSO Research Laboratories, July 10, Nisshin-shi, Japan, 2013.

T2 N. Wojtas, F. Umbrecht, and C. Hierold, ”Towards efficient fluidic waste heat recovery by a large scale micro thermoelectric heat exchange system,” 32nd International Conference on Thermoelectrics , June 30 - July 3, Kobe, Japan, 2013.

T3 N. Wojtas, E. Schwyter, W. Glatz, S. Kühne, W. Escher, and C. Hierold, ”Power enhancement of micro thermoelectric generators by micro fluidic heat transfer packaging,” 16th International Conference on Solid-State Sensors, Actuators and Microsystems, June 5-9, Beijing, China, pp. 731-734, 2011.

Supervised Student Projects

S1 P. Streit "Thermal Energy Harvesting for Zero-Power EEG Acquisition, " Master thesis, spring semester 2013.

S2 F. Ryser, "Parameter Optimization and GUI for a Thermoelectric Heat Exchange System Model," Bachelor thesis, spring semester 2013.

S3 S. Ruckstuhl, "Interface Optimization in Thermoelectric Heat Exchangers," Bachelor thesis, spring semester 2013.

S4 G.A. Büsser, "Ultra-low Temperature Bonding Techniques for Structured Metal Polymer Interfaces," Semester thesis, autumn semester 2012.

S5 F. Ottonello Briano, "Design, Fabrication and Testing of a Large-area Micro Heat Transfer System for PowerCube Application," Master thesis, spring semester 2012.

S6 M. Grab, "Micro Heat Transfer System Characterization and Testing for Thermoelectric 'Power Cube' Application," Bachelor thesis, spring semester 2012.

S7 M. Grab, "Literature Research on Thermoelectric Generators integrated in Heat Exchanger Systems," Studies on Mechatronics, spring semester 2012.

S8 L. Rüthemann, "Fabrication, Characterization and Modeling of a Micro Heat Transfer System for Power Enhancement of Thermoelectric Generators," Master thesis, spring semester 2011.

S9 S. Staufert, "Process Development of High Aspect Ratio SU-8 Molds for Copper Microchannel Fabrication," Bachelor thesis, spring semester 2011.

S10 D. Sadihov, "Design of a micro heat sink for power enhancement of thermoelectric generators," Bachelor thesis, spring semester 2010.

S11 M.K.G. Flink, "Thermal Stress Analysis of Bonding Interfaces in Actively Cooled Micro Thermoelectric Generators," Semester thesis, spring semester 2010.

S12 S. König, "Evaluation of Copper Electroplating for Micro Channel Heat Sinks," Studies on Micro and Nanosystems, spring semester 2010.

S13 B.Schaffner "Modeling of Micro Thermoelectric Generator Design and Applications, " Semester thesis, spring semester 2009.

Curriculum vitae

Personal Details

Birth   October 3rd 1982
Citizenship Poland, Switzerland

Education

01/2009 – 02/2014	**ETH Zurich, Micro and Nanosystems, Switzerland** Dissertaion „*Microfluidic Thermoelectric Heat Exchangers for Low-Temperature Waste Heat Recovery*"
03/2007 – 08/2008	**ETH Zurich, Department of Mechanical Engineering, Switzerland** M.Sc. in Micro and Nanosystems, Willi Studer Award
10/2003 – 08/2006	**ETH Zurich, Department of Mechanical Engineering, Switzerland** B.Sc in Mechanical Engineering
08/1999 – 07/2000	**Pinconning Area High School, Michigan, USA** High school exchange program
08/1995 – 09/2002	**Kantonsschule Rychenberg, Winterthur, Switzerland** Matura, type D (modern languages)

Work Experience

01/2009 – 02/2014	**ETH Zurich, Micro and Nanosystems, Switzerland** Research and teaching assistant, supervisor of 13 student projects
10/2006 – 02/2007	**DENSO Research Laboratories, Nishin, Japan** Industrial internship in the field of micro-optical devices
07/2006 – 08/2006	**ETH Zurich, Institute for Mechanical Systems, Switzerland** Research assistant in the field of micromechanics
03/2004 – 04/2004	**Unimec Fabrikations AG, Wetzikon, Switzerland** Industrial internship in the field of machining processes
09/2003 – 12/2003	**Zurich University Library, Switzerland** Library assistant, part-time work
10/1998 – 12/2007	**Laboratory of KWH Bautechnologen AG, Zurich, Switzerland** Chemical analyst, part-time work

Language

German/Polish	native
English	fluent, Certificate of Proficiency
Spanish	oral communication (level B2)
French	oral communication (level B2)